Istituto Universitario di Studi Superiori di Pavia

Advanced Modeling of Stents: from constitutive modeling to biomedical (isogeometric) analysis

by

Mauro Ferraro

A Thesis submitted in Fulfilment of the Requirements
for the Degree of Doctor in Philosophy in

Computational Mechanics and Advanced Material
at Istituto Universitario di Studi Superiori, Pavia, Italy

Ph.D. Program Coordinator: Prof. F. Auricchio

Supervisor:
Prof. A. Reali - Università degli Studi di Pavia
Coadvisors:
Prof. F. Auricchio - Università degli Studi di Pavia
Dr. S. Morganti - Università degli Studi di Pavia

XXVII Ciclo (2011-2014)

to Mary.

Dissatisfaction with possession and achievement is one of the requisites to further achievement.

J. Hope

Acknowledgements

Writing the dissertation acknowledgments has always been a complex task for me. It is not trivial to resume three years of work, satisfactions (many), frustrations (few), travels and a lot of great people.
First, I would like to express my special appreciation and thanks to my advisor Prof. Alessandro Reali, you have been a tremendous mentor for me. I would like to thank you for encouraging day by day my research and for allowing me to grow as a research scientist and as a man within a challenging and exciting research field like IgA.
I would also like to thank my co-advisors Prof. Ferdinando Auricchio and Dr. Simone Morganti, your advices on both research as well as on the human side have been priceless and incented me to struggle towards my goals.
I am extremely grateful to Prof. Robert L. Taylor for his invaluable support and the opportunity to go deep inside the research aspects related to FEAP, you are a brilliant researcher and an incredible mentor. The time I spent with you and your family in the USA has been one of the best experiences of my life.
I would like to thank Prof. Laura De Lorenzis and all the guys in Lecce for introducing me to the interesting world of contact mechanics, your support has been crucial for my research activity.
Thanks to all my colleagues: the old guard Giuseppe, Andrea, Giulia, Josef, Adrien, Elisa Reali, Elisa Boatti, Chiara, Marco, Isabella, Paolo, Tuong, Anna, Stefania, Carolina but also the newbies :) Gianluca, Valentina, Chiara, Rodrigo, Marco and Xi. I hope we will continue to have fun and share experiences, opinions and tons of coffee.

Special thanks go to Dr. Michele Conti, the *right-answer at the right-moment* man. If I am a passionate biomechanics researcher is mostly thanks to you.
A special thanks to my family, words cannot express how grateful I am to you all for the daily support and deep love.
Last but not least, I want to thank my beloved Mary. A lot of water has flowed under the bridge since we discussed the derivative exercise after Calculus 1 exam, and I still barely realize how much the life has been generous with me. I love you, there is nothing more to say.

Contents

English summary

CARDIOVASCULAR diseases are the main cause of death in western countries and are responsible for hundreds of thousands of early deaths all over the world. Several options are nowadays available for the treatment of such pathologies, but the current trend in modern clinical practice focuses on the application of percutaneous minimally-invasive techniques, characterized by the employment of high-tech endoprosthesis driven to the pathological district by mean of an endoluminal path.

In particular, the devices object of this dissertation, i.e., carotid artery stents, are characterized by complex geometrical features and non standard shape memory alloy (SMA) material behavior.

The employment of such devices call for continuous technological improvements with respect to prosthesis materials, device design and procedure planning techniques. In fact, the prostheses are required to be always more safe and efficient in terms of delivery process, implantation and long-term performance. Moreover, the concept of predictive medicine, i.e., the family of methods and techniques aiming at predicting the outcomes of alternative treatment plans for an individual patient, is becoming a highly-demanded requirement and this can only be exploited through robust and cost-effective engineering tools.

In this aspect, SMA constitutive modeling represents a fundamental challenge in order to efficiently predict the performance of stent devices. In particular, the ideal SMA constitutive model needs to reproduce the main macroscopic material behaviors resorting to a limited number of parameters with a clear physical interpretation.

Within this context, computational modeling, typically based on Finite Element Analysis (FEA), has shown the capability to provide useful information to understand the mechanics of cardiovascular devices and to improve device design. In particular, FEA is employed to investigate different combinations of material behaviors, geometries and working conditions prior to prototype manufacturing. Moreover, FEA is often used to reproduce a wide variety of clinical scenarios that cannot be investigated experimentally.

However, even if FEA is already a widely employed and well assessed simulation tool, it presents some drawbacks that can limit the geometrical accuracy of the domain under investigation and the regularity of the approximated solution without resorting to a huge number of degrees of freedom.

Isogeometric analysis (IgA), has recently been developed as an exact-geometry, cost-effective alternative to classical FEA. Roughly speaking, IgA proposes to replace the low-order, low-regularity FEA basis functions with the high-order, high-regularity basis functions employed in computer- aided design (CAD). This leads to a significant enhancement of the accuracy-to-computational-effort ratio, with a great impact on the simulation efficiency.

This dissertation is collocated within this scenario since we aim at setting up advanced and efficient computational tools to investigate the main features of different SMA carotid artery stents by mean of traditional FEA and innovative IgA. The final goal of this dissertation is to compare and discuss the impact of innovative IgA in terms of solution accuracy and computational efficiency.

This work ultimately aims at providing a basis for developing accurate and efficient predictive tools that can support researchers and medical companies during stent manufacturing and design process.

Italian summary

Le malattie cardiovascolari rappresentano la principale causa di morte nei paesi occidentali e sono responsabili di centinaia di migliaia di morti in tutto il mondo. Al giorno d'oggi sono disponibili diverse opzioni terapeutiche per il trattamento di queste patologie, tuttavia la moderna pratica clinica si sta orientando verso l'applicazione di tecniche percutanee minimamente invasive, caratterizzate dall'impianto di endoprotesi trasportate nel distretto patologico attraverso un percorso intravascolare.

In particolare questo lavoro di tesi si focalizza sullo studio degli stent carotidei, endoprotesi metalliche caratterizzate da geometrie complesse e dall'impiego di materiali non standard come le leghe a memoria di forma (SMA). L'utilizzo efficiente di questi dispositivi richiede continui miglioramenti tecnologici nei materiali, nel design e nelle tecniche di impianto, in modo da garantire alti livelli di sicurezza ed efficienza in termini di esito clinico e prestazioni meccaniche della protesi nel lungo periodo.

Inoltre l'implementazione di strumenti ingegneristici robusti ed efficienti rappresenta la componente fondamentale degli strumenti di medicina predittiva, ovvero la famiglia di metodi e tecniche con lo scopo di predire gli esiti di diversi piani di intervento clinico per uno specifico paziente

In questo ambito la modellazione costitutiva dei materiali SMA rappresenta il primo fondamentale tassello nell'ottica di predire in maniera accurata le performance meccaniche degli stent carotidei. In particolare, il modello costitutivo SMA ideale dovrebbe essere in grado di riprodurre i principali fenomeni macroscopici di questi materiali, ricorrendo ad un numero limitato di parametri con una chiara interpretazione fisica.

In questo contesto, gli strumenti di modellazione computazionale, tipicamente basati su analisi agli elementi finiti (FEA), hanno dimostrato negli anni la capacità di fornire informazioni utili per comprendere il comportamento meccanico di diversi dispositivi medici nell'ottica di ottimizzarne il design. In particolare, le FEA sono largamente utilizzate per investigare diverse combinazioni di materiali, geometrie e condizioni di impiego prima della produzione di un prototipo. Inoltre, le FEA vengono impiegate per riprodurre numericamente una vasta gamma di scenari clinici che non possono essere valutati sperimentalmente.

Tuttavia, anche se le FEA sono considerate uno strumento di simulazione robusto ed affidabile, presentano alcune limitazioni che possono inficiare l'accuratezza geometrica del dominio investigato e la regolarità della soluzione approssimata, a meno di ricorrere a un elevato numero di gradi di libertà.

L'analisi isogeometrica (IgA) é una tecnica numerica innovativa recentemente sviluppata come un' alternativa efficiente e accurata alle FEA. In particolare, l' IgA si propone di rimpiazzare le funzioni di forma ad ordine-basso e regolarità-bassa tipiche delle FEA, con le funzioni ad ordine-alto e regolarità-alta impiegate negli strumenti di Computer Aided Design (CAD). Questo porta a un miglioramento significativo del rapporto tra accuratezza della soluzione e costo computazionale per la generazione del dominio discretizzato, con un grande impatto sull'efficienza computazionale.

Questa tesi si colloca in questo contesto, in quanto si propone di impostare e implementare diversi strumenti computazionali avanzati ed efficienti per investigare le principali proprietà di diversi stent carotidei attraverso l'impiego delle tradizionali FEA e IgA innovative. Inoltre, l'obiettivo finale di questa tesi é di confrontare e discutere l'impatto dell'IgA in termini di accuratezza della soluzione ed efficienza computazionale. Infine, questo lavoro si pone come obiettivo finale la creazione di una base per lo sviluppo di strumenti predittivi accurati ed efficienti che potranno supportare ricercatori e aziende durante e il design e la produzione di nuovi stent.

List of Tables

List of Figures

Chapter 1

Introduction

THE modern clinical practice for the treatment of cardiovascular diseases, based on the implant of minimally-invasive endoprosthesis, calls for continous technological improvements with respect to prosthesis materials, device design and procedure planning techniques. In fact, the prostheses are required to be always more safe and efficient in terms of delivery process, implantation and long-term performance.

Such a framework requires a deep comprehension of the material behavior of the involved components. Moreover, different sources of complexity (geometry, working conditions etc.) make often impossible to determine experimentally the mechanical behavior of a specific medical device.

With the advent of the information age and the introduction of the modern computational modeling techniques, we are now able to accurately simulate the behavior of a wide variety of applications where material phenomena at different scales are coupled with complex geometries and working conditions.

Given these basic statements, one of the main aims of this chapter is introducing the medical devices object of this dissertation, i.e., the carotid

artery stents, and the importance of stent design in the determination of the outcomes of stenting procedures.

Subsequently, the role of advanced numerical modeling to evaluate the mechanical properties of a particular stent design is presented. In this aspect, the problem of the definition of proper and robust material models have to be addressed. In particular, the present doctoral research focuses on shape memory alloy modeling. Moreover, with the goal of performing accurate simulations, we describe the numerical approach with a double perspective on classical Finite Element Analysis (FEA) and on a novel numerical technique, namely Isogeometric analysis (IgA), in order to motivate the final goal of the present dissertation.

1.1 Vascular surgery: the minimally invasive approach

Cardiovascular diseases (CVD) is a general term used to describe disorders that can affect the heart and/or blood vessels. Each year, CVD cause over 4 million deaths in Europe corresponding to the 42% of the overall mortality (see Fig. 1.1). Moreover, CVD cause an estimated cost of €196 billions every year for the EU economy in terms of direct cost and loss of productivity [1]. Stroke, defined as a loss of brain function in relations of a reduction of the blood supply, represents the second main form of CVD in terms of death rate and the first in terms of loss of productivity due to chronic impairment [1].

The pathological events leading to stroke are complex, including biochemical reactions, genetic predisposition and blood flow disorders, but they can be roughly reconnected to the so-called atherosclerotic plaque formation or atherosclerosis. Atherosclerosis is defined as an accumulation of substances (mainly cells, lipids and calcium) in the interstice between

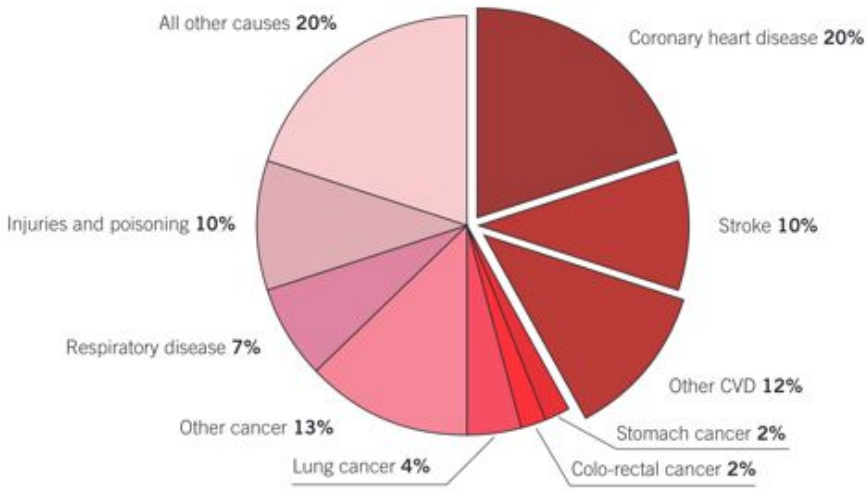

Figure 1.1 *European CVD statistics: deaths subdivided by cause [1].*

the different layers of the vascular wall. This phenomenon can lead to many dangerous effects, including vessel hardening and lumen reduction, i.e., stenosis, which can reduce or, at worst, block the blood flow and cause tissue necrosis. Atherosclerosis can arise in different districts of the vascular system, but the atherosclerosis of the carotid artery is the main responsible for stroke.

The gold standard for the treatment of carotid artery atherosclerosis is the *Carotid Endarterectomy* (CEA), a surgical procedure where the surgeon peels the plaque away from the carotid artery. Once the plaque is removed from the carotid artery, more oxygen-rich blood can flow through the artery to the brain, reducing the risk of stroke (see Fig. 1.2). CEA is well-proven for preventing strokes and is the most commonly performed major vascular operation. The first clinical report of a successful CEA dates back to the

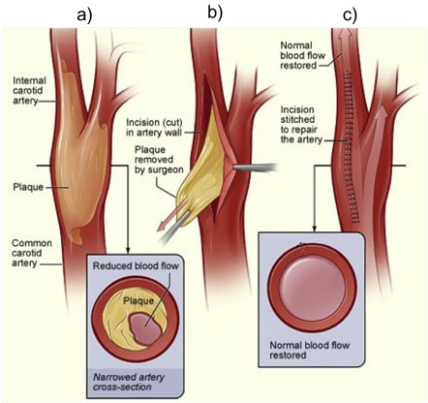

Figure 1.2 *Carotid endarterectomy (CEA): a) carotid artery with plaque buildup b) the plaque has been separated from the outer wall of the common carotid artery and external carotid artery and is now being removed from the internal carotid artery; b) sutures are placed at the distal end of the arteriotomy.*

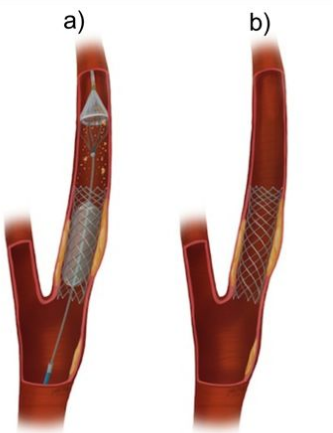

Figure 1.3 *Carotid artery stenting (CAS) : a) stent placement (coupled with a distal filter device) in the carotid artery to support the inner artery wall and keep the artery open; b) the normal blood flow is restored in the stent-widened artery.*

paper of Eastcott et al. [2], but only after the North American Symptomatic Carotid Endarterectomy Trial (NASCET) [3] and the European Carotid Surgery Trial (ECST) [4], the medical community conclusively accepted the benefit of CEA in preventing strokes [5].

Nowadays, the current trend in clinical procedure is moving toward the CEA's minimally invasive alternative, i.e., the *Carotid Artery Stenting* (CAS).

CAS restores the vessel patency by enlarging the narrowed lumen through the expansion of a metallic mesh, i.e., the stent, which compresses the dilated plaque material. The stent is targeted to the lesion location by means of a catheter running inside an endoluminal path (see Fig. 1.3). With respect to deployment mechanics, stents can be classified as: i) balloon-expanding stents, which are mounted on a balloon which is gradually inflated driving the stent deployment; ii) self-expanding stents, which take advantage of their peculiar mechanical properties, typically shape memory alloy pseudo elasticity, to recover their original shape when deployed at the target lesion [6]. CAS is a younger technology with respect to CEA and the first implant dates back only to 1989, when Klaus Mathias placed the first stainless steel stent in a 65 old man with symptomatic carotid stenosis. In 1999, the first self-expandable stents made from a Nickel-Titanium shape memory alloy (SMA) became available on the market and rapidly replaced ballon-expandable stents [7].

The outcomes coming from CEA and CAS do not clarify which procedure is safer for the patient and the debate in the literature is still open. The most important clinical trial dealing with this issue, i.e., the Carotid Revascularization Endarterectomy versus Stent Trial (CREST) [8], concludes that among patients with symptomatic or asymptomatic carotid stenosis, the risk of the composite primary outcome of stroke, myocardial

infarction, or death did not differ significantly in the group undergoing CAS and the group undergoing CEA.

In summary, the advent of CAS moved the perspective of clinicians from the traditional approach, where only the surgeon's skill determined a satisfactory success rate of the procedure, to a novel one, in which the harmonic convergence of technology development and refinement of endovascular intervention work together to reduce the impact of the surgical procedure in terms of post-procedural patient's condition, social and economical costs.

1.2 The role of stent design

In Section 1.1 the benefits of CAS as a cost-effective alternative to classical surgical procedure were presented. However, the change of surgical paradigm from CEA to CAS introduced different complications and technological issues. In particular, it is important to note that stent deployment radially compresses the atherosclerotic plaque between the vessel wall and the stent itself. In the majority of implants, this does not induce any adverse phenomena, but, in a significant percentage of patients, post-stenting narrowing can be appreciateted [9].

According, to Lally et al. [10], three main types of post-stenting narrowing can be identified due to the fact that: i) excessive stent elastic recoil induces immediate narrowing of the lumen; ii) the stent expansion induces vessel injuries and may initiate intimal hyperplasia, i.e., a uncontrolled proliferation of vessel wall cells that cause post-procedural restenosis (see Fig. 1.4-a); or iii) vessel remodeling can cause narrowing in response to the stresses generated in the tissue.

Another major CAS issue is related to the stent delivery process. In particular, the stent needs to accommodate the tortuous path from the

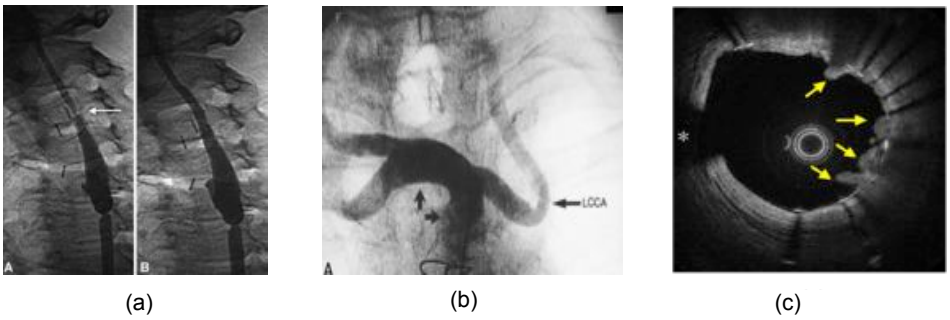

(a) (b) (c)

Figure 1.4 *Major stenting issues: a) in-stent restenosis [11]; b) tortuous vessel in elder patient; c) Intravascular Optical Coherence Tomography prolapse imaging [12].*

incision to the lesion location. Moreover, the implanted stent should not excessively straighten the carotid artery in order to limit vessel injuries (Fig. 1.4-b).

At last, the stent must minimize the plaque prolapse in order to reduce the risk of stroke and/or local inflammatory reactions (Fig. 1.4-c).

Resuming, the "optimal" carotid stent design has to: i) guarantee enough flexibility to ensure a safe deployment and to improve the stent conformability [1]; ii) provide sufficient radial strength to minimize the elastic recoil reducing, at the same time, the risk of stent-induced vessel injury; iii) minimize the tissue prolapse by mean of a dense mesh structure.

It is immediately clear that the design plays a crucial role in determining the stent features and, consequently, the outcomes of CAS procedure. Moreover, the structural requirements of the"optimal" carotid artery stent design are various and, often, contradictory [10, 13, 14, 15]. For this reason, the stent designs available in the market usually result as a

[1]Stent conformability is the stent ability to adapt its deployed configuration to the vessel tortuosity.

trade-off between several biomechanical features and the investigation of such requirements needs to set up different engineering benchmarks able to experimentally evaluate the material properties associated with the complex geometrical features of such devices (Fig. 1.5). However, experimental tests are often not applicable due to high costs for prototype manufacturing and/or working conditions that are difficult to reproduce experimentally, e.g., stent scaffolding after stent implant. In this aspect, computational studies can be used both as complementary or alternative to experimental studies.

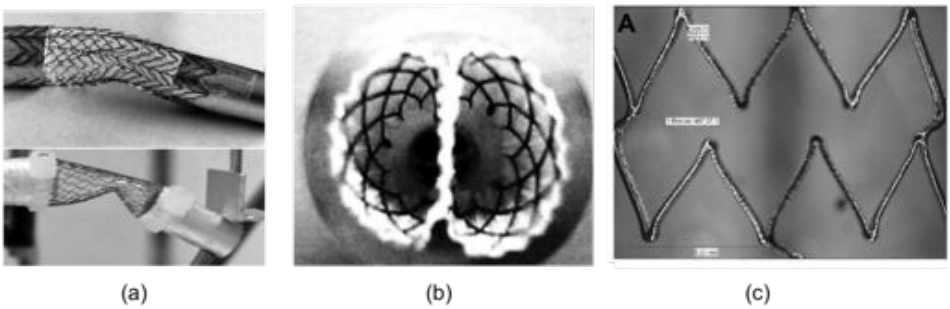

Figure 1.5 *Carotid stent experimental benchmarks: a) flexibility evaluation test [15]; b) radial force test [6]; c) stent scaffolding evaluation (measured as free-expanded cell area) [15].*

1.3 Advanced modeling of stents

Nowadays, modern computational methods are an ubiquitous tool to reproduce various clinical procedures for pre-operative planning and to predict the mechanical behavior of a wide range of medical devices. The major benefit of the employment of computational methods for the mechanical evaluation of medical devices is the possibility to test different combina-

tions of materials, geometries and working conditions prior to prototype manufacturing or when the traditional experimental approach is too expensive or difficult to implement. Moreover, computational methods are the basic ingredient of the concept of *predictive medicine* [16], i.e., the family of methods and techniques aiming at predicting the outcomes of alternative treatment plans for an individual patient. Clearly, the reliable application of such computational methods for real life clinical and industrial problems requires the deep comprehension of the different sources of complexity related to the problem itself. Focusing on carotid artery stent modeling, the following challenges need to be addressed:

- Material behavior: as introduced in Section 1.1, modern carotid artery stents are made of Nickel-Titanium SMA, a metallic alloy able to elastically recover strains after stress-induced large deformations. SMA behavior is inherently non linear and their macroscopical properties are driven by a complex thermomechanical solid phase transition. In this aspect, the constitutive modeling of such materials requires the development of accurate models to reproduce the major phenomena involved with the material behavior, resorting to a limited number of parameters possibly easy to estimate and underlying a clear physical interpretation.

- Geometry description: the majority of carotid artery stents are constituted by a set of circular rings connected with a variable number of linkers. Shape, number and arrangement of these structures dramatically influence the various stent features. In this aspect, the computational tools should provide a reliable framework to relate the real geometry, typically identified by a Computer Aided Design (CAD) model, and its numerical counterpart.

- Working conditions: each evaluation of a particular stent feature requires a reliable transposition of the device working conditions into the computational model. This task is not trivial, since real life problems often include complex non linear phenomena, e.g., contact or geometrical instability, that can affect the predicting capabilities of many computational models.

Within this context, Finite Element Analysis (FEA) has been widely employed in the last few decades to understand and predict biomechanical phenomena and to optimize the design of a wide variety of medical devices (Fig. 1.6). However, even if FEA is already a widely employed and well assessed simulation tool, it presents some limitations that can affect both the geometrical accuracy of the domain under investigation and the accuracy of the approximated solution. In particular, low-order and low-regularity polynomials used to discretize the continuum domain do not allow, in general, to accurately represent complex geometries unless extremely fine meshes are adopted. At the same time, FEA basis functions do not allow one to properly approximate the solution without resorting to a high number of degrees of freedom, in particular when different sources of non linearity are present.

Isogeometric analysis (IgA), has been recently proposed as an exact-geometry, cost-effective alternative to classical FEA [17, 18], proposing to replace the low-order, low-regularity FEA basis functions with the high-order, high-regularity basis functions employed in CAD while retaining an isoparametric framework. This seems indeed an ideal framework to address the FEA limitations highlighted above.

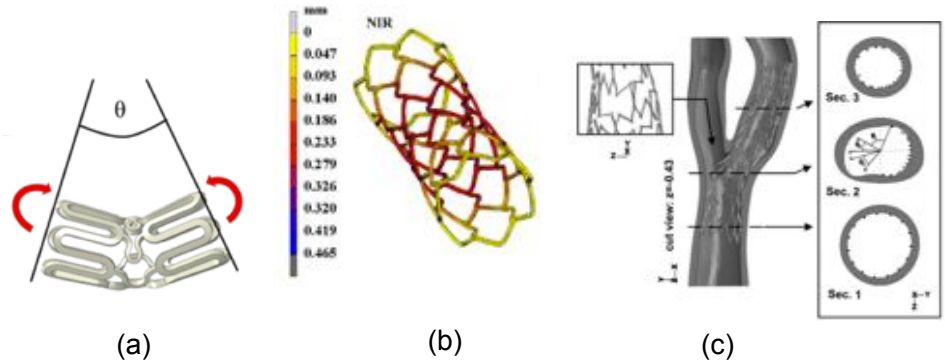

Figure 1.6 *Carotid stent numerical benchmarks: a) flexibility evaluation test [19]; b) stent radial retraction test [10]; c) stent struct distributions numerical evaluation [20].*

1.4 Aim of the doctoral research

The previous sections confirmed how important the design of a carotid artery stent is and how the computational tools can contribute to determine the "ideal" combination of stent features. The ultimate goal of this doctoral research is to provide a set of numerical tools to efficiently evaluate the principal features of different SMA self-expanding carotid artery stents. The development of such tools requires a mix of expertise on SMA constitutive modeling and computational mechanics. In particular, a reliable constitute model is important to predict the non linear, inelastic SMA behavior. Moreover, a set of proper computational techniques is mandatory to accurately reproduce real life experimental tests in terms of geometric description of the domain, but also in terms of regularity of the numerical solution. In the first part of this dissertation, we exploit this framework using FEA, a well-known and widely employed computational tool.

Subsequently, we move to a novel and cost-effective numerical technique, like the above mentioned Isogeometric Analysis. The initial motivation behind IgA lied into the desire of fulfill the gap between the analysis community, substantially based on FEA, and computer-aided design (CAD) community. The basic idea is to develop a computational framework in which the traditional FEA basis functions were substituted with that one employed in CAD systems. This implies the ability to describe exactly the computational domain geometry throughout the analysis process, including, at the same time, the chance to tune the basis functions continuity. The proposed framework aims at providing a basis for developing accurate and efficient predictive tools that can help researchers and medical companies during stent manufacturing and R & D process.

1.5 Organization of the dissertation

The dissertation is organized as follows:

- Chapter 2: Shape memory alloy constitutive modeling
  The proper constitutive modeling of the NiTiNOL shape memory alloy (SMA) is the first step for a reliable characterization of the mechanical properties of a stent device. In this chapter, the SMA peculiar properties are introduced, and the constitutive models proposed by Souza et al. [21] and Auricchio-Taylor [22, 23] are described. Thereafter, in order to assess the robustness of the proposed constitutive models, a set of different SMA boundary value problems with increasing complexity are implemented and discussed.

- Chapter 3: Vessel scaffolding evaluation for carotid artery stents: a FEA-based approach

  After CAS, the plaque remains contained between the stent and the vessel wall, moving consequently physicians' concerns toward the stent capability of limiting the plaque protrusion, i.e., toward vessel scaffolding, to avoid that some debris is dislodged after the procedure. Vessel scaffolding is usually measured as the cell area of the stent in free-expanded configuration, neglecting thus the actual stent configuration within the vascular anatomy. In the present study we measure the cell area of four different stent designs deployed in a realistic carotid artery model through patient-specific FEA.

- Chapter 4: Isogeometric analysis basic concepts

In this chapter the basic concepts of B-splines and NURBS are described. Thereafter, the basic IgA concepts are introduced with a focus on applications and comparison with traditional FEA.

- Chapter 5: Stent bending modeling: a comparision between IgA and FEA

  Flexibility, i.e., the capability to properly bend in order to accommodate the tortuous vascular structure is one of the main features for cardiovascular stents . Therefore, in order to properly evaluate the stent response under bending, many stent studies have been performed by means of computational tools based on FEA.

  IgA has recently emerged as a cost-effective alternative to classical FEA, based on the use of typical CAD basis functions for both geometric description and variable approximation.

  Accordingly, this study aims at setting up a novel computational framework based on IgA to evaluate the mechanical performance of carotid artery stents. Stent bending analyses involving large deformations are performed, with both IgA and classical FEA, on two carotid artery stent designs.

- Chapter 6: IgA based contact mechanics: from basics to real life applications

  The basic idea behind IgA is to provide a smooth basis able to describe exactly the computational domain geometry throughout the analysis process, including, at the same time, the chance to control the basis functions continuity. These peculiar features have been applied with

benefits on many critical aspects of FEA, including also contact mechanics. This chapter focuses on the application of a NURBS-based IgA to 3D frictionless contact problems between deformable bodies. Subsequently, a set of IgA-based contact problems with increasing complexity are implemented.

- Conclusions and future works

  In this last chapter, the conclusions are drawn highlighting the original aspects of the doctoral research. Moreover, further research developments are outlined.

Chapter 2

Shape Memory Alloy constitutive modeling

As mentioned in Chapter 1, the majority of CAS procedures worldwide employ self-expanding carotid artery stents. Therefore, the proper mechanical characterization of the shape memory alloys (SMA) constituting such devices represents the first step of the present doctoral research. Starting from the role of innovative materials in the technological progress, SMA discovery and evolution is described. In order to motivate the great success of SMA, their physical properties are detailed with particular care to pseudoelasticity and shape memory effect. Thereafter, two widely employed SMA constitutive models, i.e., Souza model [21] and Auricchio-Taylor model [23] are introduced.
At last, different numerical examples are presented in order to assess the robustness and accuracy of the proposed constitutive models.

2.1 Smart materials: introduction to shape memory alloys

The last 40 years represent an important turning point from a technological point of view. Indeed this period of time coincides with the transition between the "Synthetic materials age" to "Smart materials age" (Fig. 2.1). The main feature of smart materials is the capability to respond, in reac-

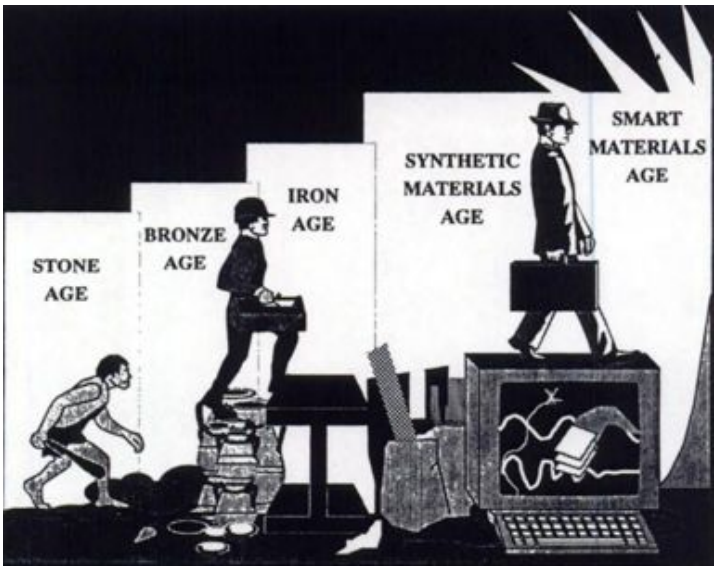

Figure 2.1 *The eras of material science [24].*

tion of an environmental stimuli, with particular changes in some variables, e.g., temperature, moisture, electric or magnetic fields, pH, and stress. Depending on some variations in the external conditions, smart materials can adapt their physical properties and/or their structure. There is a number of types of smart material, some of which are common in the ordinary life. As their variety, the application fields for smart materials goes from electronic engineering to civil engineering, passing through aeronautical and medical

applications. Shape Memory Alloys (SMA) are the most employed in the surgical field, especially for minimally invasive applications.

2.1.1 A little bit of history

Shape memory alloys (SMA) debut on tiptoe in the industrial market. In fact, the discovery of shape memory in AuCd and CuZn occurred with little fanfare in somewhat obscure technical papers with little, if any, follow-on work [25]. The real progress for SMA in engineering applications occurred with the discovery of NiTiNOL (Nichel Titanium alloy, NOL was in honor of the discovery at the Naval Ordinance Laboratory) by Buehler and coworkers in 1962 while investigating materials useful for heat shielding [26]. It was noticed that in addition to its good mechanical properties, comparable to some common engineering metals, the material also possessed a shape recovery capability. Consequently to the NiTiNOL discovery, there was suddenly a great deal of commercial interest, and many commercial applications were developed, especially in automotive and aeronautical fields. However, due to the high costs for NiTiNOL production coupled with a poor comprehension of the SMA complex mechanical behaviors (non-linear tensile properties, hysteresis, non standard fatigue effects), many companies rapidly abandoned the research on SMA. However, the development of different models for material performance prediction during the last 20 years, allowed to understand clearly the thermomechanical processing route and the environmental parameters. Thank to 20 years of studies in their behavior, SMA are, nowadays, an "household" word in the engineering world. Nowadays, the higher production standards combined with a significant decrease in prices thanks to a larger market share, allows moreover to consider new potential applications with tight budgets or cost factors.

2.1.2 SMA properties

The main features of SMA are:

- *Pseudoelasticity*: capability to recover strains after stress-induced large deformations;
- *Shape memory effect*: capability to recover plastic strains after an heating process;

These peculiar properties are combined with the following features:

- Kink resistance;
- Biocompatibility;
- Hysteresis;
- Fatigue resistance;

Such properties justify the large diffusion, in the last 20 years, of SMA in the manufacturing process of a wide variety devices. In the following all the listed properties are described in detail, with particular regard to pseudo elasticity and shape memory effect.

Pseudoelasticity and shape memory effect.

Both pseudo elasticity and shape memory effects are related to martensitic transformation, a diffusionless phase transformation in solids, in which atoms move cooperatively, often by a shear-like mechanism. The transformation from autenite phase to martensite phase does not occur by diffusion of atoms, but rather by shear lattice distortion. This particular phenomenon is associated with the crystallographic organization of SMA,

characterized by a two-solid phases structure. The martensite at free-stress state has the same structure of martensite under a stress-state, but shows different orientations. This assumption suggests that martensite can exist in two different configurations: twinned martensite, characterized by a twinned multi-variant crystallographic structure, not related to any macroscopic deformation, and stress-induced martensite, characterized by a typical detwinned configuration with a single variant crystallographic structure [27] (Fig. 2.2). It is important to remark that the martensitic transformation in SMA consists mainly in a shear, without volume change. The

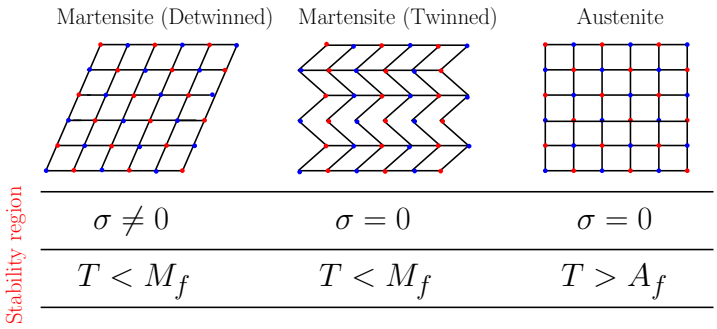

Figure 2.2 *SMA phases: schematic picture and regions of stability.*

transition between different phases is the key to understand the mechanical behavior of SMA, and it is clear that these phenomena are ruled by the strong connection between mechanical effects (mechanical loadings) and thermal effects (temperature variations). A load (at a temperature greater than A_f) causes, initially, an elastic deformation in austenite phase (Fig. 2.3-*left*-a), then, if the deviatoric part of the stress reaches the value of σ^s the transition between austenite to single-variant martensite begins. This phase shows off a plateau due to the occurring of the transformation phase (Fig. 2.3-*left*-b). Once the austenite is completely converted ($\sigma > \sigma_f$),

an elastic deformation for martensite phase can be appreciated. Once the load is removed, the martensitic phase, tends to the reverse transformation (Fig. 2.3-*right*-a), by reason of the instability of martensite phase at high temperatures. This phenomenon causes the complete recovery of the strain (Fig. 2.3-*right*-b). This phenomenon, defined as pseudo elasticity or super elasticity, allows to recover large strains (up to 10%). In the other way,

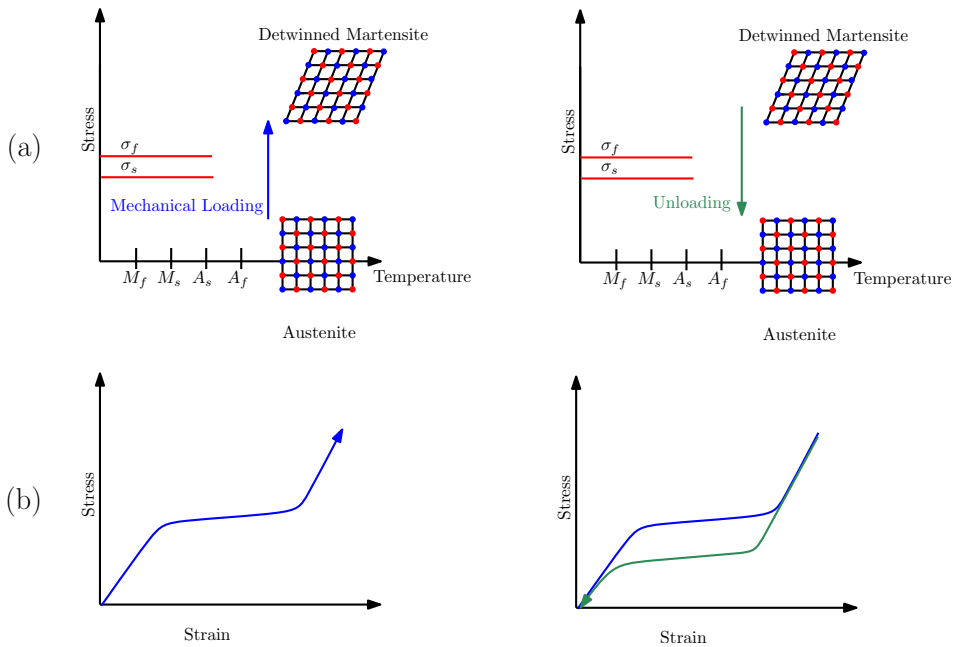

Figure 2.3 *Pseudoelasticity: a) Schematic view of the phase transitions; b) Schematic of the stress strain diagram.*

at a temperature lower than M_f, twinned martensite phase is stable. A load such that the deviatoric part of the stress is greater than σ^f, induces, after an elastic deformation step (Fig. 2.4-*left*-b), the twinned to detained variant martensite transformation takes place. Once the load is removed,

a residual strain can be appreciated(Fig. 2.4-*right*-b). If the material is heated at a temperature around A_f, transition between detwinned martensite and austenite phase occurs, and the residual strain is fully recovered at zero stress. This phenomenon is defined as shape memory effect.

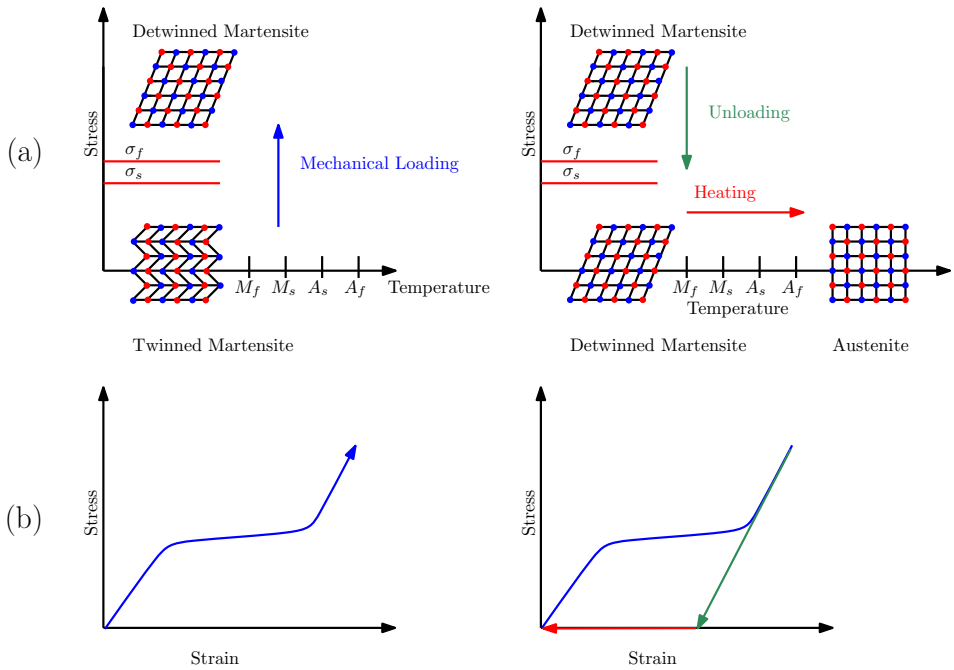

Figure 2.4 *Shape memory effect: a) Schematic view of the phase transitions; b) Schematic of the stress strain diagram.*

Kink resistance

Kink resistance or, more appropriately, crush recoverability (Fig. 2.5), is an important feature of NiTiNOL, even more than pseudo elasticity and shape memory effect in some applications [28]. When strains are locally increased

beyond the plateau strain, stresses increase markedly. This causes strain to partition to the areas of lower strain, instead of increasing the peak strain itself. This phenomenon can be very dangerous for devices performance, and it is not uncommon in steel devices. In NiTiNOL devices, kinking, or strain localization, is prevented by creating a more uniform strain than could be realized with a conventional material [29]. This property is widely employed in medical applications, especially in laparoscopic surgery, where the ability to target the device through side branches or around sharp bends is vital.

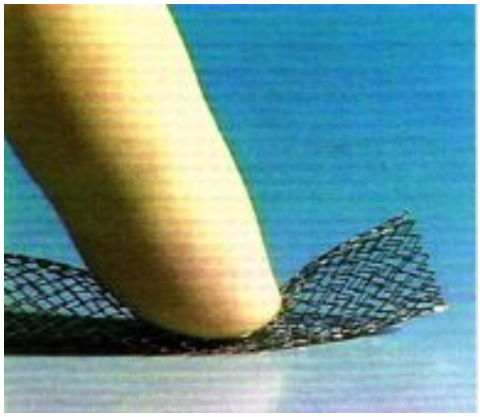

Figure 2.5 *Stent crush recoverability [29].*

Biocompatibility

This feature can be roughly defined as the ability of a material to be not rejected by the human body. Biocompatibility is directly related to the corrosion behavior of the material in a specified solution and the tendency for the alloy to release potential toxic ions. Experimental studies generally

indicate that NiTiNOL has extremely good biocompatibility [28, 30, 31]. This is due to the tendency of Nitinol surfaces to be covered with TiO_2 oxides with only a minor amount of nickel under normal conditions.

Hysteretical dissipation

The superelastic hysteresis, as described in the Section 2.1.1, was initially considered a drawback because it reduces the energy storage efficiency. However, hysteresis is a desirable feature in stent design, for example. A superelastic stent should provide only a very light chronic outward force against a vessel wall, and at the same time be highly resistant to crushing, compliant in one direction, and stiff in the other. Moreover, a wide variety of SMA seismic applications take advantage of the hysterical properties of NiTiNOL for dampers and seismic insulators.

Fatigue resistance

It is well known that NiTiNOL offers exceptional fatigue resistance. Practically speaking, most fatigue environments in the body involve irregular cyclic motion against highly compliant tissue, and thus are a combination of stress and strain-control. Fatigue is also complicated by the superposition of a mean stress or strain on top of the cyclic component. As example of NiTiNOL fatigue study, Pelton et al. [32] tested the combined effects of cardiac pulsatile fatigue and vessel oversizing in vascular stents application. In particular, displacement controlled fatigue tests were performed and fatigue data were collected with combinations of simulated oversizing conditions and pulsatile cyclesm with both experimental and computational tools .

2.1.3 SMA application fields

SMA applications cover a wide variety of fields. Many alloy systems show shape memory behavior but only a few of them have been developed for a large scale market. Nowadays almost all the new SMA-applications are based on NiTiNOL or ternary NiTi-Cu and NiTi-Nb alloys (covering about the 90% of the SMA industrial applications). NiTiNOL SMA predominance is due to the improved strength and ductility with respect to other alloys. NiTiNOL SMA are available in the shape of thin wires and thin films, and presents an high electrical resistivity making electrical actuation reliable. Concerning to medical applications, NiTi SMA shows high biocompatibility and high resistance to corrosion. For these reasons, NiTiNOL SMA replaced Cu-based SMA although the industrial processes for the production results more difficult and expensive. Looking at the literature review on SMA applications, we partition between medical and non medical applications [25]. Medical applications include (for details readers may refer to [33, 34]):

- Cardiovascular surgery: starting from self-expanding stents (Fig. 2.6-*bottom left*), passing through embolic filters and transcatheter aortic valves (Fig. 2.6-*bottom right*), NiTiNOL is widely employed in minimally-invasive surgery;
- Orthopaedics: the principal applications include correction rods, compression staples and fracture fixators;
- Clinical instruments: there is a growing market for NiTiNOL clinical instruments, especially for biopsy forceps, guidewires, tissue ablators and retrieval baskets for laparoscopy;
- Ortodontic applications: NiTiNOL is widely employed for wires, palatal arches, distracters (Fig. 2.6-*top left*) and endodontic files;

- Other applications: birth control devices, laparoscopic inguinal hernioplasty, stapes prosthesis, colonic anastomosis are some of NiTiNOL devices developed in the last years;

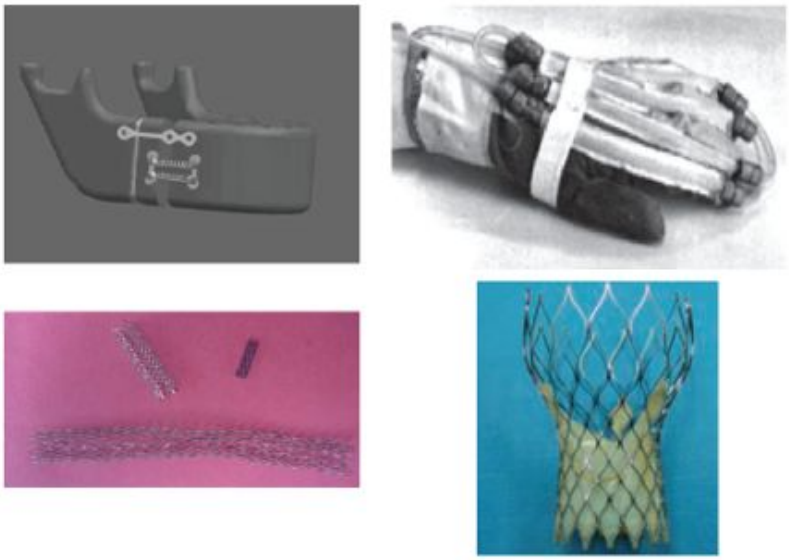

Figure 2.6 *Short overview of SMAs medical applications: (top left) Orthodontic distracters [35],(top right) Gloves with SMA wires [36], (bottom left) SMA stents [33], (bottom right) CoreValve aortic valve http://www.medtronic.com/corevalve/ous/index.html.*

Moving to non medical applications it is possible do identify the following applications:

- Fashion, decoration and gadgets: manufacturing of devices for ordinary life like eye glass frames (bow bridges and temples), frames for brassieres and antennas for portable cellular telephones;

- Couplings and fasteners: SMA are widely employed for heat-recoverable couplings, heat-to-shrink fasteners and connectors since the 70's. In fact, a coupling to connect titanium hydraulic tubing F-14 aircraft was the first large scale application of SMA in 1971;

- Microactuators: SMA properties can be exploited to realize thermal actuators. Following the subdivision given by Otsuka et al.[37] it is possible to subdivide SMA actuators in applications where the device is both sensor and actuator, and applications where the device only performs a complete controlled action. The first class includes ,e.g., water kettles with shape memory actuated heat cut off, coffee makers, thermal protection device. The second class includes, e.g., devices for the control of the environmental temperatures and flow control devices for air conditioners;

- Other applications: adaptive materials, hybrid composites and seismic devices that take advantage from the high damping properties of SMA.

2.2 SMA behavior: from experiments to constitutive modeling

In summary, SMA are caractherized by several features very attractive for a wide variety of industrial applications. However, given the complex thermomechanical interaction and the different non linear behaviors typical for such materials, the development of engineering tools to predict the SMA behavior is not a trivial task. As suggested by Arghavani [38], it is possible to partition the SMA behaviors into two categories:

- Primary effects, including pseudo-elasticity, shape memory effect as well as variant reorientation;
- Secondary effects, covering other effects which may turn out to be relevant in some practical cases.

The secondary effects include tension-compression asymmetry, different elastic moduli for austenite and martensite phases, progressive strain under cyclic loadings and thermal-mechanical coupling. As described in Section 2.1.1, contemporarily to experimental investigations, in the last decades a big effort was devoted to define constitutive models able to describe the main SMA behaviors. The main challenge for model theoretical conception and computational implementation is to predict the primary effects with regard also for secondary effects in relation with the practical implementation of the model. A satisfactory description of all these features is not trivial, and the task become even harder when the material behavior has to be "embedded" into a discrete framework for FEA. In particular, the constitutive model should be able, starting from experimental data (Fig. 2.7), to describe the macroscopic effects that could be important for the specific application. In fact, developing a 3D SMA model able to consider many SMA complex behaviors does not implies that the model is effective in engineering applications. To this end, besides research activities in SMA modeling, it is necessary to evaluate in advance which behaviors should be included into the model, according to engineering and computational requirements [38]. Many approaches to define the constitutive relations for SMA are available in the literature, but this section focuses on the procedure to obtain the SMA constitutive equations using a set of internal state variables. Thus, starting from the basics of Continuum Mechanics [40], the fundamental components are:

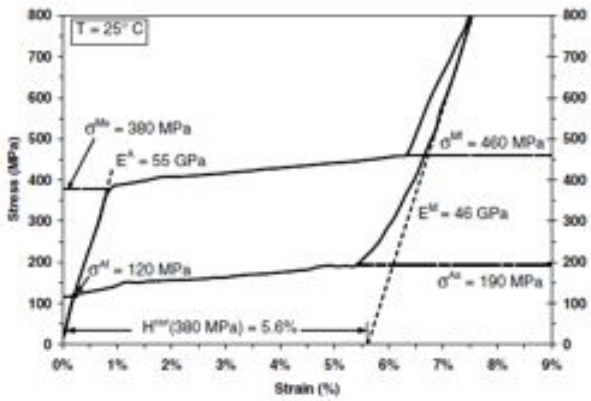

Figure 2.7 *Pseudoelastic loading/unloading results and derivation of parameters for various testing temperatures of 25 Celsius degrees. [39]*

- Kinematics: is the study of body configuration changes. Kinematics describes the geometry of motion and deformation of a body, without considering the cause of that motion and deformation;
- Equilibrium: is the study of the body equilibrium conditions. Equilibrium includes the relations for the measurement of the internal forces. This component can be described in terms of conservation laws (mass, linear momentum, angular momentum and energy);
- Constitutive relations: this component takes in account the phenomenological nature of the body. Constitutive equations are in general expressed as relations between internal forces and measures of the body configuration, like a bridge between equilibrium and kinematics.

This set of equations represents the fundamentals of mechanics of solids, and the introduction of the constitutive relations ensure the unicity of the solution [40]. Constitutive equations are mathematical constructs able to

describe the principal features of a material behavior. The SMA phase transition between different thermomechanical states can be described with the introduction of the so-called internal state variables, i.e., a set of additional unknowns aiming at describing the micromechanical SMA behavior. As suggested by Lagoudas et al. [39], the interaction between external and internal state variables can be described through the introduction of a thermodynamical potential. Four thermodynamical potentials are employed in the literature, i.e., the specific internal energy u, the specific Helmhotz free energy Ψ, the specific entropy η and the specific Gibbs free energy G. However, only Gibbs and Helmhotz free energies are commonly employed, given the difficulty to efficiently evaluate entropy and internal energy. Once the thermodynamical potential is defined, the main steps to derive a set of SMA constitutive relations are:

- Choice of internal state variables: the microstructural changes due to phase transformation should be represented with a set of internal variables. Different choices can deeply affect the model complexity, and the related features.

- Kinematics and thermomechanical assumptions: starting from experimental observations, it is possible to set some conditions to simplify the system, such as small strain regime or additive decompositions for the state variables.

- Evolution of Internal State Variables: in this step, the evolution laws for the internal variables are defined following the approach described by Simo and Hughes [41]. To define a rate-independent plasticity model, the evolutionary behavior of plastic strain must be defined with a relation called *flow rule*.

2.2.1 Review of Shape Memory alloys models.

As described in Section 2.2, the choice on representing the different combinations of primary and secondary effects strongly influences the performance and the applicability of a particular SMA constitutive model. For this reason, many SMA constitutive models are available in the literature, addressing different features and engineering applications. Following the classification suggested by Arghavani [38], SMA models can be classified into two big families:

- Models without internal variables
- Models with internal variables

Models without internal variables describe SMA behaviors without including quantities representing austenitic and martensitic mixture, using only strain, stress, temperature and entropy. Polynomial models [42] and hysteresis models [43] can be included in this family. The first describes the material behavior starting from a polynomial free energy function, which can be derived to get the constitutive equations, while the latter approach sets up the constitutive relations starting from mathematical properties, often neglecting the physical aspects underlying the material behavior. The introduction of internal variables to describe the material internal structure, in combination with the control variables (stress or strain, and thermal variables such as temperature and entropy) allows to describe the material constitutive relations, accounting for the physical phenomena underlying the experimental data. The internal variables typically include one or more phase fractions and/or macroscopic transformation strains. The first model based on internal variables was proposed in 1982 by Tanaka and Nagaki [44], it was characterized by an exponential hardening rule and

by the material properties remained constant during transformation phase. This model was theoretically studied for 3D problems, but its implementation was restricted to 1D problems, until Boyd and Lagoudas [45] extended the formulation, in order to permit the 3D implementation. In 90's, the growing number of SMA applications, in particular on biomedical applications, enhanced the creation of 3D phenomenological models (oriented to the computational testing of devices). 1D implementation remained active for the description of SMA's secondary effects, i.e., martensite volume fraction decomposition [46], in reason of its simplicity, and for the wide use of SMA wires in many applications . In this context, remarkable works are Raniecki and Lexcellent [47] and Leclercq and Lexcellent [48] models, able to describe the macroscopic thermo-mechanical behavior using two internal variables, in order to allow modeling of both detwinned and twinned martensite. In 1996 Lubliner and Auricchio considered a 3D response using a Drucker-Prager-type surface to describe the critical stresses for pseudoelastic transformation with exponential hardening law [49]. Moreover, this study was oriented to finite element implementation (this work is based on the generalized plasticity theory [50]). Souza et al. [21] proposed in 1998 a model able to describe the main features of polycrystalline shape memory materials for 3D implementation. Auricchio and Petrini improved this model, in order to increase its robusteness for finite element implementation [27]. Qidwai and Lagoudas [51] proposed a comprehensive modeling with tension-compression asymmetry, starting from the previous work of Boyd and Lagoudas [45].

Within this doctoral research, the constitutive laws proposed by Souza et al. [21] and the model introduced by Auricchio et al. [22] are considered and, in the following sections, both models are detailed. The notation of Auricchio-Taylor model has been slightly modified in order to make it

consistent with the Souza model notation in order to avoid confusing repetitions.

2.2.2 Souza 3D phenomenological model

Souza model, developed within the framework of phenomenological continuum thermodynamics [40], is able to describe pseudo elasticity and shape memory effect with a simple and robust solution algorithm based on return-map procedure [41].

Time-continuous model

The authors choose strain, $\boldsymbol{\varepsilon}$, and the absolute temperature, T, as control variables and the second-order transformation strain tensor, $\mathbf{e}^{tr}$, as internal variable. The model is developed under small strain assumption. The quantity $\mathbf{e}^{tr}$ has the role of describing the strain associated to the phase transformation. This variable is assumed to be traceless, in reason of experimental results indicating no volume changes during the phase transformation [52]. Furthermore, the value of trasformation strain norm (euclidean norm) is assumed to be always less than the value of ε_L, defined as the transformation strain norm value at the end of the transformation phase (ε_L, defined as a material parameter).

$$\|\mathbf{e}^{tr}\| \leq \varepsilon_L, \tag{2.2.1}$$

ε_L can be derived with a simple uniaxial test and it represents the value of transformation strain at the end of transformation phase. The following

additive decomposition is used for $\boldsymbol{\varepsilon}$:

$$\boldsymbol{\varepsilon} = \frac{\theta}{3}\mathbf{1} + \mathbf{e}, \tag{2.2.2}$$

where $\theta = \mathrm{tr}(\boldsymbol{\varepsilon})$ and $\mathbf{e}$ are, respectively, the volumetric and the deviatoric part of the total strain ε, while $\mathbf{1}$ is the second-order identity tensor. The free energy density function, or Helmholtz free energy Ψ, is defined to be the portion of the internal energy available for doing work at constant temperature, and represents the starting point for the development of different constitutive relations.
For a polycrystalline SMA material Ψ is expressed as

$$\begin{aligned}\Psi(\theta, \mathbf{e}, T, \mathbf{e}^{tr}) =& \frac{1}{2}K\theta^2 + G\|\mathbf{e} - \mathbf{e}^{tr}\|^2 - 3\alpha K\theta(T - T_0) + \beta\langle T - T_0\rangle\|\mathbf{e}^{tr}\| + \\ & \frac{1}{2}h\|\mathbf{e}^{tr}\|^2 + (u_0 - T\eta_0) + c\left[T - T_0 - T\log\left(\frac{T}{T_0}\right)\right] + \mathcal{I}_{\varepsilon_L}(\mathbf{e}^{tr}),\end{aligned} \tag{2.2.3}$$

where K and G are, respectively, the bulk and the shear modulus, α is

the thermal expansion coefficient, β is a material parameter associated with the stress-temperature relation, T_0 is the temperature below which only martensite phase is stable (M_f in Section 2.1.2), h is the hardening parameter associated with the transformation phase, c is the heat capacity, and u_0, η_0 and T_0 are, respectively, the internal energy, the entropy and the temperature at the reference state, while the symbol $\langle a\rangle$ is the positive part function. The component $\mathcal{I}_{\varepsilon_L}(\mathbf{e}^{tr})$ is set equal to an indicator function introduced to satisfy the previous constraint on the transformation strain

norm:

$$\mathcal{I}_{\varepsilon_L}(\mathbf{e}^{tr}) = \begin{cases} 0 & \text{if } \|\mathbf{e}^{tr}\| \leq \varepsilon_L \\ +\infty & \text{otherwise} \end{cases} \tag{2.2.4}$$

Differentiating the Ψ function with respect different arguments, it is possible to highlight the different stress components

$$\begin{cases} p &= \dfrac{\partial \Psi}{\partial \theta} &= K\left[\theta - 3\alpha(T - T_0)\right], \\ \mathbf{s} &= \dfrac{\partial \Psi}{\partial \mathbf{e}} &= 2G(\mathbf{e} - \mathbf{e}^{tr}), \\ \eta &= -\dfrac{\partial \Psi}{\partial T} &= \eta_0 + 3\alpha K\theta - \beta\|\mathbf{e}^{tr}\|\dfrac{\langle T - T_0\rangle}{|T - T_0|} + c\log\left(\dfrac{T}{T_0}\right), \\ \mathbf{X} &= -\dfrac{\partial \Psi}{\partial \mathbf{e}^{tr}} &= \mathbf{s} - \beta\langle T - T_0\rangle\dfrac{\mathbf{e}^{tr}}{\|\mathbf{e}^{tr}\|} - h\mathbf{e}^{tr} - \gamma\dfrac{\mathbf{e}^{tr}}{\|\mathbf{e}^{tr}\|}, \end{cases} \tag{2.2.5}$$

$\mathbf{s}$ and p represent, respectively, the deviatoric and the volumetric part of the stress. $\mathbf{X}$ represents a stress-like quantity related to transformation strain and can be considered as the driving force for phase transformations processes. It is important to note that if $\mathbf{e}^{tr} = \mathbf{0}$ the transformation stress $\mathbf{X}$ is undetermined. To overcome this issue the authors proposed this different definition for $\mathbf{X}$, in the step of nucleation of the product phase

$$\mathbf{X} = R\frac{\mathbf{s}}{\|\mathbf{s}\|} \tag{2.2.6}$$

where R is a positive material parameter that can be defined as the radius of the elastic domain. This relation can be proved with the assumption of an hypothetical process starting with $\mathbf{e}^{tr} = \mathbf{0}$ and $\dot{\mathbf{e}}^{tr} \neq \mathbf{0}$. Assuming that $\|\mathbf{s} - \mathbf{X}\| = \beta\langle T - T_0\rangle + h\|\mathbf{e}^{tr}\|$ holds for $\mathbf{e}^{tr}$ in a neighborhood of zero,

it follows by continuity that $\|\|\mathbf{s}-\mathbf{X}\| = \beta\langle T - T_0\rangle$. Therefore, if phase transformation is expected there will be

$$\|\mathbf{S}\| = \|\|\mathbf{s}-\mathbf{X}+\mathbf{X}\| \leq \|\mathbf{s}-\mathbf{X}\| + \|\mathbf{X}\| = \beta\langle T - T_0\rangle + R \tag{2.2.7}$$

this relation is obtained taking in account the transformation, leads to

$\|\mathbf{X}\| \ = R$.

The flow rule for the internal variable and the classical Kuhn-Tucker conditions take the form

$$\dot{\mathbf{e}}^{tr} = \dot{\zeta}\frac{\partial F}{\partial \mathbf{X}} = \dot{\zeta}\frac{\mathbf{X}}{\|\mathbf{X}\|}, \tag{2.2.8}$$

$$\begin{cases} \dot{\zeta} \geq 0, \\ F \leq 0, \\ \dot{\zeta}F = 0. \end{cases} \tag{2.2.9}$$

where $\dot{\zeta}$ plays a role similar to the plastic consistent parameter.

The strict inequality in Equation (2.2.7) is not consistent, because the flow rule imposes that $\dot{\mathbf{e}}^{tr}$ must have the same direction of $\|\mathbf{X}\|$, and $\mathbf{e}^{tr}$ as well, when integrated in a short process. This is impossible because $\mathbf{e}^{tr}$ should point toward $\|\mathbf{s}\text{-}\mathbf{X}\|$. Moving back to the model description, the derivation of $\mathcal{I}_{\varepsilon_L}(\mathbf{e}^{tr})$ creates the variable γ defined such that

$$\begin{cases} \gamma = 0 & if\ \|\mathbf{e}^{tr}\| < \varepsilon_L, \\ \gamma \geq 0 & if\ \|\mathbf{e}^{tr}\| = \varepsilon_L, \\ \partial\mathcal{I}_{\varepsilon_L}(\mathbf{e}^{tr}) = \gamma\mathbf{e}^{tr}/\|\mathbf{e}^{tr}\| \end{cases} \tag{2.2.10}$$

while the yielding is ruled by the following limit function

$$F(\mathbf{X}) = \|\mathbf{X}\| - R, \tag{2.2.11}$$

Auricchio and Petrini modifications

Auricchio and Petrini [27] introduced some modifications in the Souza model described in the previous section, in order to improve the model robustness for FEA applications. The transformation stress $\mathbf{X}$ dependance on the derivative of the transformation strain has been highlighted as a critical point when $\mathbf{e}^{tr}$ is close to 0, making $\mathbf{X}$ undefined. To overcome this issue, the authors proposed to replace the Euclidean norm $\|\mathbf{e}^{tr}\|$ with the regularized norm $\overline{\|\mathbf{e}^{tr}\|}$, defined as:

$$\overline{\|\mathbf{e}^{tr}\|} = \|\mathbf{e}^{tr}\| - \frac{\delta^{\delta+1/\delta}}{\delta - 1}(\|\mathbf{e}^{tr}\| + \delta)^{\delta-1/\delta} \tag{2.2.12}$$

where δ is a user-defined parameter which controls the smoothness of the regularized norm. Thus, the quantity $\overline{\|\mathbf{e}^{tr}\|}$ is always differentiable, even for $\|\mathbf{e}^{tr}\| = \mathbf{0}$. Moreover, the authors introduced another form for the yielding function $F(\mathbf{X})$, as function of second (J_2) and third (J_3) invariants of the transformation stress tensor $\mathbf{X}$

$$F(\mathbf{X}) = \sqrt{2J_2} + m\frac{J_3}{J_2} - R \tag{2.2.13}$$

$$J_2 = \frac{1}{2}((\mathbf{X}^2 : \mathbf{1}) \tag{2.2.14}$$

$$J_3 = \frac{1}{3}((\mathbf{X}^3 : \mathbf{1}) \tag{2.2.15}$$

where m is a material parameter. Both R and m can be associated to the uniaxial critical stress in tension σ_t and in compression σ_c by the relations

$$R = 2\sqrt{\frac{2}{3}}\frac{\sigma_t \sigma_c}{\sigma_c + \sigma_t} \tag{2.2.16}$$

$$m = \sqrt{\frac{27}{2}}\frac{\sigma_c - \sigma_t}{\sigma_c + \sigma_t} \tag{2.2.17}$$

This approach is used in order to introduce the tension-compression asymmetry observed in SMA and the material is modeled as isotropic with a Prager - Lode type limit function.

Time-discrete model and solution algorithm

The constitutive model consists of a non-linear equation system, treated by Auricchio and Petrini [27] as an implicit time-discrete strain-driven problem. The adopted convention, for sake of notation simplicity, states that the pedix n is used for all the variables evaluated at $t = t_n$ and no pedix is used for variables evaluated at time $t = t_{n+1}$. Known the solution at the time t_n and the strain tensor at the time t_{n+1}, an implicit backward Euler method is used to integrate the model rate equations; the stress history is then derived from the strain history by means of a procedure known as return-map. Initially suggested by Maenchen and Sack [53] for the solution of plasticity formulations, the return map provides an efficient and robust integration scheme based on a discrete enforcement of the evolutionary equations [41]. Using this integration scheme, the discrete framework is structured as follows

$$
\begin{cases}
p = K[\theta - 3\alpha(T - T_0)] \\
\mathbf{s} = 2G(\mathbf{e} - \mathbf{e}^{tr}) \\
\mathbf{X} = \mathbf{s} - \beta\langle T - T_0\rangle \dfrac{\mathbf{e}^{tr}}{\|\mathbf{e}^{tr}\|} - h\mathbf{e}^{tr} - \gamma \dfrac{\mathbf{e}^{tr}}{\|\mathbf{e}^{tr}\|} \\
\gamma \geq 0 \\
\mathbf{e}^{tr} = \mathbf{e}_n^{tr} + \Delta\zeta \dfrac{\mathbf{X}}{\|\mathbf{X}\|} \\
\|\mathbf{e}^{tr}\| \leq \varepsilon_L \\
F(\mathbf{X}) = \|\mathbf{X}\| - R \leq 0 \\
\Delta\zeta \geq 0, \quad \Delta\zeta F(\mathbf{X}) = 0
\end{cases}
\tag{2.2.18}
$$

The return-map scheme belongs to a family of the two stages, elastic-

predictor plastic-corrector methods. The first stage belongs to the elastic predictor, a purely elastic *trial state* is computed; the second one is computed using the trial state as initial condition, if the trial state violates the constitutive conditions. For this model, the trial state is evaluated for "frozen" internal variables. A trial limit function is computed and compared with the condition described in Equation (2.2.11). If such a condition is violated, the step is considered inelastic and the evolution equations need to be integrated. To treat an inelastic step, the problem is formulated in residual form, in order to solve the non linear equation system with a Newton-Raphson method. It is important to remark that an inelastic state could be related to an unsaturated or a saturated condition, and the discrete model has also to be able to distinguish them with a proper procedure. The procedure starts with the assumption of $\|\mathbf{e}^{tr}\| < \varepsilon_L$, which implies $\gamma = 0$, and consists in an unsatured condition. Within this case, the residuals take the following form

$$\begin{aligned}
&\mathbf{R}^X = \mathbf{X} - \mathbf{s}^{TR} + \beta\langle T - T_0\rangle \frac{\partial \overline{\|\mathbf{e}^{tr}\|}}{\partial \mathbf{e}^{tr}} + h\mathbf{e}^{tr} = \mathbf{0}, \\
&R^{\Delta\zeta} = \|\mathbf{X}\| - R = 0.
\end{aligned} \tag{2.2.19}$$

It is possible now to solve the seven non-linear scalar equations with a Newton-Raphson method to find the seven scalar unknowns, (six components of $\mathbf{X}$ and $\Delta\zeta$). At this point, the solution is checked to evaluate its admissibility. If the solution is not admissible (i.e., $\|\mathbf{e}^{tr}\| > \varepsilon_L$), the state consists in a saturated condition (i.e., $\|\mathbf{e}^{tr}\| = \varepsilon_L$), which implies $\gamma > 0$, and the sytem in residual form becomes:

$$\begin{aligned}
&\mathbf{R}^X = \mathbf{X} - \mathbf{s}^{TR} + \beta\langle T - T_0\rangle \frac{\partial \overline{\|\mathbf{e}^{tr}\|}}{\partial \mathbf{e}^{tr}} + h\mathbf{e}^{tr} + \gamma\frac{\mathbf{e}^{tr}}{\|\mathbf{e}^{tr}\|} = \mathbf{0}, \\
&R^{\Delta\zeta} = \|\mathbf{X}\| - R = 0, \\
&R^{\gamma} = \|\mathbf{e}^{tr}\| - \varepsilon_L = 0.
\end{aligned} \tag{2.2.20}$$

In this case, the Newton-Rapshon method is employed to find eight unknowns, constituted by the six components of $\mathbf{X}$, $\Delta\zeta$, and γ (for the details about the form of the consistent tangent matrix please refer to [27]).

2.2.3 Auricchio-Taylor model

Auricchio-Taylor-Lubliner model (Auricchio-Taylor model in the following) is developed within the generalized plasticity framework [50] and represents the built-in constitutive model to reproduce pseudolastic materials undergoing solid-solid phase transitions in the majority of FEA commercial softwares. The model is able to reproduce the direct and reverse transitions between austenite phase (A) and single-variant martensite phase (S). In particular, the model considers three different conditions:

- conversion of austenite into single-variant martensite (A $\rightarrow$ S)
- conversion of single-variant martensite into austenite (S $\rightarrow$ A)
- single-variant martensite reorientation (S $\rightarrow$ S)

The different solid-solid phase transitions are defined within a specific thermo-mechanical range. In particular, the thermo-mechanical limits for each phase transition are defined by mean of the following scalar functions:

Austenite-Martensite transition (A $\rightarrow$ S)

$$F^{AS}(\boldsymbol{\sigma}, T) = \|\mathbf{s}\| + 3\pi\, p - C^{AS} T$$

where $\mathbf{s}$ is the deviatoric part of the stress (defined as: $\mathbf{s} = \boldsymbol{\sigma} - \mathrm{tr}(\boldsymbol{\sigma})\mathbf{1}/3$), p is the pressure, C^{AS} and π are material parameters and $\|\cdot\|$ indicates the Euclidean norm. The initial and final transformation function can be expressed as:

$$\begin{aligned} F_s^{AS} &= F^{AS} - R_s^{AS} \\ F_f^{AS} &= F^{AS} - R_f^{AS} \end{aligned}$$

with:

$$\begin{aligned} R_s^{AS} &= \left[\sigma_s^{AS}\left(\sqrt{\frac{2}{3}} + \pi^{AS}\right) - C^{AS} T_s^{AS}\right] \\ R_f^{AS} &= \left[\sigma_f^{AS}\left(\sqrt{\frac{2}{3}} + \pi^{AS}\right) - C^{AS} T_f^{AS}\right] \end{aligned}$$

where σ_s^{AS}, σ_f^{AS}, T_s^{AS} and T_f^{AS} are all material parameters.
The conditions for the conversion of austenite into single-variant martensite

are:

$$F_s^{AS} > 0 \ , \quad F_f^{AS} < 0 \ , \quad \dot{F}^{AS} > 0 \tag{2.2.21}$$

and that the scaled transformation strain corresponding to the $A \to S$ phase transformation evolves as follows:

$$\dot{\boldsymbol{u}}^{AS} = \dot{\xi}_S^{AS} \boldsymbol{N}^{AS} \tag{2.2.22}$$

where:

$$\boldsymbol{N}^{AS} = \frac{\boldsymbol{M}^{AS}}{\|\boldsymbol{M}^{AS}\|} \qquad , \qquad \boldsymbol{M}^{AS} = \frac{\partial F^{AS}}{\partial \boldsymbol{\sigma}} \tag{2.2.23}$$

for the evolution of the single-variant martensite fraction the author the following linear form:

$$\dot{\xi}_S^{AS} = -H^{AS}(1 - \xi_S)\frac{\dot{F}^{AS}}{F_f^{AS}}$$

The scalar parameter H^{AS} embeds the conditions for the activation of the phase transformation and it is defined by the relation:

$$H^{AS} = \begin{cases} 1 & \text{if} \quad F_s^{AS} > 0 \ , \ \ F_f^{AS} < 0 \ , \ \ \dot{F}^{AS} > 0 \\ 0 & \text{otherwise} \end{cases} \tag{2.2.24}$$

Martensite-Austenite transition (S $\to$ A)

Similarly to the above, a Drucker-Prager-type loading function is introduced:

$$F^{SA}(\boldsymbol{\sigma}, T) = \|\mathbf{s}\| + 3\pi\, p - C^{SA} T$$

where C^{SA} is a material parameter. The initial and final transformation function can be expressed as:

$$\begin{aligned} F_s^{SA} &= F^{SA} - R_s^{SA} \\ F_f^{SA} &= F^{SA} - R_f^{SA} \end{aligned}$$

with:

$$\begin{aligned} R_s^{SA} &= \left[\sigma_s^{SA}\left(\sqrt{\frac{2}{3}} + \pi^{SA}\right) - C^{SA}T_s^{SA}\right] \\ R_f^{SA} &= \left[\sigma_f^{SA}\left(\sqrt{\frac{2}{3}} + \pi^{SA}\right) - C^{SA}T_f^{SA}\right] \end{aligned}$$

where σ_s^{SA}, σ_f^{SA}, T_s^{SA}, T_f^{SA} are all material parameters.
The conditions for the conversion of single-variant martensite into austenite are:

$$F_s^{SA} < 0 \ , \quad F_f^{SA} > 0 \ , \quad \dot{F}^{SA} < 0 \tag{2.2.25}$$

and that the scaled transformation strain corresponding to the $S \rightarrow A$ phase transformation evolves as follows:

$$\dot{\boldsymbol{u}}^{SA} = \dot{\xi}_S^{SA}\boldsymbol{N}^{SA} \tag{2.2.26}$$

where:

$$\boldsymbol{N}^{SA} = \frac{\boldsymbol{u}}{\|\boldsymbol{u}\|} \tag{2.2.27}$$

Again, the evolution of the single-variant martensite fraction assumes the following linear form:

$$\dot{\xi}_S^{SA} = H^{SA}\xi_S\frac{\dot{F}^{SA}}{F_f^{SA}} \tag{2.2.28}$$

The scalar parameter H^{SA} embeds the conditions for the phase transformation and it is defined by the relation:

$$H^{SA} = \begin{cases} 1 & \text{if} \quad F_s^{SA} < 0\ , \quad F_f^{SA} > 0\ , \quad \dot{F}^{SA} < 0 \\ 0 & \text{otherwise} \end{cases} \tag{2.2.29}$$

For later developments, it is important to remark that the conversion of martensite into austenite is associated only with a rescaling of the transformation strain $\boldsymbol{u}$.

Martensite reorientation (S $\rightarrow$ S)

To model the single-variant martensite reorientation process for non-proportional changes of stress (changes of direction or rotation), the loading function is expressed as

$$\begin{aligned} F^{SS}(\boldsymbol{\sigma}, T) &= \|\mathbf{s}\| + 3\pi p - C^{SS}T \\ F_s^{SS} &= F^{SS} - R_s^{SS} \end{aligned}$$

with:

$$R_s^{SS} = \left[\sigma_s^{SS} \left(\sqrt{\frac{2}{3}} + \pi \right) - C^{SS} T_s^{SS} \right] \tag{2.2.30}$$

where C^{SS}, σ_s^{SS} and T_s^{SS} are material parameters.

The condition for the activation of the reorientation process are:

$$F_s^{SS} > 0 \quad , \quad \dot{\boldsymbol{N}}^{SS} \neq \mathbf{0} \tag{2.2.31}$$

where:

$$\boldsymbol{N}^{SS} = \frac{\boldsymbol{M}^{SS}}{\|\boldsymbol{M}^{SS}\|} \qquad , \qquad \boldsymbol{M}^{SS} = \frac{\partial F^{SS}}{\partial \boldsymbol{\tau}}$$

and that the scaled transformation strain corresponding to the SS phase transformation evolves as follow:

$$\dot{\boldsymbol{u}}^{SS} = H^{SS} \xi_S \dot{\boldsymbol{N}}^{SS} \tag{2.2.32}$$

where:

$$H^{SS} = \begin{cases} 1 & \text{if} \quad F_s^{SS} > 0 \\ 0 & \text{otherwise} \end{cases} \tag{2.2.33}$$

The authors assume that, from a physical point of view it seems plausible that whenever the material has enough energy to induce a conversion of austenite into single-variant martensite, then it has also enough energy to reorient the martensite fraction already present. Hence, we set $C^{AS} = C^{SS}$ and $R_s^{AS} = R_s^{SS}$, such that $F_s^{AS} = F_s^{SS}$. Moreover, recalling the expression for F^{AS} and F^{SS}

$$\boldsymbol{M}^{AS} = \boldsymbol{M}^{SS} = \frac{\mathbf{s}}{\|\mathbf{s}\|} + \pi \mathbf{1} = \boldsymbol{M} \tag{2.2.34}$$

$$\boldsymbol{N}^{AS} = \boldsymbol{N}^{SS} = \frac{1}{1+3\alpha}\left(\frac{\mathbf{s}}{\|\mathbf{s}\|} + \pi \mathbf{1}\right) = \boldsymbol{N} \tag{2.2.35}$$

Starting from this assumption can the rate equations for the scaled transformation strain can be computed, obtaining the following equation:

$$\boldsymbol{u} = \xi_S \, \hat{\boldsymbol{N}} \tag{2.2.36}$$

where $\hat{\boldsymbol{N}}$ is the current value of $\boldsymbol{N}$ if $H^{SS} = 1$, otherwise it is equal to the last value of $\boldsymbol{N}$ attained when H^{SS} was equal to 1.

The interaction of the different loading functions, F^i, ${F_s}^i$, ${F_f}^i$ (with $i = \{A \to S,\ S \to A,\ S \to S\}$), define the three different phase transitions. In the following, for the sake of simplicity, only the small-deformation setting of the model is presented (for the large-displacement model, the reader may refer to [23]).

Time-continous model

The authors choose to additively decompose the strain ε into an elastic part, ε^e, and a transformation strain ε^{tr}

$$\boldsymbol{\varepsilon} = \boldsymbol{\varepsilon}^e + \boldsymbol{\varepsilon}^{tr} \tag{2.2.37}$$

where

$$\boldsymbol{\varepsilon}^{tr} = \varepsilon_L \mathbf{u} \tag{2.2.38}$$

being ε_L a material parameter. The authors assume the strain $\boldsymbol{\varepsilon}$ and the temperature T as control variables. Moreover, the authors choose the transformation strain $\boldsymbol{\varepsilon}^{tr}$ and the single variant martensite volume fraction ξ_S as internal variables. A free-energy function, quadratic in the elastic strain, is considered:

$$\Psi = \Psi(\boldsymbol{\varepsilon}) = \frac{1}{2}\boldsymbol{\varepsilon}\boldsymbol{D}^e\boldsymbol{\varepsilon} \tag{2.2.39}$$

where $\boldsymbol{D}^e$ is the fourth-order rank elastic modulus tensor. Accordingly, the stress $\boldsymbol{\sigma}$ is given by:

$$\boldsymbol{\sigma} = \frac{\partial \Psi}{\partial \boldsymbol{\varepsilon}} = \boldsymbol{D}^e\boldsymbol{\varepsilon}^e = \boldsymbol{D}^e(\boldsymbol{\varepsilon}^e - \boldsymbol{\varepsilon}_L\boldsymbol{u}) \tag{2.2.40}$$

Recalling the Drucker-Prager form of the loading functions and the hypothesis of isotropy and assuming the elastic tensor $\boldsymbol{D}$ to be constant and isotropic, it is convenient to split the equations into the volumetric and the deviatoric components. Recalling part of the notation introduced in Section 2.2.2 we have:

$$\boldsymbol{\varepsilon} = \frac{\theta}{3}\mathbf{1} + \mathbf{e}, \tag{2.2.41}$$

$$\boldsymbol{\varepsilon}^e = \frac{\theta^e}{3}\mathbf{1} + \mathbf{e}^e, \tag{2.2.42}$$

$$\boldsymbol{\varepsilon}^{tr} = \frac{\pi}{3}\mathbf{1} + \mathbf{e}^{tr}, \tag{2.2.43}$$

$$\mathbf{e} = \mathbf{e}^e + \varepsilon_L \xi_S \mathbf{e}^{tr} \tag{2.2.44}$$

$$\theta = \theta^e + 3\pi\, \epsilon_L\, \xi_S \tag{2.2.45}$$

and:

$$w = 3\pi\, \xi_S \tag{2.2.46}$$

$$\boldsymbol{v} = \xi_S\, \mathbf{e}^{tr} \tag{2.2.47}$$

$$p = K\, \theta^e = K\,(\theta - \epsilon_L w) \tag{2.2.48}$$

$$\mathbf{s} = 2G\, \boldsymbol{e}^e = 2G\,(\boldsymbol{e} - \epsilon_L \boldsymbol{v}) \tag{2.2.49}$$

where K is the bulk modulus and G is the shear modulus.

Time-discrete model and solution algorithm

As for the Souza model, the authors, in order to minimize the appearance of subscripts (and to make the equations more readable), introduce the convention:

$$\boldsymbol{a}_n = \boldsymbol{a}(t_n) \ , \quad \boldsymbol{a} = \boldsymbol{a}(t_{n+1})$$

where $\boldsymbol{a}$ is any generic quantity. Therefore, the subscript n indicates a quantity evaluated at time t_n, while no subscript indicates a quantity evaluated at time t_{n+1}. Using a backward-Euler integration formula, the discrete forms of equations are given by:

$$w = 3\pi\, \xi_S \tag{2.2.50}$$

$$\boldsymbol{v} = \xi_S\, \mathbf{e}^{tr} \tag{2.2.51}$$

$$\xi_S = \xi_{S,n} + \left(\lambda_S^{AS} + \lambda_S^{SA}\right) \tag{2.2.52}$$

where:

$$\lambda_S^{AS} = \int_{t_n}^{t_{n+1}} \dot{\xi}_S^{AS} dt \tag{2.2.53}$$

$$\lambda_S^{SA} = \int_{t_n}^{t_{n+1}} \dot{\xi}_S^{SA} dt \tag{2.2.54}$$

Similarly, using a backward-Euler scheme to integrate the time-continuous evolutionary equations yields the corresponding time-discrete evolutionary equations. Written in residual form and after clearing fractions, the time-discrete evolutionary equations specialize to:

$$\mathcal{R}^{AS} = F_f^{AS}\lambda_S^{AS} + H^{AS}(1-\xi_S)\left(F^{AS} - F_n^{AS}\right) = 0 \tag{2.2.55}$$

$$\mathcal{R}^{SA} = F_f^{SA}\lambda_S^{SA} - H^{SA}\,\xi_S\ \left(F^{SA} - F_n^{SA}\right) = 0 \tag{2.2.56}$$

The quantities λ_S^{AS} and λ_S^{SA} can be computed expressing F^{AS} and F^{SA} as functions of λ_S^{AS} and λ_S^{SA} and requiring the satisfaction of $\mathcal{R}^{AS}$ and $\mathcal{R}^{SA}$. As for the Souza model, a return-map algorithm is used as the integration scheme for the time-discrete model. It belongs to the family of elastic-predictor/inelastic-corrector algorithms and, hence, is a two-part algorithm. In the first part, a purely elastic *trial state* is computed; in the second part, if the trial state violates the constitutive model, an *inelastic correction* is computed using the trial state as an initial condition. The details of the algorithm for the time-discrete model proposed here are:

1. **Trial state.**
   Assume that no phase transformations occur (i.e. $w = w_n$, $\boldsymbol{v} = \boldsymbol{v}_n$, $\xi_S = \xi_{S,n}$, $\lambda_S^{AS} = \lambda_S^{SA} = 0$). Accordingly, compute the trial pressure and the trial deviatoric part of the stress:

$$\begin{aligned} p^{TRIAL} &= K(\theta - \varepsilon_L w_n) \\ \mathbf{s}^{TRIAL} &= 2G\,(\mathbf{e} - \varepsilon_L \boldsymbol{v}_n) \end{aligned}$$

2. **Check reorientation process (SS).**
   Compute F_s^{SS}
   If $F_s^{SS} > 0$ then
   set $H^{SS} = 1$
   update w, ε^{tr} and $\boldsymbol{v}$
   recompute p^{TRIAL} and $\mathbf{s}^{TRIAL}$
   else
   set $H^{SS} = 0$
   end if

3. Check solutions with $\xi_S = 0$ and $\xi_S = 1$.

Compute $F^{AS}\big|_{\xi_S=1}$ and $F^{SA}\big|_{\xi_S=0}$

If $F^{AS}\big|_{\xi_S=1} > R_f^{AS}$ then

$\xi_S = 1$ is the appropriate solution

solution found

set $H^{AS} = 1$

else

$\xi_S = 1$ is not the appropriate solution

end if

If $F^{SA}\big|_{\xi_S=0} < R_f^{SA}$ then

$\xi_S = 0$ is the appropriate solution

solution found

else

$\xi_S = 0$ is not the appropriate solution

end if

If solution found then skip to 7

4. Check $A \to S$ transformation.

Compute F^{AS}, F_s^{AS} and F_n^{AS}

If $F_s^{AS} > 0$, $F^{AS} > F_n^{AS}$ and $\xi_{S,n} < 1$ then

set $H^{AS} = 1$

else

set $H^{AS} = 0$

end if

5. Check $S \to A$ transformation.

Compute F^{SA}, F_s^{SA} and F_n^{SA}

If $F_s^{SA} < 0$, $F^{SA} < F_n^{SA}$ and $\xi_{S,n} > 0$ then

set $H^{SA} = 1$

else

set $H^{SA} = 0$

end if

6. Compute martensite evolution.

If $H^{AS} = 1$ or $H^{SA} = 1$ then

compute λ_S^{AS} and λ_S^{SA}

update ξ_S, $\boldsymbol{v}$, w, p and $\mathbf{s}$

end if

7. Compute algorithmic tangent.

If $H^{AS} = 1$ or $H^{SA} = 1$ or $H^{SS} = 1$ then

compute algorithmic inelastic tangent

(for details reader may refer to [23])

else

compute elastic tangent

end if

2.3 Model calibration

Souza model

Auricchio et al. [54] defined a simple methodology to calibrate the parameters for the Souza model. The experimental data is based on the comparison between two thermal cycling tests at constant stress (figure 2.8).

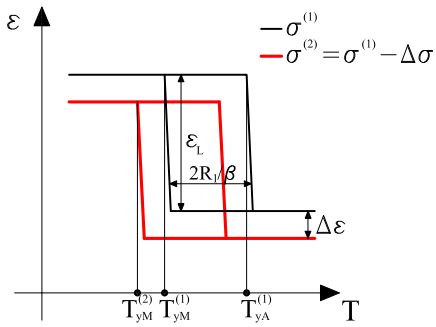

Figure 2.8 *Two strain-temperature curves at two constant stresses $\sigma^{(1)} > \sigma^{(2)}$.[55]*

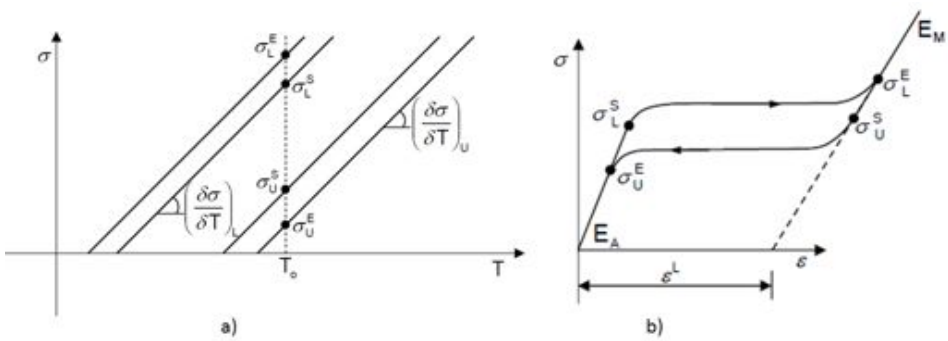

Figure 2.9 *a) stress-temperature phase diagram, b) stress-strain curve sketch. Both figures highlight the physical interpretation of some material parameters*

The identification of ε_L is trivial and corresponds to the strain associated to the plateau phase in the diagram. E and β are defined, respectevely, as $\dfrac{\partial\sigma}{\partial\varepsilon}$ and $\dfrac{\partial\sigma}{\partial T}$ (see figure 2.9). Such parameters can be estimated starting from Fig.2.8 defining $\Delta T = T_{yM}^{(1)} - T_{yM}^{(2)}$ and $\Delta\sigma = \sigma^{(1)} - \sigma^{(2)}$. The elastic radius parameter R can be derived in two ways, depending on the experimental data and the characteristic of limit function. In fact, classic Souza model uses Equation (2.2.11) as limit function, and the elastic radius can be derived subtracting the two relations

$$\begin{cases} \sigma - \beta(T_{yM} - T_0) = R, \\ \sigma - \beta(T_{yA} - T_0) = -R. \end{cases} \tag{2.3.1}$$

On the other hand, if Auricchio and Petrini improvements are implemented, the elastic radius can be calculated with Equation (2.2.16).

Concerning to hardening parameter h, starting from

$$\frac{\partial\sigma}{\partial\varepsilon} = \frac{Eh}{E+h} \tag{2.3.2}$$

and

$$\frac{\partial\sigma}{\partial\varepsilon} = \frac{\partial\sigma}{\partial T}\frac{\partial T}{\partial\varepsilon} = \beta\,\frac{\partial T}{\partial\varepsilon} \tag{2.3.3}$$

with simple computations it can be found that

$$h = \left(\frac{1}{\beta}\frac{\partial\varepsilon}{\partial T} - \frac{1}{E}\right)^{-1} \tag{2.3.4}$$

Finally, to compute T_0, the following expression, directly derived from $\sigma^{(1)}-$

$\beta(T_{yM}^{(1)} - T_0) = R$, can be used

$$T_0 = T_{yM}^{(1)} + \frac{R - \sigma^{(1)}}{\beta}.$$

Auricchio-Taylor model

Moving to the Auricchio-Taylor model, the material parameter set is obtained integrating properly different information:

- some material parameter, such as E^A, E^M, ν, C^{AS}, C^{SA} are derived straightforwardly from Souza model parameters;
- other *thermic* parameters, i.e., T_s^{AS}, T_s^{SA}, T_f^{AS}, T_f^{SA}, are obtained from the work of Hartl et al. [56], referring to the same experimental data (S3T Roundobin activity);
- the remaining parameters are obtained elaborating some parameter of Souza model as discussed in the following.

The parameter ε_L has different physical interpretation within the two models. In fact, while in the Souza model ε_L is defined as the maximum value of the transformation strain norm during an uniaxial test, within the Auricchio-Taylor model it is defined as the maximum uniaxial transformation strain. Consequently, it is possible to manipulate the equations in order to obtain a coefficient able to relate these two parameters. In fact, starting from a simple uniaxial process, the stress tensor is defined as:

$$\sigma = \begin{bmatrix} \sigma & 0 & 0 \\ 0 & 0 & 0 \\ 0 & 0 & 0 \end{bmatrix} \tag{2.3.5}$$

and the related deviatoric stress tensor is

$$\mathbf{s} = \begin{bmatrix} \frac{2}{3} & 0 & 0 \\ 0 & -\frac{1}{3} & 0 \\ 0 & 0 & -\frac{1}{3} \end{bmatrix} \sigma \tag{2.3.6}$$

resuming the flow rule of Souza model, we remark that the transformation strain evolution is ruled by the ratio $\mathbf{n} = \frac{\mathbf{s}}{\|\mathbf{s}\|}$. The substitution of Equation (2.3.6) in the previous ratio gives

$$\mathbf{n} = \sqrt{\frac{9}{6}} \begin{bmatrix} \frac{2}{3} & 0 & 0 \\ 0 & -\frac{1}{3} & 0 \\ 0 & 0 & -\frac{1}{3} \end{bmatrix} \tag{2.3.7}$$

and the uniaxial component n_{11} is

$$n_{11} = \frac{2}{3}\sqrt{\frac{9}{6}} = \sqrt{\frac{2}{3}} \tag{2.3.8}$$

Auricchio model employes n_{11} as reference to find ε_L and, consequently, the coefficient that relates the maximum transformation strain norm and the its uniaxial value, is exactly $\sqrt{\frac{2}{3}}$. For these tests $\varepsilon_L = 0.056$ and the

associated $H = 0.046 = 0.056\sqrt{\frac{2}{3}}$.
Moreover, the Auricchio model requires 4 stress values related to the transformation phase (see Fig. 2.9). To overcome this issue, we performed a simple pseudoelastic FEA using the Souza model, estimating then the 4 stress values from the obtained curve. The estimated values of σ_s^{AS},σ_f^{AS},σ_s^{SA} and σ_f^{SA} are extrapolated from the FEA uniaxial test and must be rescaled because they are referred to the reference temperature value T_0.

2.4 Numerical examples

In this section, the proposed constitutive models are evaluated by mean of different boundary value problems, accounting for different SMA behaviors and engineering complexity. The Souza model is implemented as a User Material subroutine (UMAT) for the FEA solver Abaqus/Standard, while the Auricchio-Taylor model is already available as built-in material subroutine for the same solver. The material parameters are obtained with the procedure described in Section 2.3 starting from the experimental data carried out on SMA wires within S3T Roundrobin SMA modeling activities [57].

2.4.1 Pseudoelastic cube test

At first, we performed a simple pesudoelastic test (loading-unloading at constant temperature) on a cube discretized with 1000 C3D8 elements (Fig.2.10). This test is performed in order to demonstrate that an increasing computational complexity cannot invalidate the subroutine features. The results (see Fig. 2.11) show that all the constitutive models keep the same behavior of the same test performed on a single cubic element.

Table 2.1 *Souza material parameters.*

E	Elastic modulus	53000 MPa
ν	Poisson's ratio	0.33
h	Linear hardening parameter	1000 MPa
β	Stress-temperature relation parameter	2.1 MPa/K
T_0	Reference temperature	245 K
σ_c	Critical traction stress	72 MPa
σ_t	Critical compression stress	56 MPa
ε_L	Maximum trasfromation strain norm	5.6 %
M_f	Martensite finish temperature	223 K
M_s	Martensite starting temperature	239 K
A_f	Austenite finish temperature	260 K
A_s	Austenite starting temperarut	2248 K
α	Thermal expansion coefficient	$10^{-6}\ K^{-1}$
δ	Regularized norm coefficient	10^{-4}

Table 2.2 *Auricchio-Taylor material parameters.*

E^A	Austenite Elastic modulus	53000 MPa
E^M	Martensite Elastic modulus	53000 MPa
ν	Poisson's ratio	0.33
σ_s^{AS}	Start of transformation loading	142 MPa
σ_f^{AS}	End of transformation loading	282 MPa
σ_s^{SA}	Start of transformation unloading	92 MPa
σ_f^{SA}	End of transformation unloading	-108 MPa
$C^{AS} = (\frac{\partial \sigma}{\partial T})_{AS}$	Loading stress-temperature coefficient	6.1 MPa K^{-1}
$C^{SA} = (\frac{\partial \sigma}{\partial T})_{SA}$	Unloading stress-temperature coefficient	6.1 MPa K^{-1}
T_0	Reference temperature	243 K
ε_L	Maximum transformation strain	4.6%
π	Maximum volumetric transformation strain	0.0%

2.4.2 SMA spring pseudoelastic test

SMA helical springs are widely employed in passive control for seismic applications, thank to the damping capabilities due to their hysterical behavior [58]. The FEA analysis consists on a traction pseudoelastic test

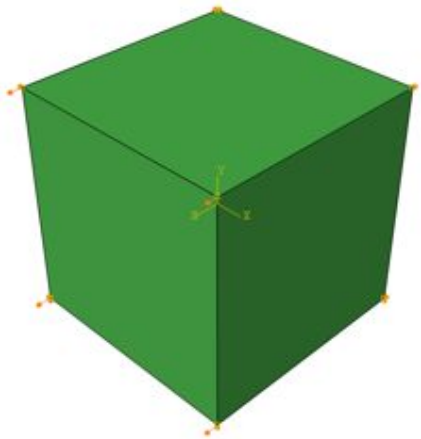

Figure 2.10 *Pseudoelastic cube test FEA model.*

performed on a helical spring portion. The model is discretized with 6312 C3D8 elements (Fig. 2.12). An axial displacement is applied to one end of the helical spring while the other end is clamped. The displacement is increased from zero to its maximum value and unloaded back to zero. Stress-strain diagram for both models are shown in Fig.2.13. Stress is evaluated at a reference point in the proximal end while the engineering strain is evaluated as $(l - l_0)/l_0$, where $l - l_0$ is the spring elongation and l_0 is the spring initial length. The two models provide comparable behaviors, both in terms of stress-strain curves and Von Mises stress distribution (Fig. 2.14). Moreover, we report in Table 5.4 the model comparison with respect to simulation time and the requirement of convergence enhancement. Convergence enhancement is defined as a set of customized options for the FEA solver, including line-search algorithm, tolerances modifications etc. . The description of such tools is detailed in Appendix A.

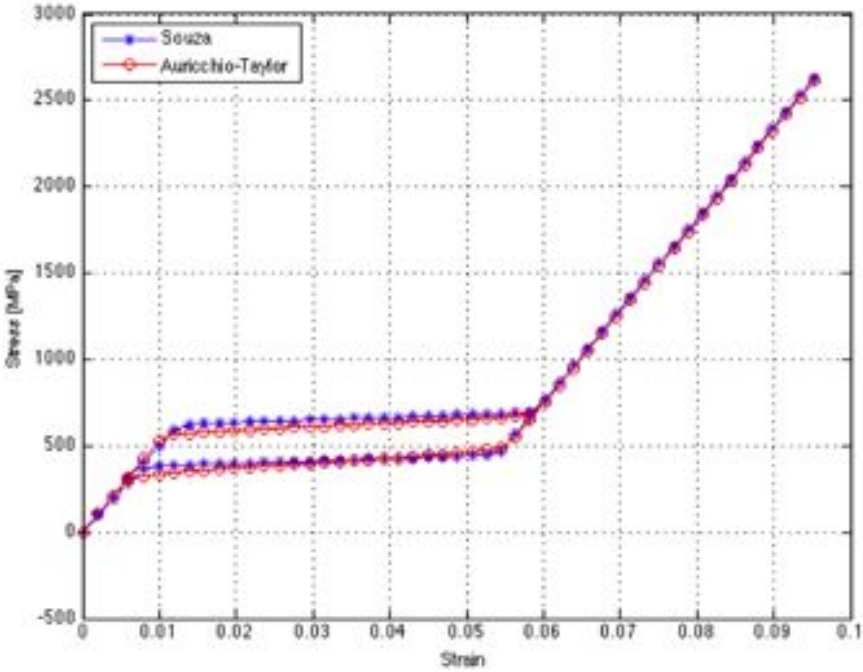

Figure 2.11 *Pseudoelastic cube test: stress-strain diagram.*

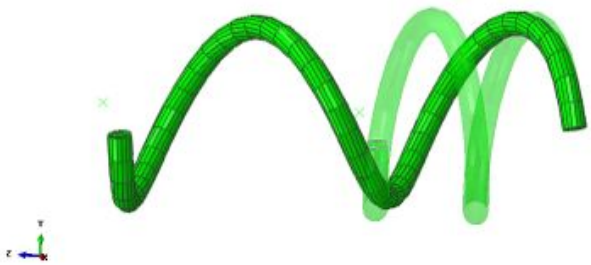

Figure 2.12 *Spring pseudoelasticity test: initial and deformed configurations.*

Table 2.3 *Pseudoelastic spring test resume*

Model	Convergence Enhancement	Min Time Step [s] Step [s]	Convergence	Total time [s]
Souza	NO	10^{-7}	YES	1458.5
Auricchio-Taylor	YES	10^{-7}	YES	604.5

2.4.3 Stent crushing test

Stent manufacturing is the main application of SMA materials in medical applications. Therefore, we now investigate the behavior of a pseudo-elastic stent ring, which represents an example study for bending issues. This test involves geometric nonlinearity with addition of a complex contact interaction. The FEA model includes the following parts:

- Stent model: the FEA model resembles a stent employed in the clinical practice, i.e., ACCULINK (Abbott, Illinois, USA) carotid stent. The planar design is drawn with a CAD software and the tridimensional surface is imported in Abaqus as a solid part. The mesh is cre-

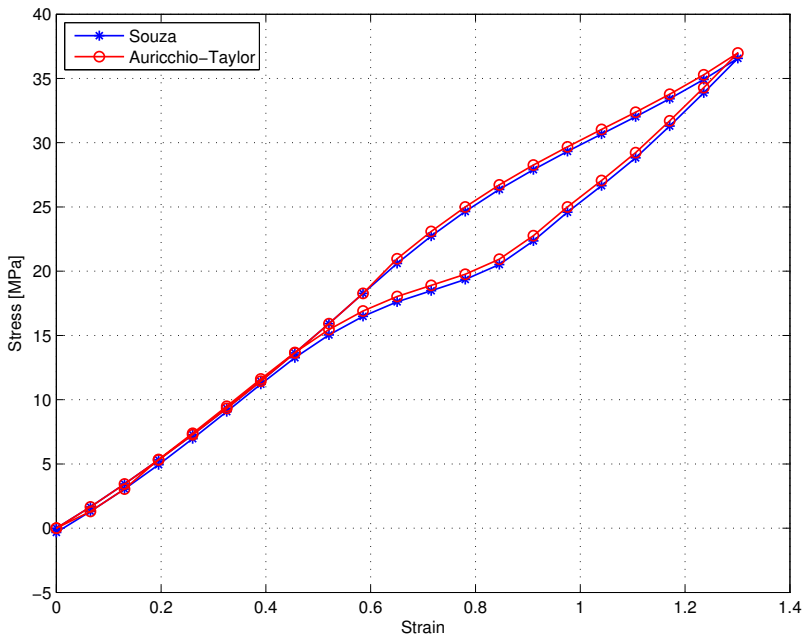

Figure 2.13 *Spring pseudoelasticity test: stress-strain diagram.*

ated using a compartimental approach (the main structure is decomposed in many simpler regions, easier to be meshed). Subsequently, the nodal mesh coordinates are sent to an in-house Matlab script code to roll the planar mesh and to obtain the final model. For this simulation, 40068 linear hexahedral C3D8 elements are employed;

- Plates: the compression plates model is used to simulate the crushing procedure and the subsequent strain recovery step. The plates are modeled as rigid bodies meshed with 80 three-dimensional, 4-node

surface elements with reduced integration (R3D4).

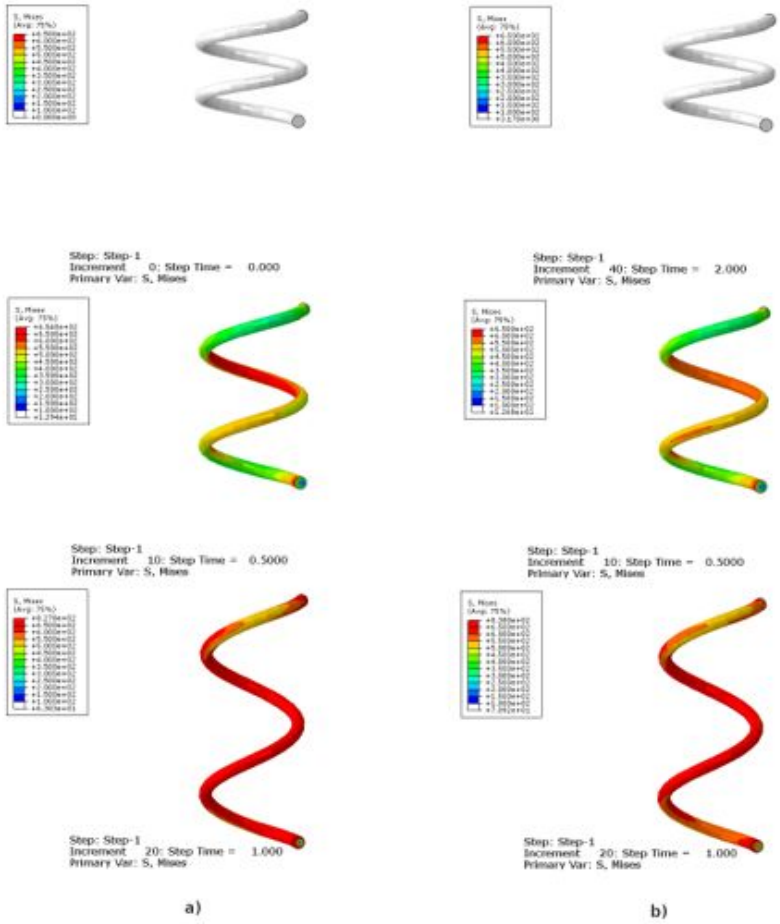

Figure 2.14 *Spring pseudoelastic test: contour plot comparison between Souza (a) and Auricchio-Taylor (b) model.*

This FEA simulation is structured with two steps at constant temperature ($T > A_f$). In the first one the stent is compressed by the relative motion between the two plates with a 70% reduction of the stent diameter (Fig. 2.15-a). Subsequently, the compression plates return in the original position allowing the strain recovery (Fig. 2.15-b). Concerning to the contact modeling, tangential and normal behaviors are modeled frictionless and with a linear penalty method (stiffness = 0.001), respectively. The simulation

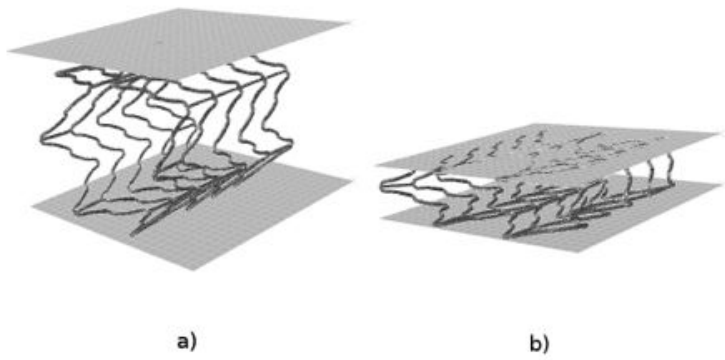

Figure 2.15 *Crushing test of Nitinol stent: a) initial configuration; b) crushed configuration.*

force-displacement diagrams are shown in Fig. 2.16. Moreover, the Von Mises stress distribution of the two models show good agreement (Fig. 2.4.3). Again, we report in Table 5.5 the model comparison with respect to elapsed simulation time and the requirement of convergence enhancement.

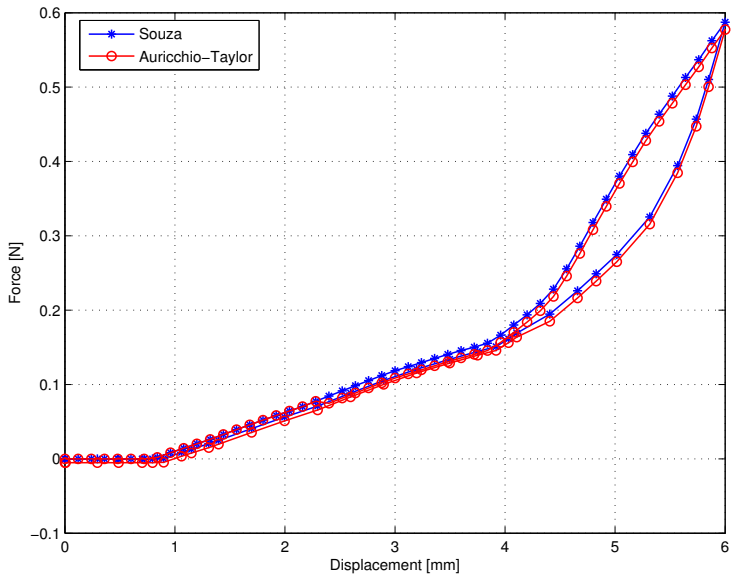

Figure 2.16 *Crushing test of Nitinol stent: force-displacement diagram.*

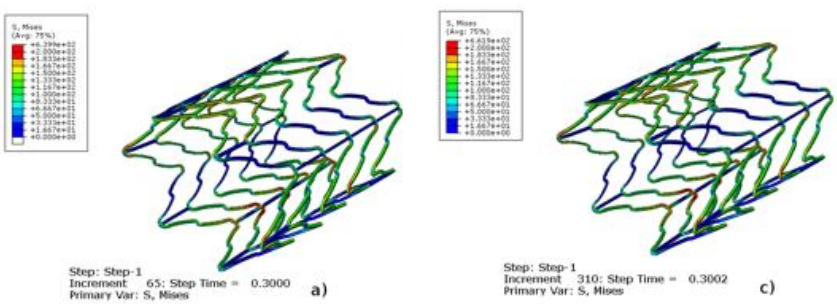

Figure 2.17 *Crushing test of NiTiNOL stent: contour plot comparison between Souza (a), and Auricchio-Taylor (c) UMAT (step 1 step time=0.3).*

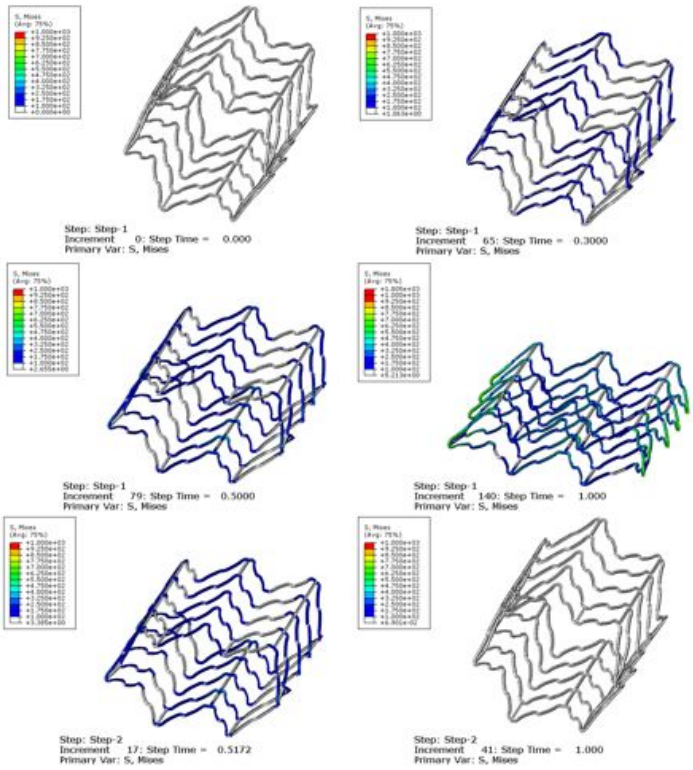

Figure 2.18 *Von Mises stress distribution in different analysis steps.*

Table 2.4 *Stent crush test resume*

Model	Convergence Enhancement	Min Time Step [s] Step [s]	Convergence	Total time [s]
Souza	NO	10^{-7}	YES	5633
Auricchio-Taylor	YES	10^{-7}	YES	2312

2.4.4 SMA spring hysteresis test

Hysteretical behavior is the functioning principle for a wide variety of devices. Among them, SMA spring actuators cover a wide application field, from automotive to robotics. For this reason, numerical simulations are valuable tools to provide useful features information and behavior prediction, in order to design novel devices. For this example the spring is clamped at distal end and loaded by an axial force (9.81 N) at the proximal one during the first step. Subsequently, keeping constant the load, the spring is subjected to temperature cycle, exhibiting both stretching and shape actuation (Fig. 2.19).

This test involves different complex phenomena, such as geometric non linearity and thermo-mechanical interaction. The strain-temperature diagram is shown in Fig. 2.21. Unexpectedly, only Souza model reached convergence, while Auricchio-Taylor model shows off a larger saturation value without reaching convergence, even resorting to convergence enhancement

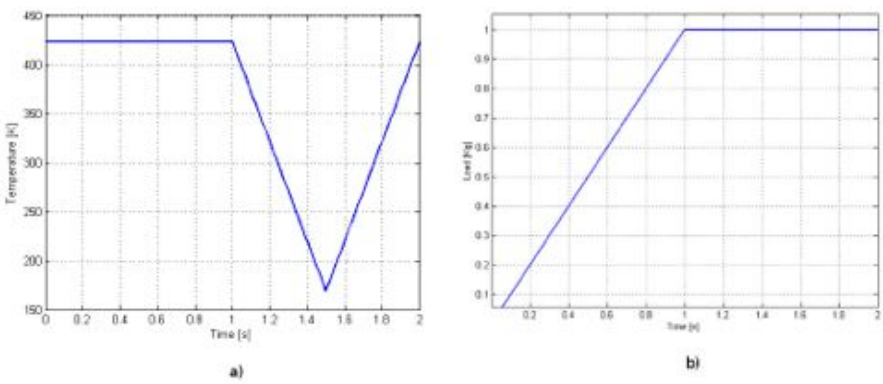

Figure 2.19 *Spring actuator: temperature (a) and load (b) profile.*

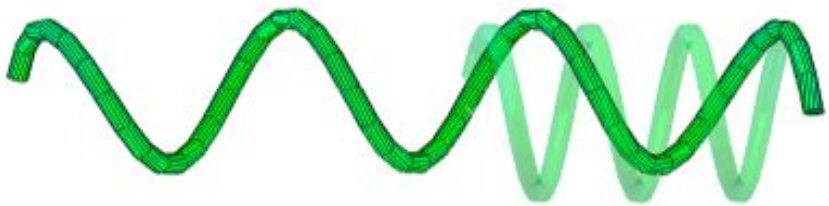

Figure 2.20 *Spring actuator: initial and deformed configuration.*

tools. We remark that the low saturation values obtained by the Souza model do not represent the experimental behavior [59] (Fig. 2.22-b). In particular, the Souza model structure does not allow to reproduce SMA behavior for work conditions in which the material is considered linear elastic (Fig. 2.22-a stress region 1) of where the model is particularly sensitive to numerical implementation (Fig. 2.22-a stress region 2). This limitation can be overcome introducing the linear dependance on working temperature by the elastic radius parameter (Fig. 2.22-b label Mod. SA). Concerning to Auricchio-Taylor, the poor convergence behavior during simulations characterized by constant loads and thermal cycles has been already noticed in the literature [60]. However, to our knowledge this particular issue has not been investigated yet.

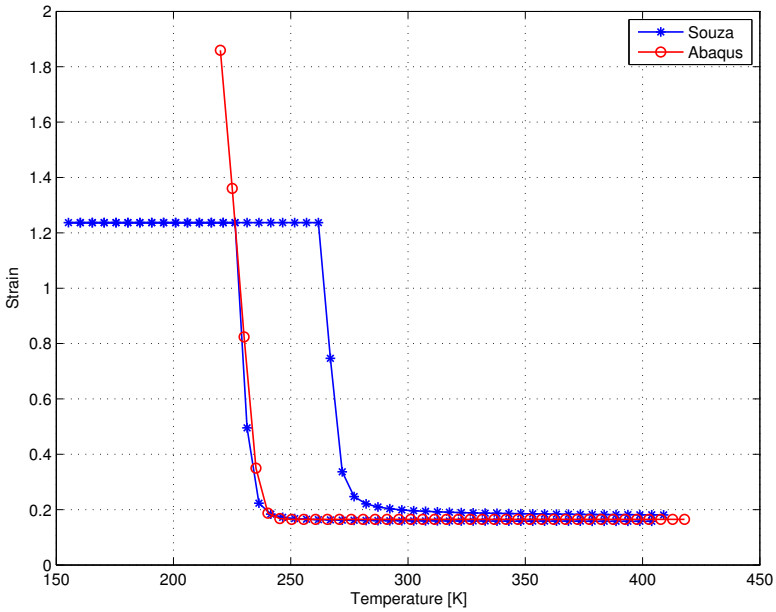

Figure 2.21 *Spring actuator: strain-temperature diagram.*

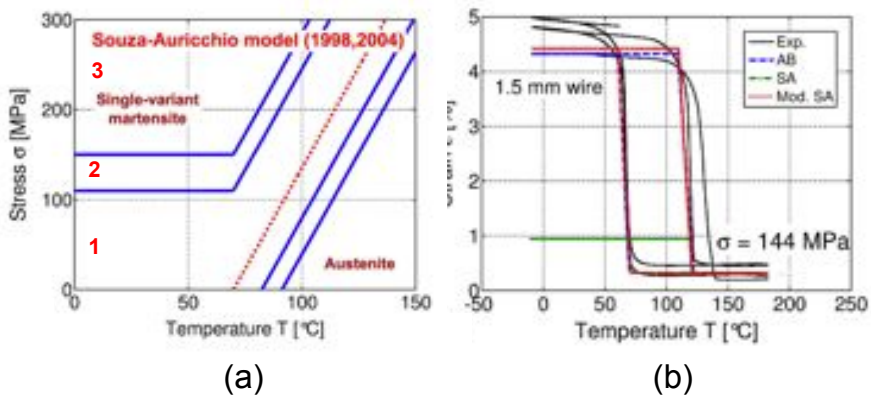

(a) (b)

Figure 2.22 *Souza model low saturation issue: (a) phase diagram highlighting the different stress regions; (b) model comparison with respect to experimental data.*

2.5 Summary

The present chapter discusses the capabilities of two different SMA models with a set of FEA involving different material behaviors and model complexity. The results show similar results both for simple benchmark tests and for more complex simulations. The use of Auricchio-Taylor model, given its formulation, is appropriate only to reproduce pseudoelastic simulations while Souza model is suited also to reproduce the one-way shape memory effect. Both models, unexpectedly fail to accurately reproduce the analysis involving thermal hysteresis (Section 2.4.4). Concerning to computational efficiency, it is important to note that, even if Souza model has higher computational times than Auricchio-Taylor model (see Tables 5.4 and 5.5), it does not require any convergence enhancement for all the considered simulations. This is due to a sub stepping code portion, embedded in the subroutine, able to improve convergence during phase transition.

This peculiar feature allows the Souza model to reach convergence in all the investigated cases but at the same time induces a significant increase of the analysis computational cost.

Chapter 3

Vessel scaffolding evaluation for carotid artery stents: a FEA-based approach

MOVING from the constitutive models presented in the previous chapter, we now adopt the combination of Auricchio-Taylor model and traditional displacement-based FEA to evaluate one of the most important features for carotid artery stents, i.e., vessel scaffolding.

3.1 Problem definition

As introduced in Chapter 1, while during CEA the atherosclerotic plaque is removed, with CAS the plaque remains contained between the stent and the vessel wall, moving consequently the physicians' concerns from the intra-procedural to the post-procedural stage. In fact, stent struts compress the dilated plaque material, which should not protrude into the lumen to guarantee that no debris is dislodged after the procedure.
Starting from this basic concept, it is clear that the procedure outcomes are linked to stent design, which is usually resulting as a trade-off between

several biomechanical features. Among the others, the vessel scaffolding, i.e., the stent capability to support the vessel wall after stenting, represents a crucial issue. Vessel scaffolding is usually determined by the free cell area, which is dependent upon the number and arrangement of bridge connectors. In closed-cell stents, adjacent ring segments are connected at every possible junction, while in open-cell stents, not all of the junction points are interconnected. Thus, a closed-cell stent design has a smaller cell area than its corresponding open-cell counterpart. The relation between stent design and procedure outcomes is still matter of an intense clinical debate [61, 62, 63, 64, 65], recently extensively discussed and reviewed by Hart and colleagues [66].

The evaluation of vessel scaffolding is not easily standardized or measured; typically, the cell area of a given stent is measured in its free-expanded configuration [15]. Although this measure is appropriate to compare different designs, it is challenging to be measured in vivo and does not take into account the actual configuration of a stent implanted in a tortuous carotid bifurcation. This limitation can be overcome exploiting realistic simulations of CAS [20].

Within this framework, the present study aims at assessing the cell area of four different stent designs deployed in a realistic carotid artery model through patient-specific FEA.

3.2 Materials and Methods

In this section, we start from a previous study from our group [20], addressing the validation of CAS simulation with respect to a real stent deployed in a patient-specific silicon mock artery. We then combine the methodologies proposed in that paper with a procedure to measure the cell area in order

to accomplish the goal of the present study.

3.2.1 Vessel model

The patient-specific vessel model considered in this study is reflecting the geometry of a silicon mock artery, derived from DICOM images of a neck-head Computed Tomography Angiography (CTA) performed on an 83 year-old male patient at IRCCS San Matteo in Pavia, Italy. The common carotid artery (CCA) has a mean diameter of 7 mm while the internal carotid artery (ICA) has a mean diameter of 5.2 mm; a mild stenosis (24% based on NASCET method) is present slightly above the bifurcation.
Given the variable wall thickness of the silicon model, the related finite element model is derived by an high-resolution micro-CT scan of the sole mock artery, segmented by Mimics v.13 (Materialise, Leuven, Belgium). For the sake of simplicity, only a portion with a length of 42 mm, meshed by 73322 10-node modified tetrahedron with hourglass control - C3D10M - elements and 134092 nodes, of the whole model (see figure 3.1) is considered for the simulation performed by Abaqus/Explicit v. 6.10 (Dassault Systémes, Providence, RI, USA), as discussed in subsection 3.2.3.

The mechanical response of silicon is reproduced assuming an hyperelastic material model, defined by a second order polynomial strain energy potential U defined as:

$$U = \sum_{i+j=1}^{2} C_{ij}(\bar{I}_1 - 3)^i(\bar{I}_2 - 3)^j + \sum_{i=1}^{2} \frac{1}{D_i}(J^{el} - 1)^{2i} \tag{3.2.1}$$

where C_{ij} and D_i are material parameters; $\bar{I}_1$ and $\bar{I}_2$ are respectively the first and second deviatoric strain invariants. The material model calibration is performed on the stress-strain data derived from a tensile test on a silicon

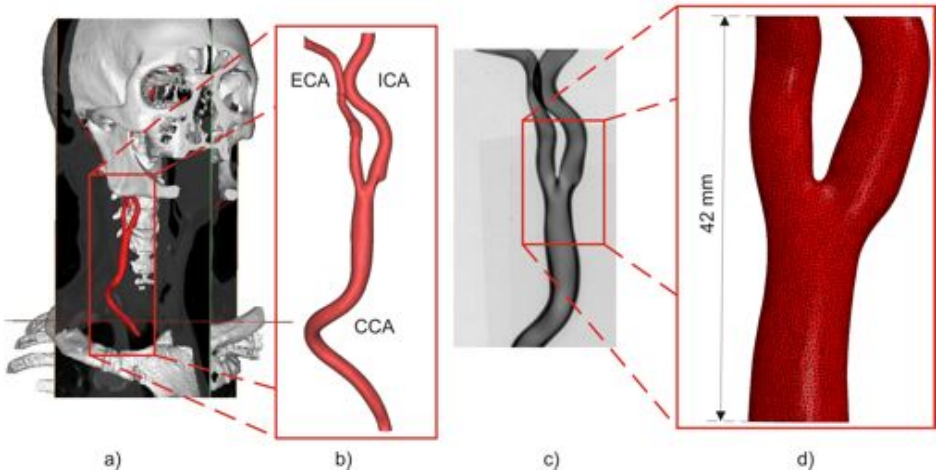

Figure 3.1 *Elaboration of Computed Tomography Angiography (CTA) images: whole 3D reconstruction of neck-head district highlighting the region of interest (a); surface describing the CA lumen used to create the silicon artery (b); radiography of the silicon artery highlighting the non-uniform wall thickness (c); tetrahedral mesh adopted in the simulations (d).*

sample and results in the following non-null coefficients: $C_{10} = -2.40301$ MPa; $C_{01} = 3.02354$ MPa; $C_{20} = 0.456287$ MPa; $C_{11} = -1.72892$ MPa; $C_{02} = 2.73598$ MPa.

3.2.2 Stent finite element model

Four different self-expanding NiTiNOL carotid stent designs are considered. They resemble four commercially available stents used in the clinical practice. In the following they will be referred to as model A (ACCULINK - Abbott, Illinois, USA), model B (Bard ViVEXX Carotid Stent - C. R. Bard Angiomed GmbH & Co., Germany), model C (XACT - Abbott, Illinois, USA) and model D (CRISTALLO Ideale - Invatec/Medtronic, Roncadelle (BS), Italy), respectively. Given the comparative nature of the study, for all designs we considered the straight configuration having a 9 mm reference diameter and 30 mm length. Since no data are available from the manufacturer, the main geometrical features of such devices are derived from high-resolution micro-CT scans of the stent in the delivery system (see figure 3.2-a). As discussed in previous studies [20, 67], the stent model to be embedded in CAS simulation is generated through the following steps:

- a planar CAD geometry (see figure 3.2-b), corresponding to the unfolding of stent crimped in the delivery catheter, is generated by Rhinoceros v. 4.0 SR8 (McNeel and Associated, Seattle, WA, USA) and subsequently imported to Abaqus/CAE v. 6.10 (Dassault SystËmes, Providence, RI, USA) where the mesh is generated;

- through appropriate geometrical transformations performed by an in-house code in Matlab (The Mathworks Inc., Natick, MA, USA), the planar mesh is *rolled* leading to the final crimped stent (i.e., laser-cut configuration) as depicted in figure 3.2-c;

- simulating the shape-setting process through FEA (solver: Abaqus/Explicit v. 6.10 - Dassault SystËmes, Providence, RI, USA), the crimped configuration is transformed into the free-expanded configuration (see figure 3.2-d).

The mesh details about the considered stent FE models are reported in table 3.7, where also the numbers of the considered cells for the area measurement, with respect to three stent segments (i.e., proximal, bifurcation and distal), are reported. The stent models in free-expanded configurations are instead depicted in figure 3.3.

3.2.3 Stent deployment simulation

To investigate the interaction between the stent and the patient-specific CA model, we perform a two-step simulation procedure [20, 68]. In the first step the diameter of the stent is decreased simulating the loading phase of the stent into the delivery system. Subsequently, the stent inside the delivery sheath is placed into the target lesion and there the retractable sheath is removed allowing the stent/vessel interaction and thus mimicking stent placement. We use the pre-stenting vessel centerline for stent positioning and the stent deformation is imposed by a profile change of the retractable sheath, through appropriate displacement boundary conditions on its nodes. These boundary conditions are determined as the difference between the starting and final sheath shape. The simulation is performed using Abaqus/Explicit v. 6.10 as finite element solver, since the numerical analysis is characterised by non-linearity due to the material properties, large deformations and complex contact problems. The general contact algorithm is used to handle the interactions between all model components; in particular, a frictionless contact between the stent and delivery sheath,

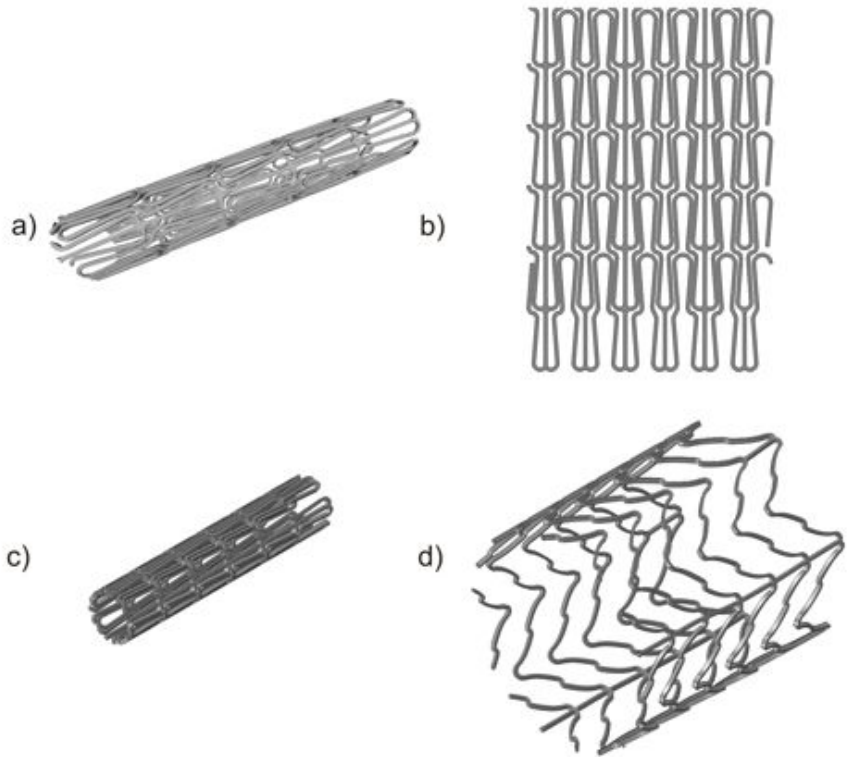

Figure 3.2 *Stent mesh generation: detail of a high resolution micro-CT performed on a real stent within the delivery system (a); planar CAD geometry resembling the stent design pattern (b); stent mesh in crimped configuration (c); stent mesh in free-expanded configuration (d).*

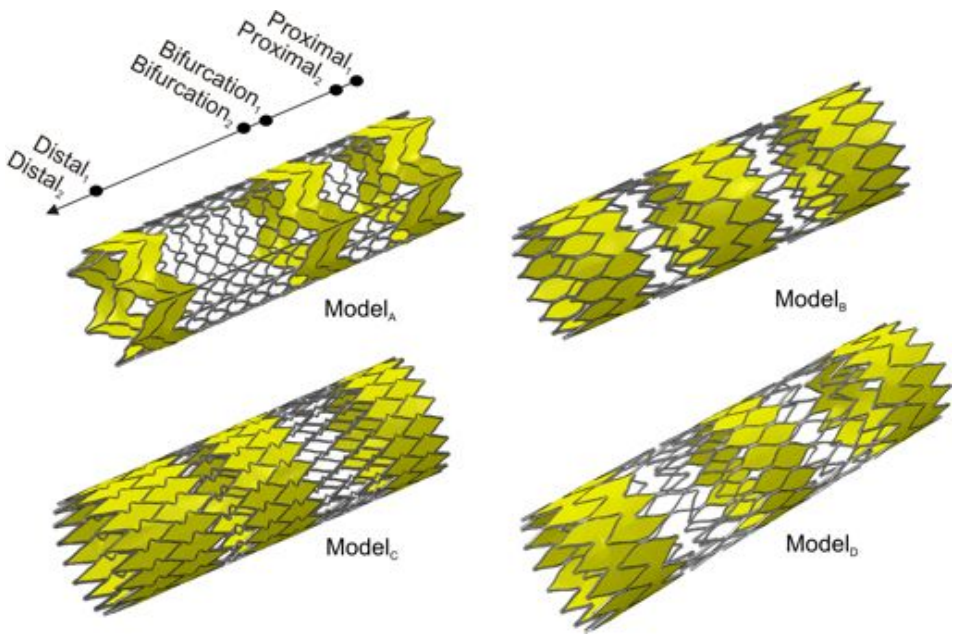

Figure 3.3 *Considered stent designs in free-expanded configuration. The cells considered for area computation are depicted in yellow.*

and a friction coefficient of 0.2 between the stent and the vessel inner surface is assumed.
The superelastic behavior of Nitinol is modeled using the Auricchio-Taylor model described in Chapter 2, by means of the Abaqus built in material subroutine [69] and the related constitutive parameters are obtained from the literature [70]; we consider such material properties identical for all stents and we assume the density to be 6.7 g/cm^3.

3.2.4 Measuring the stent cell area

We measure the cell area of a 3D surface having the cell contour as a boundary. To create such a surface it is necessary to: i) identify the cell boundary nodes; ii) sort these nodes in an appropriate manner to define a spline; iii) use the spline to create the target surface. To speed up such a process, we integrate Matlab and Rhinoceros in a workflow defined by the following steps:

1. *Node set identification of each cell boundary from the planar mesh*: since the node label does not change along the geometrical transformation described in section 3.2.2, we move from the planar mesh to clearly identify cell boundary nodes and to easily associate the related nodal labels (see figure 3.4-a/b).

2. *Delaunay triangulation of each node set*: the basic idea is to use the triangulation (see figure 3.4-c) to detect the outer edges and the related nodes, using thus the edge connectivity to drive the nodal sorting. The procedure is improved by the introduction of user-defined *dummy* nodes in order to have less distorted triangle elements inside the cell, improving the efficiency of the next step.

3. *Detection of outer edges and node sorting*: as depicted in figure 3.4-c, the mesh obtained in the previous step does not match the cell boundaries. To overcome such a problem we exploit the approach proposed by Cremonesi et al. [71], taking advantage of a distortion criterion to remove the unwanted triangles. In particular, for each triangle of the mesh, the shape factor is defined as $\alpha_e = \frac{R_e}{h} \geq \frac{1}{\sqrt{3}}$, where R_e is the radius of the circumcircle of the e-th triangle and h the minimal distance between two nodes in the element. This factor represents an index for element distortion and can be used, after the setting of a proper threshold, to remove the unwanted triangles without any modification of the original Delaunay triangulation. For this work, in order to create an algorithm able to change its requirement with the different cell configurations, we set the shape threshold to 1.5 $\overline{\alpha_e}$, where $\overline{\alpha_e}$ is the α_e average. After the undesired cells removal (see figure 3.4-d), the algorithm identifies the cell borders (see figure 3.4-e) and sorts the nodal labels in order to make them suitable for the next step. At this stage the nodal labels can be associated with the deformed nodal coordinates in order to obtain the deformed cell.

4. *Creation of a 3D surface for each cell and area measuring*: through a script in Rhinoceros, we firstly define a 3rd order polynomial curve passing through the cell boundary nodes and we finally create the related patch surface, as illustrated in figure 3.4-f. In this way, each cell area can be automatically measured and exported in a tabular format.

In this study, we compute the cell area as a scaffolding measure since it resembles in a more accurate manner the current configuration of the cell with respect other comparators such as the largest fitted-in circle (LCF),

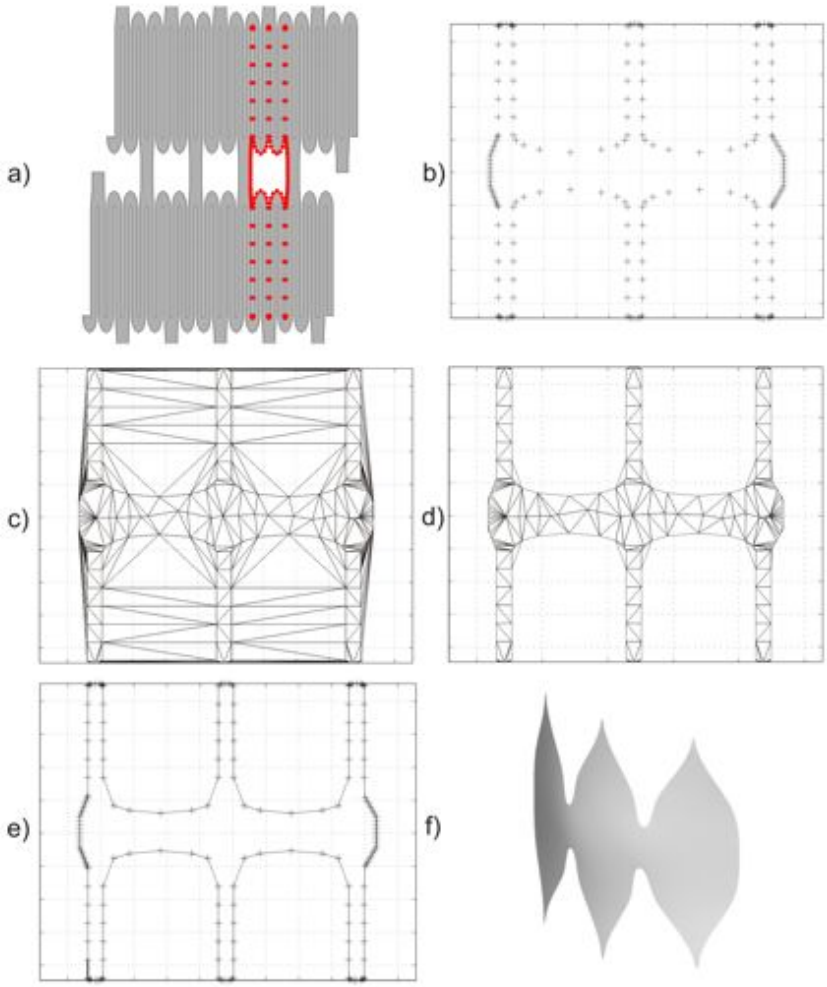

Figure 3.4 *Cell surface definition: Node identification of cell boundary nodes (a-b); Delaunay triangulation of each node set (c); Delaunay triangulation after the application of distortion criterion (d); detection of outer edges (e); creation of 3D cell surface (f).*

which would represent somehow the maximum size of a plaque particle potentially protruding through the stent struts. With respect to this issue, Müller-Hülsbeck et al. [15] report a LCF of 1.18 mm for both ACCULINK (open-cell) and XACT (closed-cell) and 1.2 mm CRISTALLO Ideale (closed-cell) in the corresponding stent middle portion, while the cell area is 15.10 mm^2 for ACCULINK, 3.55 mm^2 for XACT and 3.30 mm^2 for CRISTALLO. From these data, we can observe that LFC does not catch the difference between the various stent designs which is instead particularly evident through the cell area.

3.3 Results

In order to evaluate the suitability of our approach, we have firstly compared the cell areas computed in free-expanded configuration by our numerical models with respect to the data available in the literature. Given the lack of studies dealing with this topic, for such a comparison we can only refer to the work of Müller-Hülsbeck et al. [15]. In particular, for our purpose we consider the measurements reported about i) 7-10X30mm[1] ACCULINK (Abbott, Illinois, USA), ii) 8-10X30mm XACT (Abbott, Illinois, USA) and iii) 7-10X30mm CRISTALLO Ideale (Invatec/Medtronic, Roncadelle (BS), Italy). Since the considered stents are tapered, we appropriately modify Model A, Model C and Model D during the shape-setting step of stent mesh creation. As highlighted by table 3.7, our results are acceptably matching the experimental data. We remark that in table 3.7 the data from Müller-Hülsbeck et al. [15] of distal and proximal segments have been swapped, since we believe that a typo is present in that paper. Such a consideration is reasonable if we assume that, given the same cell

[1] distal-proximal diameter X length

shape, the smaller is the diameter of the related segment, the smaller is the cell area; consequently, in a tapered stent, the distal segment diameter is smaller than the proximal one and thus the corresponding cell area. With respect to Model D, we would also underline that our results match well with the data presented by Cremonesi et al. [72], who are in fact reporting an average cell area of 15.17 mm^2 for the proximal segment, 3.24 mm^2 for the middle segment and 11.78 mm^2 for the distal one.
The post-stenting configurations obtained by the deployment simulations with respect to the four considered models are reported in figure 3.5. Given the free-expanded and deployed configuration, for each stent it is possible to compute the cell area with respect to four stent segments as reported in table 3.7 and figure 3.6.
Both Model A and Model B are generally classified as *open-cell* but, at distal and proximal ends, the cells are partially closed in Model A and fully closed in Model B, to enhance the stent stability during the release; this feature is not present on Model D. Considering the free-expanded configuration, this aspect leads to a variable cell size in the distal and proximal segment as highlighted in figure 3.6, while the cell area is uniform in the bifurcation segment. After the deployment, if we consider the cell sets ranging from $Proximal_2$ to $Distal_1$, it is possible to notice that the cell area is decreasing following the vessel tapering pointing up the dependence of the cell size from the target vessel caliber. For Model B, it is worth to notice that the percentage reduction of different cell types is comparable in the proximal and distal segments (see table 3.7).
Model C, which is a fully closed-cell design, shows a peculiar behavior. In fact it has a cell shape varying along the length, leading to a progressive cell size increase, which is evident in free-expanded configuration (see figure 3.6-c). This feature compensates the cell area reduction due to apposition,

providing thus a uniform cell size after the deployment.
Model D resembles the features of Cristallo Ideale Carotid Stent, a nitinol self-expanding stent, which has a hybrid design consisting of three segments: a closed cell midsection with open cell portions at both edges, which are intended to provide adequate scaffolding to the carotid plaque while assuring high flexibility and vessel wall adaptability. Such a variability in the design is reflected by the change of the cell area along the stent length, showing a smaller cell area in the bifurcation segment.
Analyzing the standard deviation values, it is possible to notice that the vessel curvature induces a non uniform distribution of the cell area in circumferential direction for Model A and B especially in the bifurcation segment. This effect is particularly evident for Model A (see figure 3.5-a) where the bending due to the angulated CA bifurcation, causes a mis-alignment and protrusion of the stent struts on the open surface, so-called fish-scaling effect.
The indications provided by the free-expanded configuration (see figure 3.6-e) are qualitatively maintained after the deployment (see figure 3.6-bottom); in fact, Model A has the larger cell areas while Model C and Model D have the smaller ones at the bifurcation level. It is necessary to underline that in the segment $Distal_2$ the cell area odf Model D is higher than the other stent models but, by a clinical point of view, this aspect is negligible since often the middle part of the stent is in charge to cover the plaque.

3.4 Discussion

Carotid angioplasty and stenting is usually inducing the disruption of atheromatous plaque obstructing the lumen. Consequently, the physicians' con-

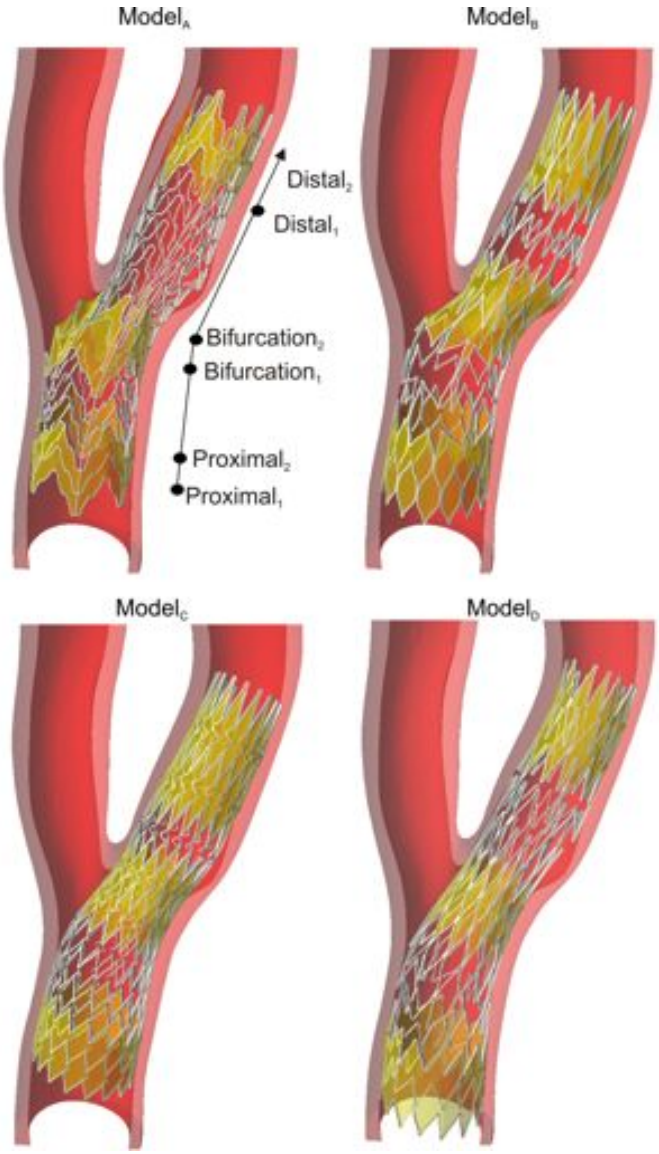

Figure 3.5 *Considered stent designs after the deployment simulation. The cells considered for area computation are depicted in yellow.*

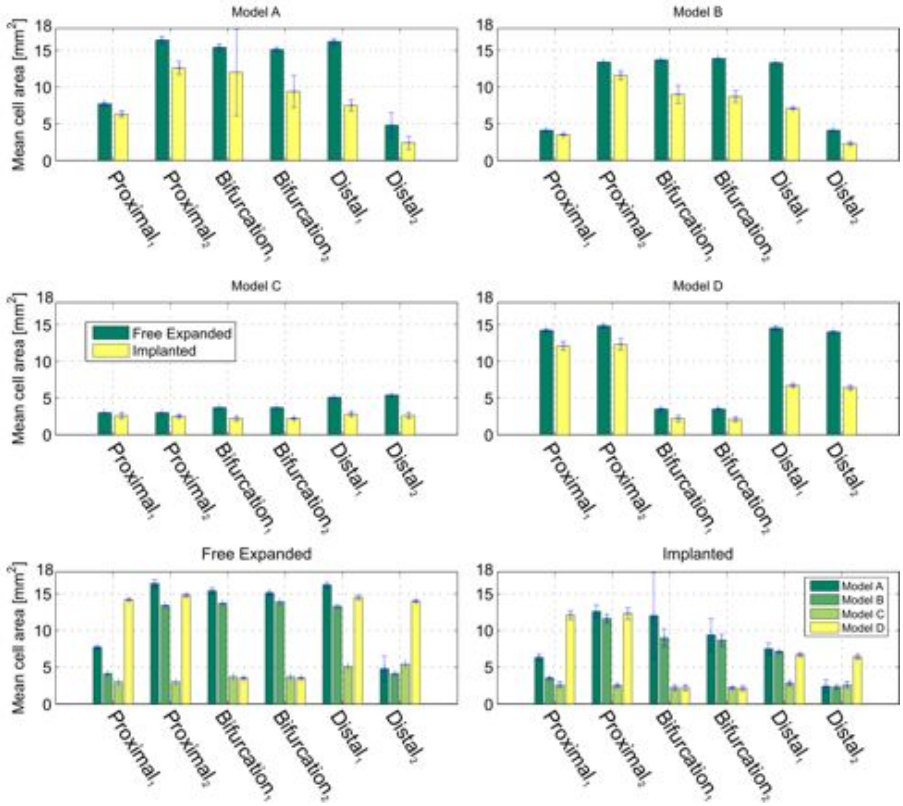

Figure 3.6 *Bar graph of the mean cell area: free expanded VS implanted for each stent model (top and middle); comparison between the stent models in free-expanded configuration (bottom-left) and implanted (bottom-right).*

cerns are now turned to stent capability to limit plaque protrusion, i.e., vessel scaffolding, to avoid that some debris is dislodged after the procedure.

There is an intense debate [61, 62, 63, 64, 65, 66, 71] about the impact of stent design on post-procedural events. Hart et al. (2006) [65] by a retrospective study suggest that patients treated with closed-cell stents have a lower risk to experience post-procedure adverse events, when compared to patients treated with open-cell design; they formulate the hypothesis that, since transient ischemic attack is related to small particles passing through the stent mesh, closed-cell stents have a superior capability to scaffold the emboligenic plaque, given to their smaller free cell area.

Bosiers et al. (2007) [64] support the conclusions from Hart et al. [65], showing that post-procedural complication rates are higher for the open-cell stent types, especially in symptomatic patients; moreover, such complications increase with larger free cell area. Consequently, Bosiers et al. [73] sustain that the smaller is the free cell area, the better is the stent capability to keep plaque material behind the struts. Although the characteristics of the plaque and its stability should be considered for an appropriate patient selection [64]

Schillinger et al. (2008) [63] do not confirm the indications previously illustrated; in fact, their retrospective analysis has not indicated any superiority of a specific carotid stent cell design with respect to neurological complications, stroke, and mortality risk.

This debate has been further enriched by other contributions [61, 62, 66] highlighting the need of other dedicated studies.

Given such considerations, it is possible to state that stent scaffolding is a clinically-relevant topic; unfortunately, the clinical debate has not an *engineering* counterpart. In particular, really few studies are addressing the

quantification of vessel scaffolding of a given stent design. Müller-Hülsbeck et al. [15] performed an in-vitro study measuring the cell area of several commercially available stents in free-expanded configuration. They performed the measurements by the software of their optical microscope. Despite this approach is appropriate for comparative purposes, it neglects the current configuration of the stent implanted in a tortuous CA bifurcation and the related cell configuration change. In our previous study [20], we have considered only one stent model in two design configurations, using the interstrut angle as a measure of scaffolding. Consequently, it is clear that there is still room for further investigations, hence we measure the cell area of four different stent designs deployed in a realistic carotid artery model through patient-specific finite element analysis (FEA).

Our results confirm the basic idea that, given a cell shape, the cell area depends on the size of the vessel segment where the stent is deployed. Even if this result is not surprising, it is important to underline that there is a dramatic reduction of the cell size (up to -54.7%) after the deployment. Despite the indications derived from the free-expanded configuration are useful and appropriate for comparative purposes, the conclusions withdrawn by this approach should be carefully considered; in fact they neglect the variance of the cell size along the stent length, which sometimes mitigates the difference between two stent designs observed in the free-expanded state. Following these thoughts, we agree with Siewiorek et al. [74], who sustain that analyses based on binary classification, such as open- vs closed-cell, or on a single variable may be misleading given the complexity of the approached problem.

Our results also confirm the qualitative observation reported by Wholey and Finol [75], who underline the role of vessel anatomy for vessel scaffolding; in fact, when cells open on the concave surface of an angulated CA

bifurcation, they could prolapse showing the so-called fish scaling effect. This issue could induce some drawbacks and is affecting the scaffolding uniformity at the bifurcation segment (see figure 3.5 and figure 3.6-d).

3.5 Limitations

The main limitations of the present study are related to the following items: i) only one specific vascular anatomy is considered; ii) the degree of stenosis is low (i.e., 24%). The consideration of more severe stenosis demands for the assessment of the atherosclerotic plaque morphology and its mechanical response, which is one of the most challenging within the framework of stenting simulations. In particular, the mechanisms driving the plaque rupture during pre-stenting angioplasty should be accounted and modelled; in fact, during real CAS procedure approaching severe stenosis, the vessel patency is primarily restored with an angioplastic procedure and after that, the stent is deployed in order to avoid elastic recoil leading to early re-occlusion.

Up to now, the majority of the numerical studies addressing structural analysis of stent in atherosclerotic vessel does not consider severe stenosis [68, 76, 77] and simplifies the problem from both geometrical and constitutive point of view [78, 79]. Despite an excellent study toward realistic investigation of stenting in highly stenotic (iliac) artery was already provided by Holzapfel and colleagues in 2005 [80], the inclusion of micro-damage and damage mechanism, occurring in the arterial wall due to vascular injury during angioplasty and stent deployment, is still an open point.

Given such considerations and the comparative nature of the present study, we believe that the consideration of a mild stenosis is acceptable. However, future consideration of more severe degrees of stenosis would strengthen the

relation between the obtained results and the clinical practice. Moreover, it is necessary to highlight that in the present study we do not consider the impact of plaque morphology and stability on the vessel scaffolding, since we focus mainly on its relationship with the stent design per se. A low/mild stenosis can be more dangerous than a severe one if the plaque is vulnerable; this issue is in fact related to post-stenting plaque prolapse and is a matter of concern during the procedure planning and for the patient eligibility [81]. Nevertheless, such a simplification is consistent with the experimentally-validated simulation presented in [20], which has shown the ability to predict the deformed configuration of a real stent deployed in a silicon mock artery.

3.6 Summary

In the present study we measure the cell area of three different stent designs deployed in a realistic carotid artery model through patient-specific finite element analysis (FEA) with the aim to consider the actual configuration of the stent within the vessel. The results suggest that after the deployment the cell area change along the stent length and the related reduction with respect to the free-expanded configuration are function of the vessel tapering. Nevertheless, for comparative purposes, the conclusions withdrawn from the free-expanded configuration appear to be qualitatively acceptable, but they should be carefully handled since they do not take into account the variability affecting the cell area distribution after the implant. Such a variability seems to be more pronounced in open-cell designs, whose scaffolding uniformity is impaired especially at the bifurcation segment.
Even though the investigation is limited to few stent designs and one vascular anatomy, our study confirms the capability of dedicated simulations

based on computational mechanics methods, such as FEA, to provide useful information about complex stent features as vessel scaffolding. Such predictions could be used to design novel carotid stents or for pre-surgical planning purposes.

3.7 Tables

Model label	A	B	C	
Reference stent	ACCULINK	VIVEXX	XACT	CRISTALLO
Design	Open-cell	Open-cell	Closed-cell	Hybrid
N° cells				
$Proximal_1$	6	15	18	5
$Proximal_2$	3	5	18	5
$Bifurcation_1$	3	5	18	14
$Bifurcation_2$	3	5	18	14
$Distal_1$	3	5	18	5
$Distal_2$	9	15	18	5
N. Elements	90552	78160	74764	30000
N. Nodes	177066	41144	33948	65010

Table 3.1 *Overview of analyzed stents. The hybrid stent has closed-cell design in the mid part and an open-cell design at the ends.*

	ACCULINK 7-10x30mm		XACT 8-10x30mm		Cristallo 7-10x30mm	
Stent segment	Model	Ref.	Model	Ref.		
$Proximal_1$	8.7 ± 0.1		3.3 ± 0.1	3.1	15.8 ± 0.1	13.5
$Proximal_2$	16.3 ± 0.0	16.6	3.2 ± 0.1		16.3 ± 0.2	
$Bifurcation_1$	15.1 ± 0.0	15.1	3.7 ± 0.1	3.55	3.4 ± 0.1	3.3
$Bifurcation_2$	15.5 ± 0.0		3.6 ± 0.1		3.3 ± 0.1	
$Distal_1$	12.7 ± 0.1	13.6	4.8 ± 0.1	4.0	11.7 ± 0.1	12.4
$Distal_2$	3.8 ± 1.2		4.9 ± 0.1		11.1 ± 0.1	

Table 3.2 *Comparison of cell area obtained using our approach with respect to the data reported by Müller-Hülsbeck et al. [15], considered here as a reference. Data are reported as the mean ± standard deviation; mm^2 is the unit measure.*

Model label	Configuration	$Proximal_1$	$Proximal_2$	$Bifurcation_1$	$Bifurcation_2$	$Distal_1$	$Distal_2$
Model A	Free exp.	7.7±0.2	16.4±0.5	15.4±0.4	15.1±0.2	16.2±0.3	4.8±1.7
	Implanted	6.3±0.4	12.6±0.9	12.0±5.9	9.4±2.2	7.5±0.8	2.4±0.9
	Implanted vs Free exp.	-18.2%	-23.1%	-22.2%	-38.1%	-53.4%	-49.1%
Model B	Free exp.	4.1±0.0	13.4±0.0	13.7±0.0	13.9±0.0	13.3±0.0	4.1±0.0
	Implanted	3.5±0.1	11.6±0.6	9.0±1.2	8.7±0.8	7.1±0.1	2.3±0.2
	Implanted vs Free exp.	-13.7%	-13.7%	-34.2%	-37.1%	-46.3%	-44.3%
Model C	Free exp.	3.0±0.0	3.0±0.0	3.7±0.0	3.7±0.0	5.1±0.0	5.4±0.0
	Implanted	2.6±0.4	2.5±0.2	2.2±0.3	2.2±0.1	2.8±0.3	2.6±0.4
	Implanted vs Free exp.	-13.9%	-15.2%	-39.0%	-40.8%	-44.5%	-51.4%
Model D	Free exp.	14.2±0.1	14.8±0.2	3.5±0.1	3.5±0.1	14.5±0.3	14±0.1
	Implanted	12.1±0.6	12.3±0.8	2.2±0.4	2.1±0.3	6.7±0.2	6.4±0.3
	Implanted vs Free exp.	-14.8%	-16.8%	-43.4%	-44.1%	-53.9%	-54.7%

Table 3.3 *Cell area in free-expanded configuration and after the stent deployment. Data are reported as the mean ± standard deviation; mm^2 is the unit measure.*

Chapter 4

NURBS-based Isogeometric Analysis fundamentals

THIS chapter aims at introducing the fundamental concepts of Isogeometric analysis starting from NURBS geometric representation. For the sake of simplicity we initially focus the discussion on curves representation. Subsequently, the extension to surfaces and trivariate solids is described. Such NURBS structures represent the basis for the continuum discretization employed within the IgA framework, which is introduced in the second part of the chapter.

4.1 Geometrical modeling of Curves

There exist different mathematical approaches for the description of curves. Basically it is possible to identify three families:

- Explicit representation: the relation between the coordinates of the curve points are expressed by mean of an equation in the form $y = f(x)$ (see Fig. 4.1-a);

- Implicit representation: the relation between the coordinates of the curve points are expressed by mean of an equation in the form $f(x, y) = 0$ (see Fig. 4.1-b);

- Parametric representation: each coordinate is expressed as an explicit function of an independent parameter u, $\mathbf{C}(u) = (x(u), y(u))$ (see Fig. 4.1-c);

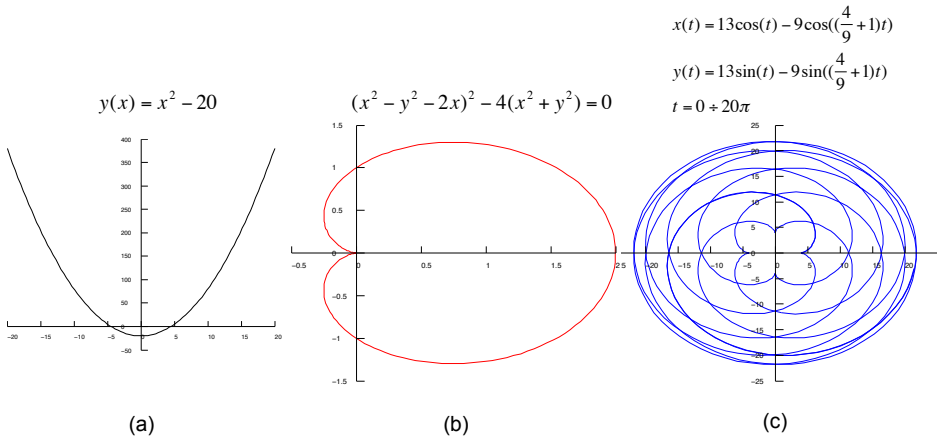

Figure 4.1 *Example of different mathematical descriptions of curves: (a) explicit representation of a quadratic parabola; (b) implicit representation of a cardioid; (c) parametric representation of a epicycloid.*

Each of the geometrical representations presents different advantages and drawbacks, as well as geometrical properties for the resulting curve [82]. The parametric representation is intuitively more suited for a computer implementation and the choice of the coordinate functions becomes crucial to define the properties of a geometric modeling system. A common choice is to use n-th order polynomials as basis functions in order to get the

following form

$$\mathbf{C}(u) = (x(u), y(u)) = \sum_{i=0}^{n} \mathbf{a_i} u^i \qquad with \qquad \mathbf{a_i} = (x_i, y_i). \tag{4.1.1}$$

where u^i are called the basis functions and $\mathbf{a_i}$ the coefficients of the geometrical representation. Several choices for the basis functions are available, e.g., power basis, Bézier curves, rational Bézier curves [82]. Although these basis functions are a powerful tool, they present the following drawbacks:

- the construction of a curve starting from n data coefficients implies a $n+1$-th order curve;
- high degree is necessary to reproduce complex shapes.

These limitations can be overcome with the introduction of B-splines and NURBS.

4.2 NURBS geometric representation

B-splines are the antecedents of NURBS and are still widely employed as geometric representation tool in many CAD softwares. Therefore, this section aims at introducing B-spline curves and their properties, since most of the definitions and properties of B-splines naturally propagate to NURBS. Thereafter, the generalization to B-splines surfaces and solids is presented. At last, the generalization of B-splines to NURBS is described.

4.2.1 B-splines

B-splines are piecewise polynomial geometrical entities widely used in CAD and computer graphics.

A p–th order B-spline curve is constructed by linear combination of B-spline basis functions and, coefficients $\mathbf{B}_i$, defined in $\mathbb{R}^d$ and named control points, as follows:

$$\mathbf{C}(\xi) = \sum_{i=1}^{n} N_{i,p}(\xi)\mathbf{B}_i, \tag{4.2.1}$$

where n is the number of basis functions (and control points). The parameter space of the curve is described by the variable ξ. A knot vector Ξ is defined as a non-decreasing, real-valued vector

$$\mathbf{\Xi} = [\xi_1, \xi_2, \xi_3, ..., \xi_{n+p+1}] \tag{4.2.2}$$

whose knots ξ_i partition the parameter space into *elements*, or *knot spans*. Knot vectors may be *open* if the first and the last knot appear $p+1$ times. Moreover, if the knots are distributed equally along the parametric space, the knot vector is defined *uniform*. Given a knot vector $\mathbf{\Xi}$ it is possible to define the B-spline basis functions using the *Cox-de Boor* recursive formula. Starting from $p = 0$

$$N_{i,0}(\xi) = \begin{cases} 1 & if\ \xi_i \leq \xi < \xi i + 1 \\ 0 & otherwise \end{cases} \tag{4.2.3}$$

and for $p \neq 0$ Equation (4.2.3) can be generalized as

$$N_{i,p}(\xi) = \frac{\xi - \xi_i}{\xi_{i+p} - \xi_i} N_{i,p-1}(\xi) + \frac{\xi_{i+p+1} - \xi}{\xi_{i+p+1} - \xi_{i+1}} N_{i+1,p-1}(\xi) \tag{4.2.4}$$

As an example, a $p = 3$, $n = 10$ B-spline curve and its basis functions are depicted in Figure 4.2.

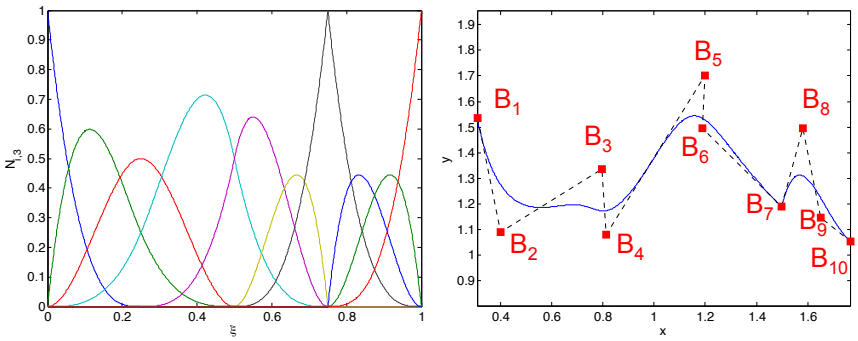

Figure 4.2 *Example of B-spline basis functions and curve: (left) Cubic basis functions generated by the knot vector* $\Xi = \{0, 0, 0, 0, 0.25, 0.5, 0.5, 0.75, 0.75, 0.75, 1, 1, 1, 1\}$*; (right) B-spline curve and its control points. The polygon constituted by the linear interpolation of the control points is the so-called control polygon.*

The main feature of B-Splines is the possibility to control the regularity on knot locations. In general, basis functions of order p present $p - m$ continuous derivatives across a given knot ξ_k, i.e., the basis is C^{p-m}, where m is the multiplicity of the knot ξ_k. In particular, if $m = p$ the basis is C^0 and interpolatory, as in classical FEA, while, if $m = p + 1$, the basis is discontinous and the boundary of the patch is defined. If a knot has multiplicity $m = 1$, maximum C^{p-1}-regularity is attained.
B-spline basis functions present many important properties (for a detailed description, please refer to [82]). Among them, it is remarkable to note:

- Partition of unity: $\sum_{i=1}^{n} N_{i,p}(\xi) = 1 \ \forall \xi$
- Compact support: Each basis function is equal to zero everywhere except on the interval $[\xi_i, \xi i + p + 1]$;
- Non-negativity: $N_{i,p}(\xi) \neq 0 \ \forall \xi$

- Linear independence: $\sum_{i=1}^{n} \xi_i N_{i,p}(\xi) = 0 \mid\mid \xi_j = 0$ j=1,2,...,n

Moreover, important properties of B-Splines curves are

- Convex hull property: the B-Spline curve is contained inside the convex hull of the control polygon;
- Continuity: the curve is C^{∞} between two knots between two knots and C^{p-m} at a knot location with multiplicity m;
- Affine transformation: affine transformations (scaling, translations, rotations) on the B-spline curve can be obtained transforming the control points accordingly.

Extension to surfaces and solids

B-spline surface and solid structure can be defined from tensor product combination of 2 (for surfaces) or 3 (for solids) 1D basis functions. Given p and q polynomial orders, n and m basis functions and two knot vectors $\mathbf{\Xi} = [\xi_1, \xi_2, \xi_3, ..., \xi_{n+p+1}]$ and $\mathcal{H} = [\eta_1, \eta_2, \eta_3, ..., \eta_{m+q+1}]$, a tensor-product B-spline surface is defined as

$$\mathbf{S}(\xi, \eta) = \sum_{i=1}^{n} \sum_{j=1}^{m} N_{i,p}(\xi) M_{j,q}(\eta) \mathbf{B}_{i,j} \tag{4.2.5}$$

The extension for solids requires and additional set of l basis functions with order r and a knot vector $\mathcal{Z} = [\zeta_1, \zeta_2, \zeta_3, ..., \zeta_{l+r+1}]$. The B-spline solid is defined as

$$\mathbf{V}(\xi, \eta, \zeta) = \sum_{i=1}^{n} \sum_{j=1}^{m} \sum_{k=1}^{l} N_{i,p}(\xi) M_{j,q}(\eta) L_{k,r}(\zeta) \mathbf{B}_{i,j,k} \tag{4.2.6}$$

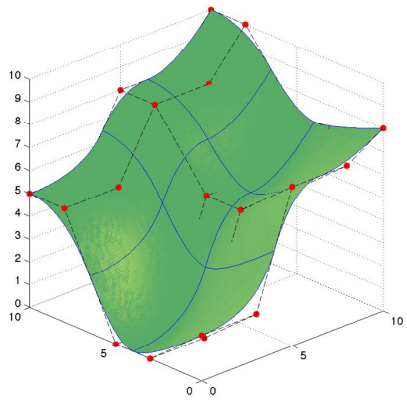

Figure 4.3 *Piecewise quadratic-quadratic polynomial surface and its control net .*

Both for surfaces and solids **B** represents the so-called *control net*, natural evolution of the control polygon in 1-D. It is important to remark that both surface and solid structures preserve the properties of 1D B-spline basis functions. Figures 4.3 and 4.4 show an example of quadratic-quadratic B-spline surface and quadratic-quadratic-linear B-spline solid, respectively. The isocurves mark the knots which partition the surface into elements. The boundaries of the surfaces are defined by the control points at the boundary and the vertices are interpolated.

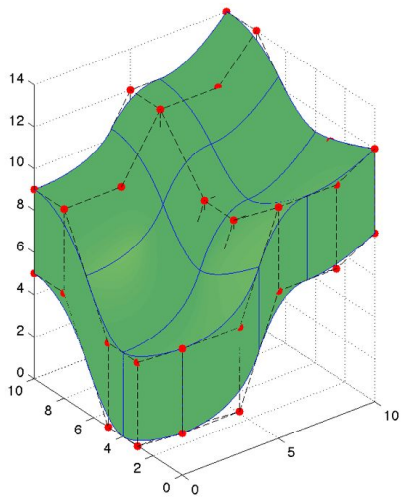

Figure 4.4 *Piecewise quadratic-quadratic-linear polynomial solid and its control net.*

4.2.2 Non-Uniform Rational B-Splines (NURBS)

The principal drawback of using polynomials as basis functions, including B-spline, is the inability to exactly represent a wide array of geometric objects. For this reason *rational* B-splines were introduced and became the current standard in CAD community. A $p-th$ order NURBS curve is represented as

$$\mathbf{C}(\xi) = \frac{\sum_{i=0}^{n} N_{i,p}(\xi) w_i \mathbf{B_i}}{\sum_{i=0}^{n} N_{i,p}(\xi) w_i}. \tag{4.2.7}$$

where B_i are the control points coordinates defined in $\mathbb{R}^d$, w_i are the *weights*, ξ is the knot representing the parametric coordinates and $N_{i,p}(\xi)$ are the p-th order B-spline basis functions. A NURBS curve in $\mathbb{R}^d$ can be seen as the projective transformation of a B-spline entity in $\mathbb{R}^{d+1}$ (see Fig.4.5). The transformation is applied by projecting every point by mean of the weight w_i. NURBS surfaces and solids can be constructed in the same way described in the previous section. Using NURBS basis functions all

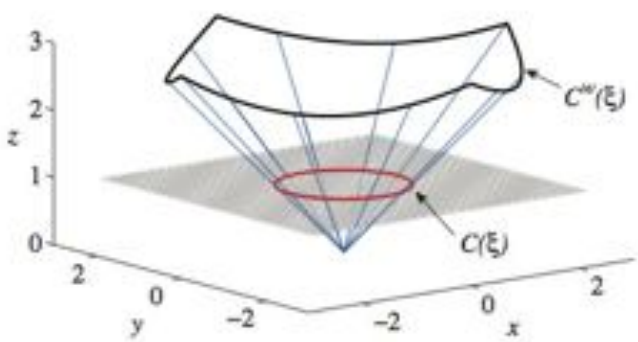

Figure 4.5 *A circle in $\mathbb{R}^2$ constructed by the projective transformation of a piecewise quadratic B-spline in $\mathbb{R}^3$ [18].*

the conic sections, such as circles and ellipses, can be exactly constructed by projective transformations of piecewise quadratic curves, making this technology the most popular in CAD community. NURBS basis functions preserve all the properties of B-spline functions:

- Partition of unity: $\sum_{i=1}^{n} N_{i,p}(\xi) = 1 \ \forall \xi$;
- Local support: Each basis function is equal to zero everywhere except on the interval $[\xi_i, \xi i + p + 1]$;
- Non-negativity: $N_{i,p}(\xi) \neq 0 \ \forall \xi$;
- Affine invariance: An affine transformation applied to the NURBS object is equivalent if it's applied directly on the control points.

4.3 Isogeometric analysis

Hughes and colleagues coined the term *Isogeometric Analysis* (IgA) in 2005 [17]. The initial motivation of IgA lied into the desire of reducing the engineering time for model generation, using a single mathematical representation for both design and analysis. In particular, IgA can be seen as an enhanced exploitment of the "isoparametric concept". The isoparametric concept states that the unknown variables, i.e., the nodal displacements, and the model geometry are represented in terms of the same basis functions. Such concept is a fundamental requisite for the exact approximation of rigid body motions and constant strain states [83]. However, traditional FEA employ low-order, mostly linear shape functions to approximate the solution while CAD software employ high-order high-continuity spline functions (like the NURBS described above) to reproduce the model geometry. For this reason, the CAD model needs to be converted in a format suitable for FEA. During such a process, called *meshing*, the high-order high-continuity CAD model is converted in a finite set of low-order, low-continuity FEA elements. Meshing presents the following drawbacks:

- FEA mesh is just an approximation of the real geometry. However, the exact representation of the geometry can be crucial in many engineering applications, i.e., buckling analysis and contact problems;

- Meshing is a bottleneck process for a wide variety of industrial applications (Fig. 4.6). In particular, meshing of complex structures needs manual modifications before FEA and, in general, the whole process needs to be repeated every time the mesh needs to be modified (Fig. 4.7).

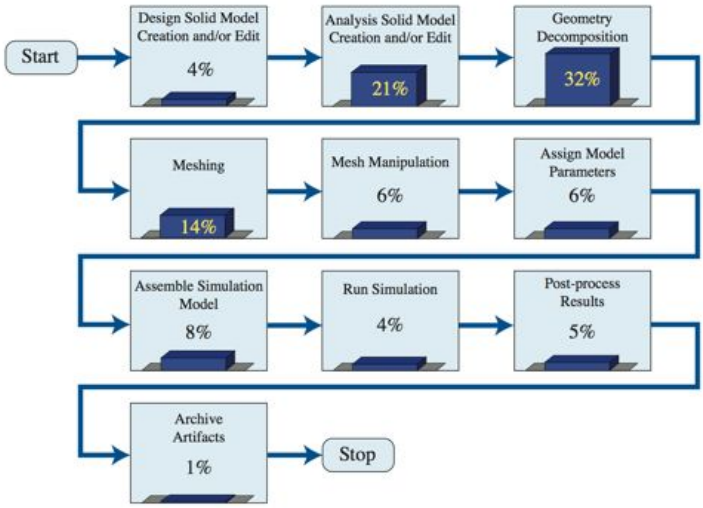

Figure 4.6 *Estimation of the relative time costs of each component of the model generation and analysis process at Sandia National Laboratories. Note that the process of building the model completely dominates the time spent performing analysis [18].*

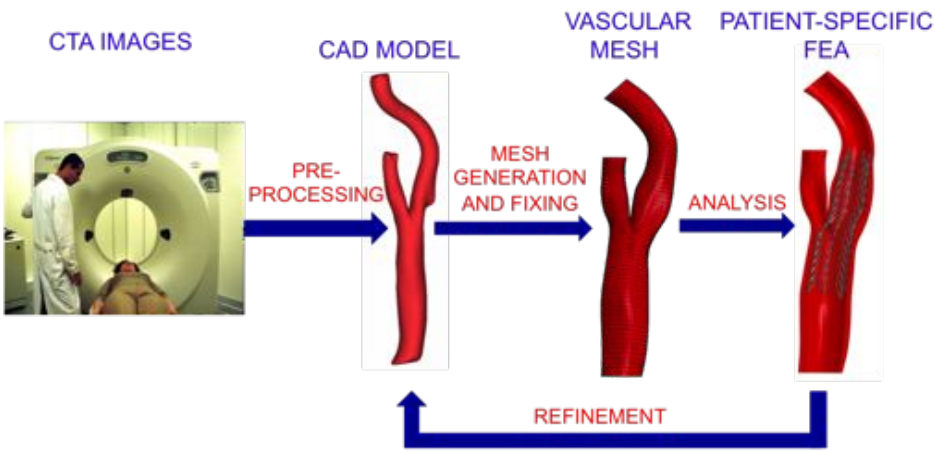

Figure 4.7 *Patient-specific FEA framework*

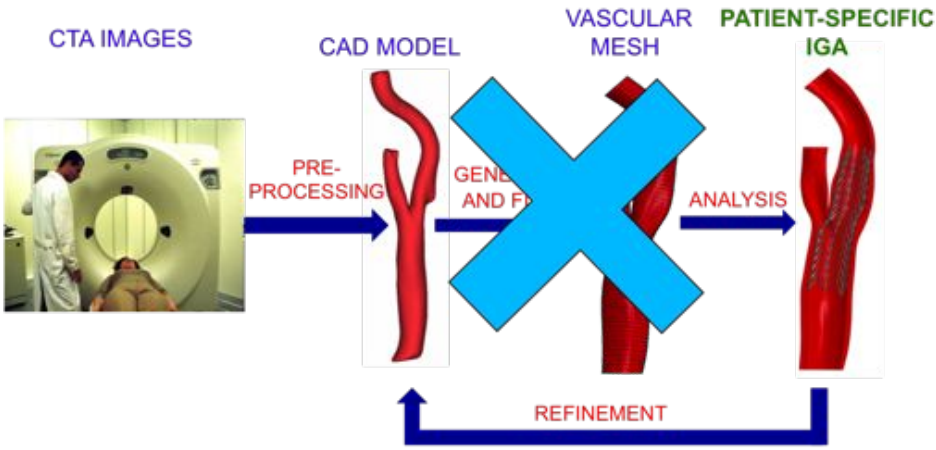

Figure 4.8 *Patient-specific IgA framework.*

The idea of isogeometric analysis is that the NURBS basis functions used for the geometry description in CAD can be employed both by the geometry description and the solution framework (isoparametric concept). Within this context the whole process of meshing can be bypassed and the two models for design and analysis merge into one (Fig. 4.8).

The following points about IgA need to be considered:

- NURBS parameter space is local to patches rather than elements. That is, the parameter space in FEA is mapped into a single element in the physical space, while in IgA the mapping is global and applied to the whole patch;

- Gauss quadrature is employed for the integration of the weak form components at the element level. Such choice has been proven to be a reliable tool in the literature [17].
  However, ad-hoc efficient integration rules taking advantage of the

NURBS high continuity [84, 85];

- Polynomial order p and knot vector Ξ define the approximation properties of the patch;
- The control points associated with the basis functions define the geometry.

4.3.1 Refinement

IgA refinement techniques slightly differ from their FEA counterparts. First, B-splines and NURBS basis can be enriched while leaving the underlying geometry and its parameterization intact. Moreover, besides control over the element size and the order of the basis, IgA allows to control the continuity of the basis as well. In the following, the three IgA refinement techniques, i.e., h,p and k refinement are presented and compared, when available, with their FEA counterpart.

h-refinement: the knot insertion

The most intuitive technique to enrich the NURBS basis is the *knot insertion*. In knot insertion, the knot spans are divided into smaller ones by inserting new knots without changing the NURBS curve geometrically or parametrically. Clearly, for each knot inserted, an additional control point is inserted (see Fig. 4.9). Also knot values already present in the knot vector may be repeated, increasing their multiplicity and reducing the continuity at that knot location. Insertion of new knot values clearly has similarities with the classical h-refinement strategy in FEA. It differs, however, in the lower number of new functions that are created, as well as in the continuity of the basis across the newly created element boundaries.

p-refinement : the order elevation

Order elevation involves the raising of the polynomial order of the basis functions used to represent the geometry (see Fig. 4.10). In order to preserve geometric and parametric definition of the original NURBS structure, when order p is increased, knot multiplicity m must also be increased to preserve the original C^{p-m} continuity at knot locations. Clearly, the

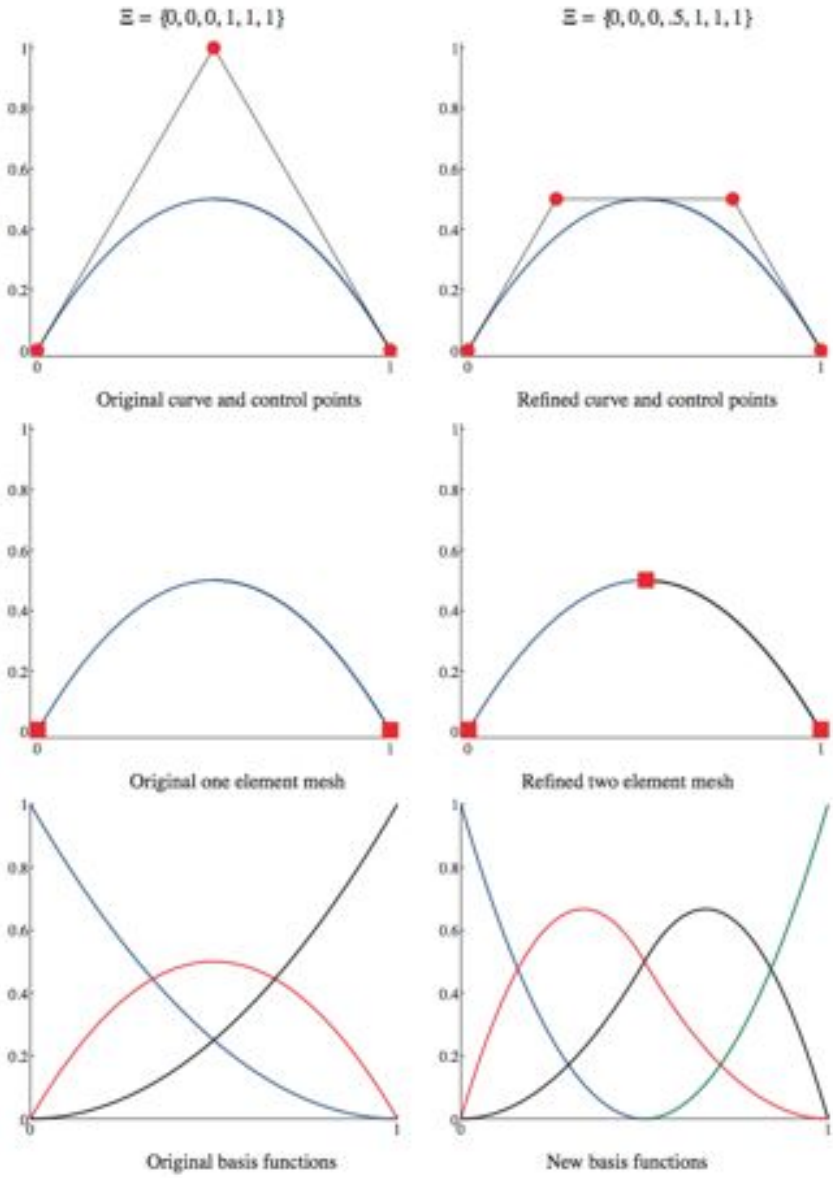

Figure 4.9 *Knot insertion: Control points are denoted by ●. The knots, which define a mesh by partitioning the curve into elements, are denoted by ■ [18].*

locations of the control points change, but the elevated curve is geometrically and parametrically identical to the original curve. Order elevation has many similarities with the classical p-refinement strategy in FEA. The major difference is that p-refinement always begins with a basis that is C^0 everywhere, while order elevation is compatible with any combination of continuities that exist in the original NURBS mesh.

k-refinement

Besides two techniques, i.e., knot insertion and degree elevation, that find similarities with traditional FEA refinement techniques, IgA offers additional possibilities. In particular, k-refinement, i.e., a sort of high continuity h refinement, is available. Starting from the fact the h and p-refinement techniques do not commute we can have:

- If a unique knot ξ_i is inserted between two distinct knot values in a curve of order p, the basis will be C^{p-1} at that knot location. Subsequently the order is elevated to q, and the multiplicity of every distinct knot value (including the knot just inserted) is increased so that discontinuities of the basis are preserved. In such a process, the basis is still C^{p-1} at ξ_i, even if the polynomial order is now q. This process is defined as hp refinement (Fig. 4.11-a).

- On the contrary, if the basis is at first elevated from order p to q and subsequently insert knot ξ_i, the resulting basis will be C^{q-1} at knot ξ_i location. This process is defined as k-refinement and there is no analogous technique in standard FEA (Fig. 4.11-b).

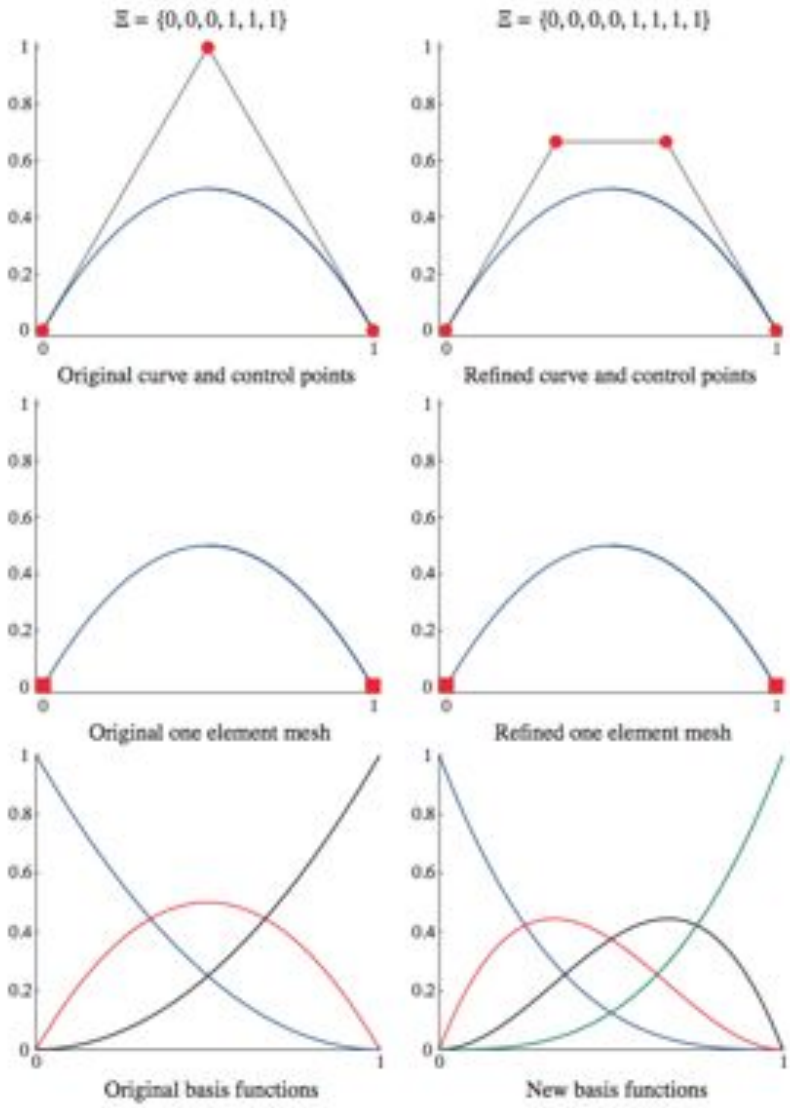

Figure 4.10 *Order elevation: Control points are denoted by ●. The knots, which define a mesh by partitioning the curve into elements, are denoted by ■ [18].*

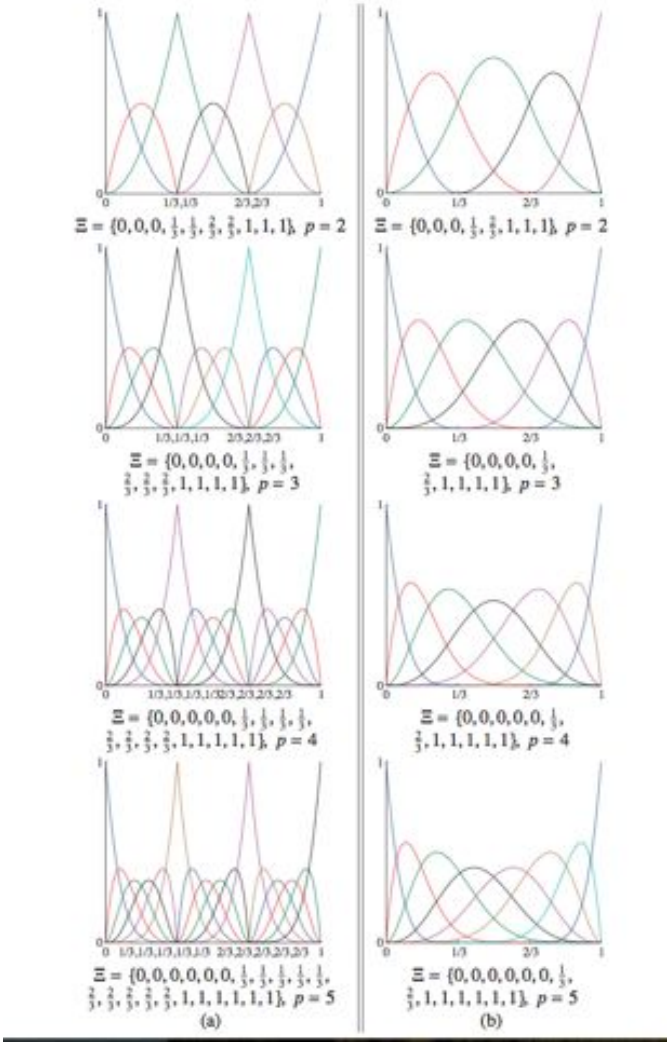

Figure 4.11 *Three element, higher-order meshes for hp and k-refinement. (a) The p-refinement ap- proach results in many functions that are C^0 across element boundaries. (b) In comparison, k-refinement results in a much smaller number of functions, each of which is C^{p-1} across element boundaries [18].*

4.4 State of the art

Since its introduction by Hughes et al. [17], NURBS-based IgA aroused great interest in the scientific community and, in the following, a brief overview of the different studies on IgA is provided.

The first works by Bazilevs et al. [86] and Cottrell et al. [18] aimed at assessing the approximation property, stability and error estimates for h and p refinements.

The analysis of structural vibrations was the first application proving the IgA computational advantages over traditional FEA [87, 88, 89]. In particular, the employment of k-refinement provided more robust and accurate frequency spectra than typical higher-order finite elements eliminating "optical" branches of frequency spectra.

Starting from these promising results, the range of IgA applications rapidly expanded. In particular, shell modeling is one of the most promising IgA application fields. In this aspect, we remark the innovative works of Kiendl et al. [90] for Kirchhoff-Love shells and Benson et al. [91] for the Reissner-Mindlin shells.

Moreover, the easy implementation of k-refined elements makes IgA very interesting for the approximation of high-order problems. In this aspect Buffa et al. [92] introduced a B-spline based discretization scheme for Maxwell equations in two space dimension, while Gomez et al. [93] and Vilanova et al. [94] applied NURBS-basis functions to solve Cahn-Hiliard equations and tumor angiogenesis modeling, respectively.

Another interesting application of the IgA concept is the analysis of nearly incompressible solids. In this aspect, Taylor [95] presented a three-field variational structures and tensor product NURBS approximations, while Elguedj et al. [96] proposed B-bar and F-bar projection methods for

nearly incompressible material in small or large deformation.

The principal aim of IgA, i.e., link design model and geometric description, provided a breeding ground for different investigations on shape optimization techniques. In this aspect, we remark the results obtained by Kiendl [97] and the works by Wall et al. [98] and Cho et al. [99].

Moreover, IgA, from its original structural environment, rapidly extended to fluid mechanics applications and turbulent flows. As example we remark the different works of Bazilevs [100, 101, 102].

More recently, the high continuity of the IgA basis has been applied to solve the strong form of the corresponding partial differential equation, within a novel family of IgA collocation methods [103, 104]. The novel numerical method has demonstrated to be extremely efficient in terms of numerical costs and especially attractive for problems where the evaluation of the stiffness matrix is an important aspect.

In conclusion,during the last few years IgA has been employed to treat many other critical aspects of traditional FEA, e.g., contact treatment [105, 106] (this aspect is detailed in Chapter 6) , large deformation problem with mesh distortion[107] and wave propagation problems [108].

The research is now exploring different solution to extend and enrich the features and the computational framework provided by the original NURBS-based IgA. From the geometrical point of view, the major effort is nowadays dedicated on the implementation of IgA schemes able to overcome the tensor product nature of NURBS basis functions. In this aspect, different novel parametrizations, e.g., T-splines [109, 110], hierarchical B-splines [111] and LR- B-splines [112], have been proposed as alternatives able to overcome the tensor product limitation. From the numerical point of view, many studies focused on the implementation of efficient and IgA-suited quadrature rules [84, 85], while the work of Collier et al. [113] highlighted

the need of *ad-hoc* solvers to enhance the IgA computational efficiency.

This is just a short list of the many numerical aspects where IgA can provide benefits with respect to traditional numerical methods, and the number of innovative applications is growing year after year as demonstrated by the great interest in the scientific community (Fig. 4.12).

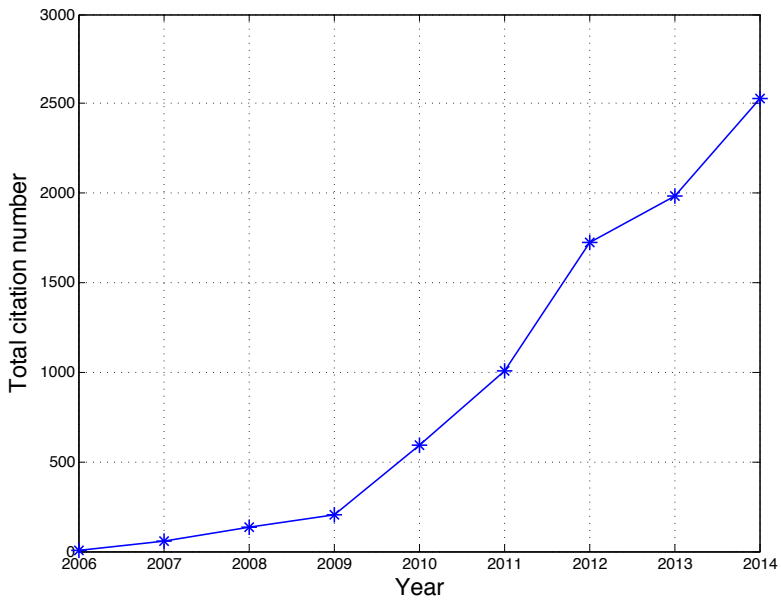

Figure 4.12 *Total number of citations per year using the keyword "Isogeometric analysis" (source: SCOPUS).*

Chapter 5

Stent bending modeling: a comparison between FEA and IgA

Following the IgA basics introduced in Chapter 4, we now aim at investigating the IgA benefits within the vascular biomechanics framework. In particular, vascular biomechanics can take advantage of highly accurate geometric description for both biomedical devices and biological structures. Moreover, IgA can provide a smooth description of complex phenomena, such as contact and buckling phenomena. Within this context, this chapter aims at investigating an important feature for carotid artery stents, i.e., flexibility by mean of traditional FEA and innovative IgA. In addition, an IgA-based application focusing on the efficient creation of analysis-suitable vascular models is detailed in Appendix B.

5.1 Problem definition

In the last decade use of carotid artery stents (CAS) for stroke prevention has rapidly evolved as a reliable alternative to the traditional approach

of carotid endarterectomy. As an example, in the United States CAS expanded from less than 3% of the total number of carotid artery revascularization procedures in 1998 to 13% in 2008 [114]. The key device of CAS is the so-called *stent*, a metallic frame that is driven to the target lesion to restore the carotid artery patency by enlarging the narrowed lumen.

A proper delivery and placement of endovascular stent devices is of utmost importance to ensure the safety and performance of the implant. For this reason, an adequate stent flexibility, typically evaluated by means of bending tests, plays an important role in the stent delivery process as well as in the reduction of the stress generated by the interaction between the device and the surrounding biological tissue.

Therefore, the quantitative evaluation of mechanical and geometrical properties is of critical relevance for a reliable characterization of stents already available on the market or during the design process of new devices. This topic has been widely investigated in the literature, both from the experimental and the numerical point of view. In particular, different experimental benchmarks were proposed with particular emphasis on coronary artery stents [115, 116, 117]. However, only the works of [15] and [118] implemented an experimental benchmark for carotid artery stents. The experimental properties are typically evaluated through comparative studies between different stent designs and include flexibility, radial stiffness, cell scaffolding, foreshortening, and elastic recoil. On the other side, many virtual benchmark tests, typically based on structural Finite Element Analysis (FEA), have been developed as a complementary tool to the experimental studies [19, 77, 119, 120, 121].

Within this context, FEA is widely employed when experimental tests are difficult to implement or when a large number of materials, geometries, and loading conditions need to be investigated before prototype fabrication.

In particular, [117] studied the flexibility of four coronary artery stents by means of a two-dimensional (2D) FEA model resembling a small portion of the complete device. [119] and [19] proposed a there-dimensional (3D) FEA model for stainless steel and adsorbable metallic coronary stents, respectively. Both models reproduce only a portion of the complete device. Eventually, [77] proposed a virtual flexibility test for coronary artery stents based on a multipoint constraint. They implemented a 3D FEA model of a full device.

We believe our work is the first numerical study approaching the flexibility evaluation for carotid artery stents within a computational framework applied to a 3D model of the whole device.

In our view, FEA presents some drawbacks that can limit the description of the domain under investigation and the regularity of the approximated solution. In particular, the low-order and low-regularity polynomials used to discretize the continuum domain do not allow, in general, to accurately represent complex geometries unless extremely fine meshes are adopted. At the same time, FEA basis functions do not allow one to properly approximate the solution without resorting to a high number of degrees of freedom.

Isogeometric analysis (IgA) has recently been developed as an exact-geometry, cost-effective alternative to classical FEA [17, 18]. Roughly speaking, IgA proposes to replace the low-order, low-regularity FEA basis functions with the high-order, high-regularity basis functions employed in computer-aided design (CAD) while retaining an isoparametric framework. In particular, non-uniform rational B-splines (NURBS) were initially chosen as the basic environment for IgA due to their widespread use in the CAD community, but nowadays other more flexible options also are available ([18, 102]).

An initial motivation for IgA was a desire to reduce the engineering time for model generation by using a single mathematical representation for both design and analysis. However, the higher regularity of IgA shape functions with respect to FEA extended the range of applications to all the fields in which high continuity plays a preeminent role, e.g., the study of structural vibrations [87, 89, 108, 122], the analysis of nearly incompressible solids [95], novel contact formulations [106], turbulent flows [100], and fluid-structure interaction [102].

Only a few works have investigated the features of IgA applied to vascular biomechanics. In particular, [123] focused on the geometrical representation of complex vascular branches to get accurate, IgA-suitable models for the analysis of blood flow. [101] and [102] developed an IgA-based fluid structure interaction model, developed within an Arbitrary Lagrangian Eulerian framework, to investigate the interaction of the arterial wall and the blood flow. [124] developed a computational framework to compare the performance of IgA and FEA applied to the structural closure of a patient-specific aortic valve model. The work of [124] is the first structural investigation addressing the benefits of IgA with respect to benchmark FEA shell elements applied to vascular biomechanics.

Within this context, the present paper represents the first study investigating the impact of structural IgA for the evaluation of the mechanical properties of endovascular devices. In this work we consider the behavior of two carotid artery stent designs that resemble two commercially available devices. NURBS-based IgA and classical FEA are adopted to model the 3D bending problem in a large deformation regime corresponding to the cantilever beam bending experiment proposed by [15]. In our work we develop a computational framework able to automatically obtain an IgA-suitable stent discretization from the CAD model. Moreover, our framework also

is extended to automatically obtain an equivalent highly structured finite element mesh.

Two different constitutive models are considered, i.e., an elastic Saint Venant-Kirchhoff material and an inelastic shape memory alloy (SMA) model implemented within in a large displacement-small strain regime. Both IgA and FEA bending tests are performed using the general purpose solver FEAP [125] and its additional package for IgA.

The results include a performance comparison, on a per-degree-of-freedom basis, between IgA and FEA with respect to both local (reaction force) and, when possible, global (stored energy) quantities. Moreover, we highlight the capability of the two methods to reproduce the nonlinear local effect occurring when a particular stent design is considered.

The chapter is structured as follows: In Section 5.2 we describe the proposed computational framework, including geometrical modeling, adopted constitutive relations, and analysis setup. In Section 5.3 we present and discuss some numerical results for each combination of stent design and constitutive models. This section is structured in order to highlight not only a general comparison in terms of number of degrees of freedom, but also a focus on local nonlinear effects. At last, in Section 5.4 we summarize our findings.

5.2 Materials and Methods

In this section the computational framework to obtain IgA–suitable stent models directly from CAD is described. Subsequently, the constitutive models used in our study are described. In particular we use a formulation under the hypothesis of large displacements but small strains that are typically induced in many biomedical applications [126]. Such geometrical models and constitutive laws are then integrated within an analysis setup simulating an experimental stent bending test.

5.2.1 Stent Model

A novel computational framework to interface the CAD software Rhinoceros v. 4.0 SR8 (McNeel and Associated, Seattle, WA, USA) with the general purpose solver FEAP is presented. Two different self-expanding carotid stent designs are considered. They resemble two commercially available stents used in clinical practice. In the following they will be referred to as Model A and Model B, resembling respectively a Bard ViVEXX Carotid Stent (C. R. Bard Angiomed GmbH & Co., Germany) and a XACT Carotid Stent (Abbott, Illinois, USA).

The choice of these carotid artery stents is motivated by the different designs that can significantly impact the global mechanical behavior. In fact, while Model A is an *open-cell* stent, i.e., adjacent ring segments are not connected at every junction, Model B is a *closed-cell* stent, i.e., all junctions are connected. The two different designs influence many biomechanical outcomes, e.g., vessel scaffolding, adaptability, and flexibility.

Given the comparative nature of our study, for both designs we consider a straight configuration having a 9 mm reference diameter and a 30 mm length. Since no data are available from the manufacturer, the main geo-

metrical features of such devices are derived from high-resolution micro-CT scans (viz. Fig. 5.1-a) of the crimped stent in the delivery system [120]. Each stent model is generated through the following steps:

- A planar CAD geometry (see Fig. 5.1-b) corresponding to the stent unfolded configuration is generated. Subsequently, a 2D CAD surface is generated for each NURBS patch.

- The NURBS data (control points, knots and weights) are exported as text files by mean of an in-house code developed in Visual Basic Scripting;

- The NURBS surface structure is extruded and rolled by mean of an in-house Matlab code (The Mathworks Inc. Natick, MA, USA) leading to the final stent in open configuration as depicted in Fig. 5.1-c.

- Each patch composing the trivariate NURBS structure is finally exported in a suitable format for the solver FEAP. The control points at the (conforming) interface between two adjacent patches are tied together in order to obtain the IgA stent model.

The stent models A and B are composed by 87 and 191 NURBS patches, respectively. The stent structure is regular and is composed of two patch families, i.e., link and ring patches. We note that model A can be easily represented by two different patches (see Fig. 5.1-d), however, model B has a more complex structure that requires one ring and three linker patches.

Given the basic NURBS representation, the adopted refinement techniques are graphically represented in Fig. 5.2. In particular, starting from the CAD-based NURBS model (Fig. 5.2-*top*), we consider the following refinement techniques for IgA and FEA, respectively.

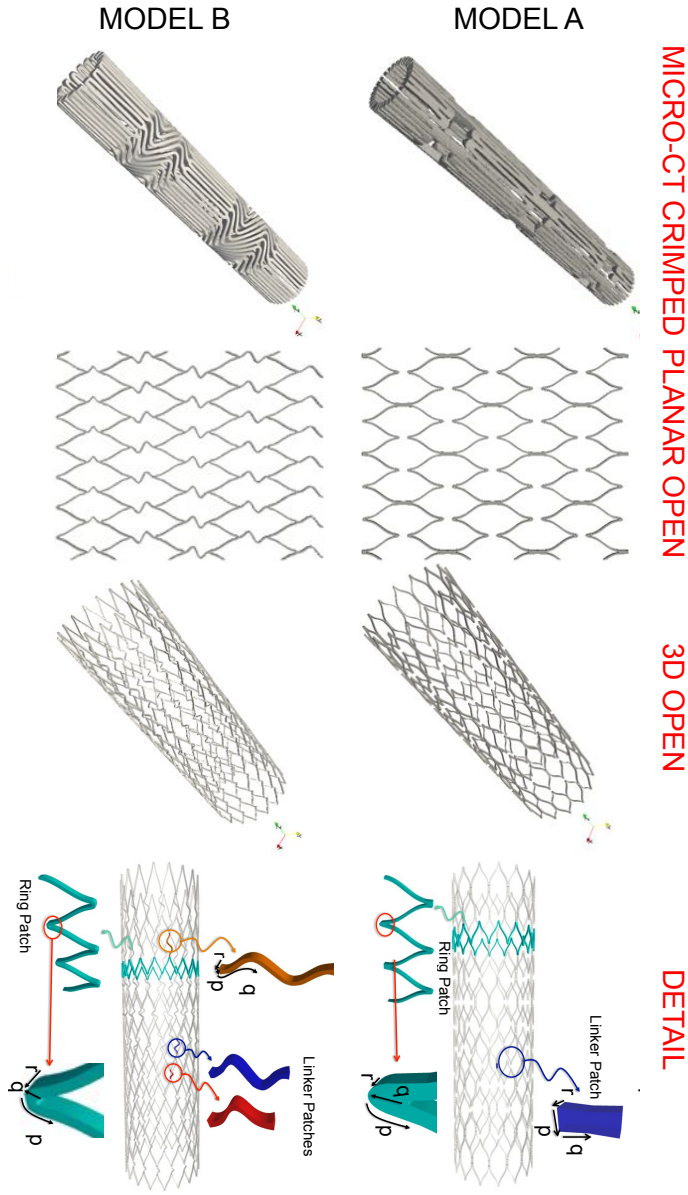

Figure 5.1 *IgA stent generation: (a) detail of a high resolution micro-CT performed on the real stents within the delivery system; (b) planar CAD geometry resembling the stent design pattern; (c) IgA-suitable stent model; (d) longitudinal view with detail of the two patch families, i.e., linkers and rings, and orientation of the three parametric directions p, q, r.*

For the IgA models we implement a k-refinement routine following the steps depicted in Fig. 5.2-*left*. This approach allows one to elevate the polynomial order and, at the same time, to increase the smoothness of the basis functions.

Moreover, in order to get a set of reliable finite element meshes we extend the proposed computational framework. In particular, we perform a set of fictitious knot insertions in order to subdivide each knot span into n distinct subdivisions. Each fictitious knot location in the parametric space, defined as *evaluation point*, has a mapped counterpart in the physical space.

We use this information to build an equivalent finite element mesh with the mapped evaluation points as nodal coordinates and element connectivity derived from the tensor-product structure of the NURBS geometry. We remark that given the adopted 8-node brick shape functions only C^0 continuity is enforced at the evaluation point locations in the FEA model.

Taking advantage of this property we are able to build different equivalent finite element meshes directly from the NURBS model in a straightforward way. This approach allows us to get easily a refined mesh, because it is only needed to increase the refinement index n (three different refinement examples are depicted in Fig. 5.2-*right*). It is remarkable to observe that, given the higher density of knot spans in the curved regions, the choice of a uniform number of subdivisions n per knot span allows us to automatically refine "locally" the model regions with higher curvature.

Both refinement techniques are implemented within an in-house Matlab code based on the NURBS toolbox [127, 128], and a set of routines implementing the algorithms included in [82].

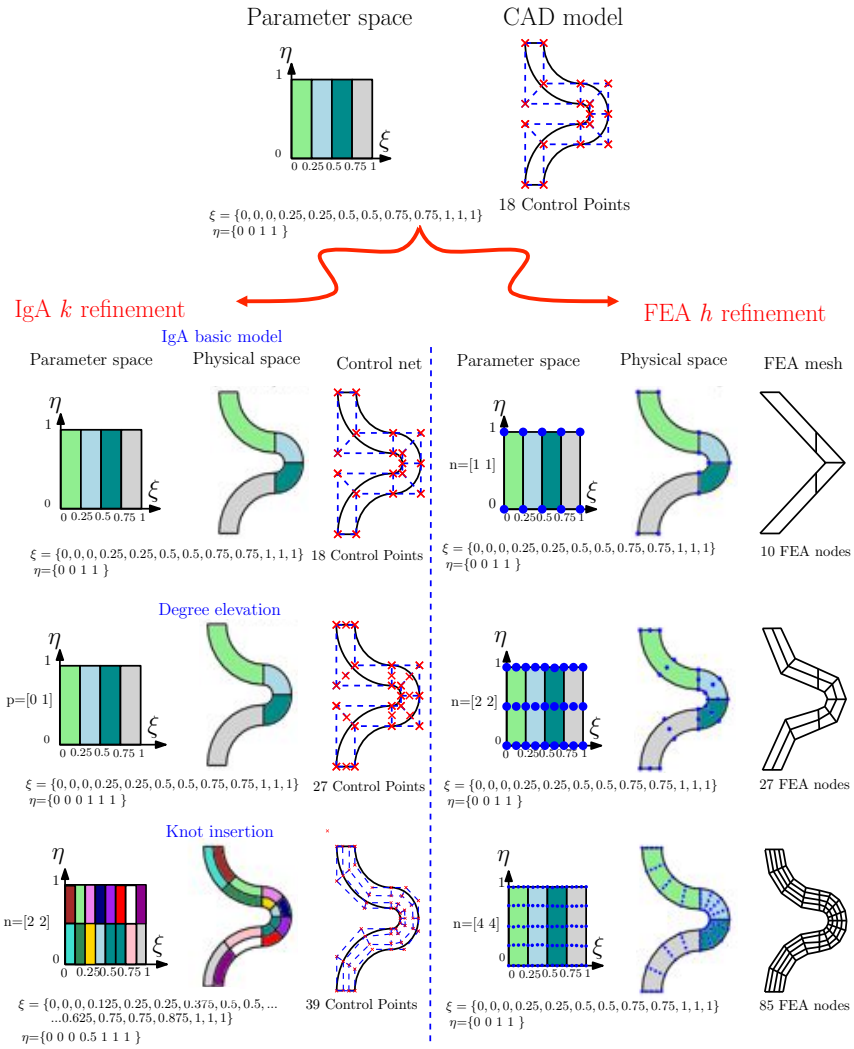

Figure 5.2 *Adopted refinement techniques: (top) initial CAD model and parametric space; (left) IgA k-refinement steps, the NURBS control points are depicted as x; (right) equivalent h-refined FEA mesh with different refinement indexes n, the evaluation points in the parametric space are depicted as ●.*

5.2.2 Constitutive models

We perform our investigations considering two constitutive models: a simplified Saint Venant-Kirchhoff model and a phenomenological shape memory alloy model (based on the work of [21]).
More details on the adopted constitutive models are given in the following.

- Saint Venant-Kirchhoff material: this model is a simple hyperelastic constitutive law that is a direct extension of an isotropic linear elastic material to the large deformation regime. The model is derived from the following stored energy function [129]:

$$\Psi(\boldsymbol{E}) = \tfrac{1}{2}\lambda\,[\mathrm{tr}(\boldsymbol{E})]^2 + G\,\mathrm{tr}(\boldsymbol{E}^2), \tag{5.2.1}$$

$$\mathbf{E} = \tfrac{1}{2}(\mathbf{F}^T\mathbf{F} - \mathbf{I}), \tag{5.2.2}$$

  being $\mathbf{E}$ the Green-Lagrange strain tensor, $\mathbf{F}$ the deformation gradient and $\mathbf{I}$ the identity tensor. The Lame's material parameters λ and G are defined in terms of the small strain Young's modulus E and Poisson's ratio ν, as

$$\lambda = \frac{\nu E}{(1+\nu)(1-2\nu)}, \qquad G = \frac{E}{2(1+\nu)}. \tag{5.2.3}$$

  For the problem under investigation we assume the elastic properties of the coronary artery stent model from the work of [130], i.e., $E = 196$ GPa and $\nu = 0.3$.

- SMA phenomenological model: in order to mimic behavior of self-expanding Nitinol stents, the Souza model described in Chapter 2 [21] is adopted.

Under the assumption of large displacements and rotations, but small strains, we use the following additive decomposition:

$$\mathbf{E} = \mathbf{e} + \tfrac{1}{3}\theta\mathbf{I}, \tag{5.2.4}$$

where

$$\theta = tr(\mathbf{E}) \qquad \mathbf{e} = \mathbf{E} - \tfrac{1}{3}\theta\mathbf{I}, \tag{5.2.5}$$

The model assumes the deviatoric strain, $\mathbf{e}$, the volumetric strain, θ,

and the absolute temperature, T, as control variables and the second-order transformation strain tensor, $\mathbf{e}^{tr}$, as an internal variable. The quantity $\mathbf{e}^{tr}$ plays the role of describing the strain associated to the phase transformations. The model is derived from the following energy function:

$$\begin{aligned}\Psi(\theta, \mathbf{e}, T, \mathbf{e}^{tr}) =& \frac{1}{2}K\theta^2 + G\|\mathbf{e} - \mathbf{e}^{tr}\|^2 - 3\alpha K\theta(T - T_0) + \beta\langle T - T_0\rangle\|\mathbf{e}^{tr}\| + \\ & \frac{1}{2}h\|\mathbf{e}^{tr}\|^2 + (u_0 - T\eta_0) + c\left[T - T_0 - T\log\left(\frac{T}{T_0}\right)\right] + \mathcal{I}_{\varepsilon_L}(\mathbf{e}^{tr}),\end{aligned} \tag{5.2.6}$$

where K and G are, respectively, the small strain bulk ($K = \lambda + 2G/3$)

and shear modulus, α is the thermal expansion coefficient, β is a material parameter associated with the stress-temperature relation, T_0 is the reference temperature, h is the hardening parameter associated with the transformation phase, c is the heat capacity, and u_0, η_0 are, respectively, the internal energy and the entropy, while the symbol $\langle\cdot\rangle$ is the positive part function. $\mathcal{I}_{\varepsilon_L}(\mathbf{e}^{tr})$ is an indicator function introduced to satisfy the constraint $\|\mathbf{e}^{tr}\| \leq \varepsilon_L$.

We implement the model version proposed by [27] in a large displacement-small strain regime. The related constitutive parameters are obtained from the literature [131] and we use the same material properties for both stent models.

5.2.3 Analysis setup

The stent bending problem has been approached in the literature in different ways from the experimental point of view, e.g., by means of the cantilever beam test [15, 115], the three point bending test [116] and the four point bending test [117, 118].

The most complete experimental benchmark applied to carotid artery stents in terms of variety of tests and number of considered designs is the cantilever beam test studied by [15]. We remark that our work aims at evaluating the performance of IgA and FEA applied to a real-life stent bending problem. Therefore, the quantitative comparison of numerical and experimental results is beyond the scope of this study. In particular, a quantitative comparison requires further investigations in terms of material parameters calibration from experimental data and analysis of experimental boundary conditions. Following the approach proposed by [131], the bending test is simulated through a displacement-based analysis in the large deformation regime. A displacement of 11 mm along the Y direction is imposed for all control points referring to the distal extremity of the stent, while the proximal one is clamped (viz. Fig. 5.3). We consider the resultant reaction force at the distal extremity of the device as a reference quantity to evaluate the capability of IgA and FEA to correctly reproduce the stent bending as also used in the experimental setup proposed by [15]. Given the refinement techniques for IgA and FEA presented

in section 5.2.1, we use six h-refined FEA meshes with different combinations of subdivision indexes n, while for IgA we consider the mesh with the basic parametrization coming from the CAD (labeled as IgA-1) and three k-refined IgA meshes. Moreover, in order to better investigate the geometrical instabilities observed in Model B for the SMA constitutive model, we perform two additional FEA h-refined simulations, i.e., FEA-7 and FEA-8. These analyses are computationally intensive and thus for efficiency reasons are performed using the Abaqus/Standard solver ver. 6.11 (Dassault Systémes, Johnson, RI, USA)[1].

The description of all analyses in terms of numbers of degrees of freedom (DOF) and polynomial degree can be found in Tables 6.2, 5.2, 5.3, and 5.4.

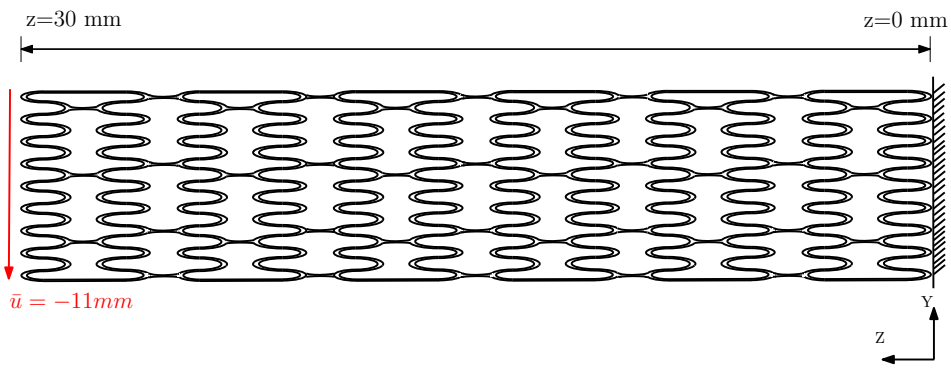

Figure 5.3 *Stent bending simulation schematic picture.*

5.3 Results and discussion

In this section we present the numerical results relative to different combinations of stent design, i.e., Model A or B, and constitutive relations, i.e.,

[1]Both IgA and FEA simulations are performed on an Intel Xeon E5-4620 @ 2.20 GHz workstation with 252 Gb RAM.

Saint Venant-Kirchhoff or SMA, all exploiting the proposed computational framework.

In order to evaluate the suitability of our approach, we first evaluate the convergence of IgA and FEA elastic simulations with respect to reaction force and stored energy quantities. In particular, the convergence of Models A and B for the Saint Venant-Kirchhoff material is depicted in Fig. 5.4. Moreover, the values of the involved quantities and their relative error with respect to the finest IgA model (labeled as IgA−4) are reported in Tables 6.2 and 5.2 for Model A and B, respectively.

Based on the assumption that the reaction force is a proper measure for convergence evaluation, as deduced from our elastic analyses and experimental studies of [15], we next consider the mechanical response of Models A and B using the SMA constitutive law. In particular, the force-displacement curves for FEA and IgA simulations are depicted and compared in Fig. 5.5. In addition, convergence plots with respect to the number of degrees of freedom (DOF) for both models are shown in Fig. 5.6. Finally, the data concerning reaction force values and relative errors with respect to IgA−4 are reported in Tables 5.3 and 5.4 for Model A and B, respectively.

Our goal is to evaluate the potential of IgA in simulating the stent behavior comparing its performance with respect to classical FEA. As previously indicated, we consider the resultant reaction force at the distal extremity of the stent as a reference quantity to evaluate the performance of IgA and FEA with respect to the number of DOF.

However, convergence is typically evaluated with respect to a global quantity such as the elastic deformation energy, while the reaction force represents only a local one. Unfortunately, the elastic stored energy results are meaningless when an inelastic model is employed, such as the SMA constitutive law adopted in this study. Therefore, in order to evaluate the

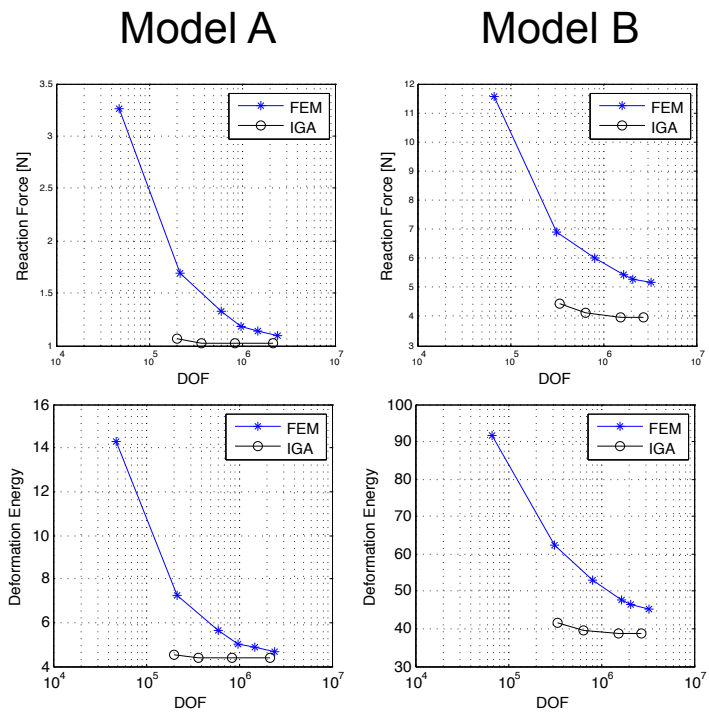

Figure 5.4 *Reaction force (top) and deformation energy (bottom) convergence plots in case of Saint Venant-Kirchhoff constitutive model.*

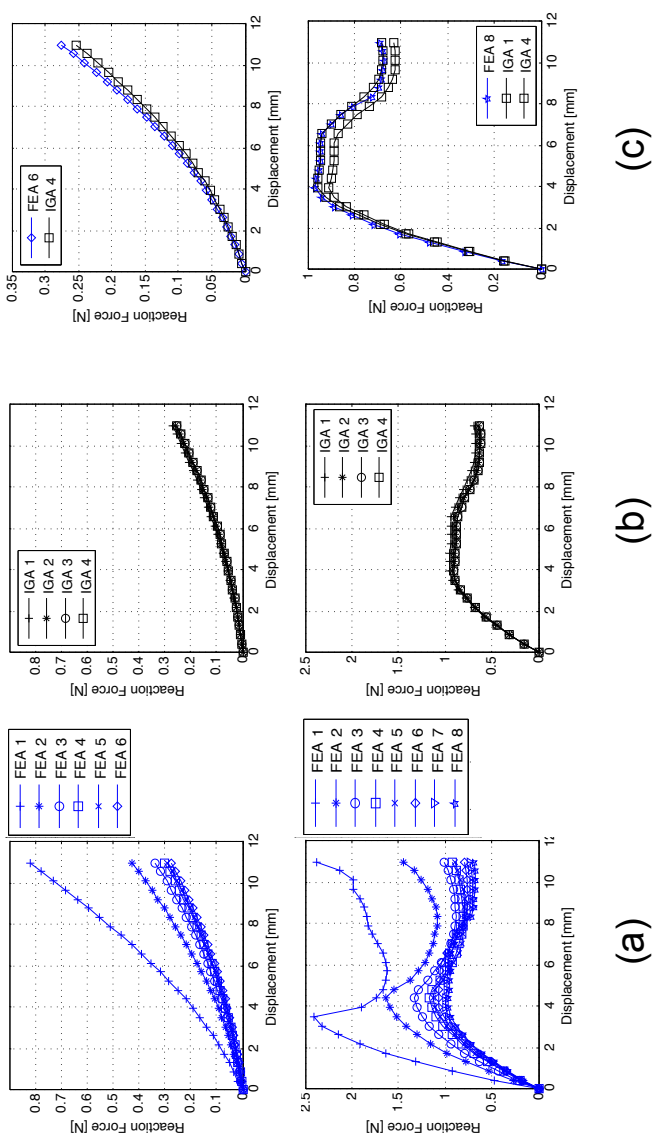

Figure 5.5 *Force-displacement diagrams in case of SMA constitutive model: (a) FEA; (b) IgA; (c) finest FEA versus finest IgA.*

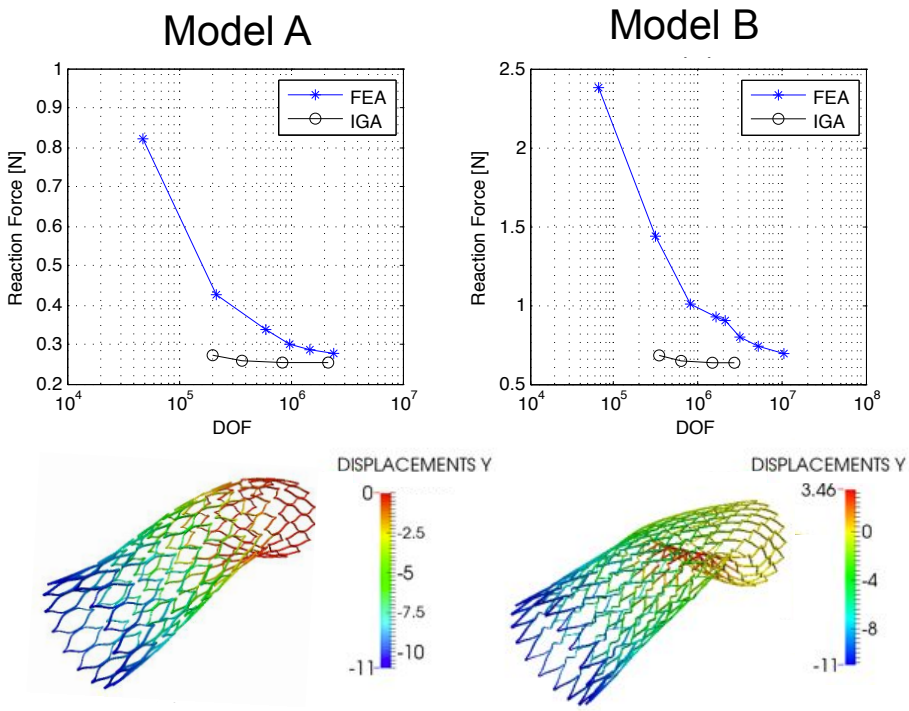

Figure 5.6 *Reaction force convergence plots (top) and contour plot of Y displacement in deformed configuration (bottom), in case of SMA constitutive model.*

suitability of a comparison based on reaction force prediction, we started with an elastic analysis comparing IgA and FEA, considering a global quantity given by the elastic stored energy. As depicted in Fig. 5.4 reaction force and deformation energy results show the same convergence trend and also the relative errors reported in Tables 6.2 and 5.2 show good agreement.

Given the results coming from the elastic analyses, we are confident that the reaction force is a suitable quantity to evaluate the global behavior of the models for both elastic and inelastic analyses. With this caveat the global performance of SMA stent Models A and B is presented in Fig.s 5.5 and 5.6 and in Tables 5.3 and 5.4). The results show that IgA again results in a better performance with respect to FEA on a per-degree-of-freedom basis, with a gain of over one order of magnitude in DOF number. This result is qualitatively in accordance with other theoretical results [17] and applicative examples [124]. In addition due to the higher degree and higher regularity of the NURBS basis functions the IgA yields low error also in its coarsest mesh IgA-1, i.e., the one coming directly from the CAD software.

As an example, we consider Model A (Fig. 5.6-*left* and Table 5.3) and we fix the DOF number in the range of $2 \cdot 10^5$, corresponding to the meshes IgA−1 and FEA−2, respectively. IgA shows a relative error of 6.57% with respect to the reference solution IgA−4, while FEA yields an error of 68.87%. We further note that the most refined FEA mesh, i.e., $2.5 \cdot 10^6$ DOF, still shows an error of 9%.

This trend is even more pronounced in results for Model B, where the closed cell design induces important local effects. In particular, in order to obtain a level of accuracy for FEA comparable to the coarsest IgA mesh (IgA−1), we need to resort to a extremely refined mesh, i.e., over 10^7 DOF.

As mentioned previously, we focus also on the influence of stent design with particular reference to kink formation and buckling phenomena ap-

pearing when a *closed-cell* stent is considered. Kink resistance is an important feature of stent devices [29]. When strains are locally increased beyond a critical value, buckling phenomena occur and the local bending stresses increase considerably. This phenomenon can be very dangerous for device performance, since it can lead to reduction of the fatigue life and implant failure. Kink formation is strongly related to stent design; in particular, *closed-cell* designs show less adaptability and are more prone to kinking with respect to *open-cell* designs. Our results confirm this statement and also are in accordance with experimental results [15]. Model A, classified as an *open-cell* stent, shows a smooth deformed configuration (Fig. 5.6-*left*). Instead, Model B, classified as a *closed-cell* stent, presents a kink in its deformed configuration (see Fig. 5.6-*right*). Even if buckling phenomena and kink formation in cardiovascular stents are commonly investigated, both from the experimental [15, 117] and the computational [119] point of view, our study is the first numerical study addressing the capability of IgA as well as traditional FEA to reproduce the buckling occurring in bent carotid artery stents.

Firstly, we investigate the capability of the two methods to reproduce, for a given level of accuracy, the same deformed configuration and buckling location. In particular, we consider the coarsest IgA mesh, i.e., IgA−1, and the finest FEA mesh, i.e., FEA−8 (Fig. 5.7). The "eyeball" norm confirms that the two models can reproduce the same buckling configuration.

Moving to the force-displacement diagrams, in Fig. 5.5 it is possible to observe that, while IgA presents the same deformation pattern for all considered refinements, FEA shows different behaviors with different refinements. In particular, the IgA deformation pattern shows two stages of local buckling (see Fig. 5.5-b). On the other hand, FEA is not able to capture this local behavior until a high number of degrees of freedom

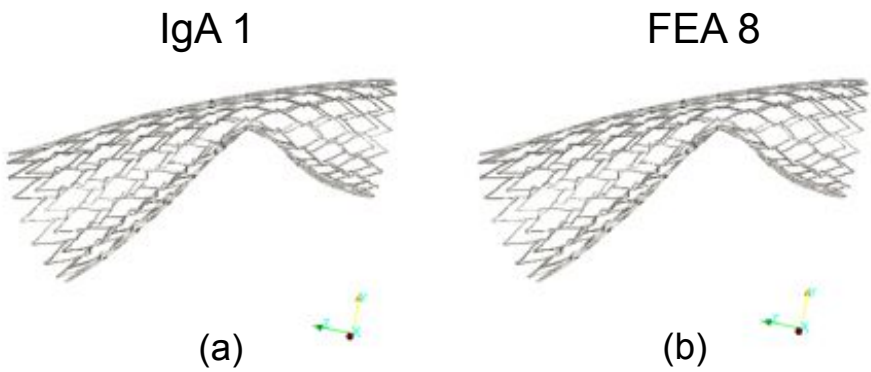

Figure 5.7 *Deformed configuration: Model B in case of SMA constitutive model; (a) IgA-1; (b) FEA-8 .*

is included (see Fig. 5.5-a). This phenomenon can be better appreciated in Fig. 5.5-c. In particular, it is important to observe that, while FEA refinements up to FEA−5 present only one stage of local buckling, FEA−6 recovers a deformation pattern similar to the IgA one. This aspect has a great influence in the capability of reproducing accurately the value of the critical load (see Tables 5.2 and 5.4).

These results demonstrate the capability of IgA to reproduce nonlinear local effects with a reduced DOF number with respect to classical FEA. It is remarkable to observe how low regularity and low interpolation order in the basis functions can lead to a reduced capability of catching the physics of the problem under investigation.

5.3.1 Computational times

Even though a fair efficiency comparison of IgA and FEA requires further investigations in terms of, for example, different approximation degrees for FEA and integration rules (see, as example, the work of [132]), it is interesting, from a practical viewpoint, to provide the computational times for a given level of accuracy, provided by the two models. In particular, the computational time coming from coarsest IgA mesh and the finest FEA mesh, are reported in Table 5.5. For Model A, given the meshes IgA-1 (relative error of 6.57%) and FEA-6 (relative error of 9.0%), IgA is 8.8 times faster than FEA. Within this model, both FEA and IgA are both performed with FEAP and 1 CPU. Moving to model B we consider the meshes IgA-1 (relative error of 8.98%) and FEA-8 (relative error of 9.57%). In this case, while the IgA simulation is still performed with FEAP and 1 CPU, the FEA simulation is performed with Abaqus/Standard with 8 CPUs in reason of the motivations mentioned in Section 5.2.3. However, it is interesting to remark that, from a qualitative point of view, IgA is still 3.9 times faster than FEA.

5.4 Summary

In the present study we developed a novel computational framework able to integrate CAD models and computational tools. These tools are then used to perform IgA for the evaluation of carotid artery stent performance.

Our results suggest that IgA is able to accurately represent the computational domain and also able to get better approximation of the solution with greatly reduced number of degrees of freedom with respect to traditional FEA. Moreover, when geometrical instabilities are present, IgA has the capability to accurately reproduce nonlinear local effects, such as local

buckling, even with quite coarse meshes.

This work, addressing the benefits of IgA for the simulation of complex biomedical devices, achieves the goal to demonstrate how IgA can provide different improvements over traditional FEA in terms of numerical results and engineering time. The present study can be the starting point for different investigations looking at the impact of IgA in different aspects of structural analysis applied to biomechanics, e.g., contact between endovascular devices and biological tissue. From the experimental point of view, future investigations will include coupling of flexibility test and micro-CT scans of the deformed configuration, and extension of this approach to a broader range of endovascular devices.

5.5 Tables

Mesh label	DOF	Order			Reaction force		Deformation energy	
		p	q	r	Value	Error	Value	Error
FEA-1	48,159	1	1	1	3.2656	233.19 %	14.323	246.52 %
FEA-2	220,725	1	1	1	1.6864	72.06 %	7.2444	75.28 %
FEA-3	606,276	1	1	1	1.3259	35.28 %	5.6647	37.06 %
FEA-4	985,680	1	1	1	1.1764	20.02 %	5.0223	21.51 %
FEA-5	1,485,900	1	1	1	1.1340	15.70 %	4.8403	17.11 %
FEA-6	2,473,875	1	1	1	1.0905	11.26 %	4.6410	12.29 %
IgA-1	204,525	3	2	2	1.0586	8.00 %	4.5207	9.38 %
IgA-2	368,100	3	2	2	1.0237	4.44 %	4.3513	5.28 %
IgA-3	838,350	3	2	2	0.9969	1.71 %	4.2154	1.99 %
IgA-4	2,173,020	3	2	2	0.9801	-	4.1330	-

Table 5.1 *Analysis of stent bending: Model A with Saint Venant-Kirchhoff material; the relative errors are evaluated with respect to the finest IgA simulation, labeled as IgA-4.*

Mesh label	DOF	Order			Reaction force		Deformation energy		Critical load	
		p	q	r	Value	Error	Value	Error		
FEA-1	66,960	1	1	1	11.5550	194.74 %	91.475	139.18 %	11.4750	128.34 %
FEA-2	316,197	1	1	1	7.2072	83.83 %	62.491	63.39 %	7.5945	51.12 %
FEA-3	606,276	1	1	1	6.0187	53.52 %	52.898	38.31 %	6.5840	31.01 %
FEA-4	1,635,960	1	1	1	5.4220	38.30 %	47.696	28.95 %	6.0022	19.43 %
FEA-5	2,118,096	1	1	1	5.2990	35.16 %	46.588	24.71 %	5.8694	16.79 %
FEA-6	3,246,480	1	1	1	5.1645	31.73 %	45.361	18.60 %	5.7059	13.54 %
IgA-1	346,413	3	3	2	4.4149	12.61 %	41.780	9.24 %	5.3836	7.12 %
IgA-2	648,000	3	3	2	4.1018	4.62 %	39.565	3.45 %	5.1518	2.51 %
IgA-3	1,530,546	3	3	2	3.9741	1.36 %	38.895	1.69 %	5.0873	1.23 %
IgA-4	2,700,435	3	3	2	3.9204	-	38.245	-	5.0254	-

Table 5.2 *Analysis of stent bending: Model B with Saint Venant-Kirchhoff material; the relative errors are evaluated with respect to the finest IgA simulation, labeled as IgA-4.*

Mesh label	DOF	Order			Reaction force	
		p	q	r	Value	Error
FEA-1	48,159	1	1	1	1.6769	224.11 %
FEA-2	220,725	1	1	1	0.9393	68.87 %
FEA-3	606,276	1	1	1	0.7370	32.56 %
FEA-4	985,680	1	1	1	0.6551	17.99 %
FEA-5	1,485,900	1	1	1	0.6319	13.81 %
FEA-6	2,473,875	1	1	1	0.0602	9 %
IgA-1	204,525	3	2	2	0.5878	6.57 %
IgA-2	368,100	3	2	2	0.5675	2.45 %
IgA-3	838,350	3	2	2	0.5249	0.22 %
IgA-4	2,173,020	3	2	2	0.5262	-

Table 5.3 *Analysis of stent bending: Model A with SMA material; the relative errors are evaluated with respect to the finest IgA simulation, labeled as IgA-4.*

Mesh label	DOF	Order			Reaction Force		Critical Load	
		p	q	r	Value	Error	Value	Error
FEA-1	66,960	1	1	1	2.3767	278 %	2.4074	165.88 %
FEA-2	316,197	1	1	1	1.4403	129.07 %	1.6395	81.07 %
FEA-3	606,276	1	1	1	1.0102	60.66%	1.3354	47.48 %
FEA-4	1,635,960	1	1	1	0.91935	46.21%	1.1671	28.9 %
FEA-5	2,118,096	1	1	1	0.89916	43 %	1.1300	24.8 %
FEA-6	3,246,480	1	1	1	0.79611	26.61 %	1.0754	18.77 %
FEA-7	5,281,740	1	1	1	0.73349	16.65 %	0.99991	10.43 %
FEA-8	10,622,016	1	1	1	0.68897	9.57 %	0.97022	7.25 %
IgA-1	346,413	3	3	2	0.68524	8.98 %	0.96182	6.22 %
IgA-2	648,000	3	3	2	0.64070	1.9%	0.92121	1.74 %
IgA-3	1,530,546	3	3	2	0.63018	0.22 %	0.90712	0.18 %
IgA-4	2,700,435	3	3	2	0.62875	-	0.90543	-

Table 5.4 *Analysis of stent bending: Model B with SMA material; the relative errors are evaluated with respect to the finest IgA simulation, labeled as IgA-4.*

	Mesh label	DOF	# CPU	Solver	Total analysis time
Model A	IgA-1	204,525	1	FEAP	**47 min**
	FEA-6	2,473,875	1	FEAP	**6 h 55 min**
Model B	IgA-1	346,413	1	FEAP	**6 h 41 min**
	FEA-8	10,622,016	8	Abaqus/Standard	**26 h 23 min**

Table 5.5 *Computational times for IgA and FEA.*

Chapter 6

IgA-based contact mechanics: from basics to real life applications

Contact boundary value problems are an household topic in computational mechanics. This statement is particularly evident in biomechanics problems, where an accurate and robust contact representation is fundamental to evaluate many important biomedical device features like, e.g., stent radial strength[1], or, more in general, to accurately simulate a wide variety of surgical procedures for pre-operative planning.

In this context, IgA can provide a reliable tool in reason of the exact representation of the contact surfaces and the higher regularity with respect to traditional FEA.

This chapter aims at introducing the basic concepts of contact mechanics and setting up an IgA-based computational framework to investigate the frictionless contact interaction between stent devices and deformable surfaces.

[1] Radial strength is defined as the stent capability to provide a sufficient radial support to the vascular vessel.

6.1 Contact problems in vascular biomechanics

Computational contact mechanics principles are widely employed in vascular biomechanics to numerically reproduce important experimental benchmarks and, more in general, to simulate the interaction between a cardiovascular device and a biological structure. In the following both applications are briefly described by means of two representative examples.

6.1.1 Radial strength evaluation

Post procedural restenosis is one of the principal causes of implant failure after CAS. As example, Lal et al. [133] performed a clinical investigation on 118 patients obtaining an incidence of in-stent recurrent restenosis of 6.4% (taking into account a vessel occlusion between 40% and 60%). Post implant restenosis is mainly caused by the acute vascular injuries induced by the percutaneous transluminal angioplasty (PTA) anticipating the stent implant. Such a damage can induce a cascade of physiological mechanisms to repair the vessel wall, leading to intima hyperplasia and vessel narrowing. Moreover, after CAS, the contact interaction between vessel and stent can be perceived by the organism as a foreign body, triggering an immune system response which can lead to further narrowing near or inside the stent. According to Lally et al. [10] the "optimal" carotid stent design in term of restenosis rate needs to present the following properties:

- High radial strength: this feature is required to prevent post-implant vessel recoil;
- Low artery-stent contact surface area: as introduced above, the contact interaction between stent and vessel can initiate an aggressive thrombotic response; The artery can react to the stent, perceive it as

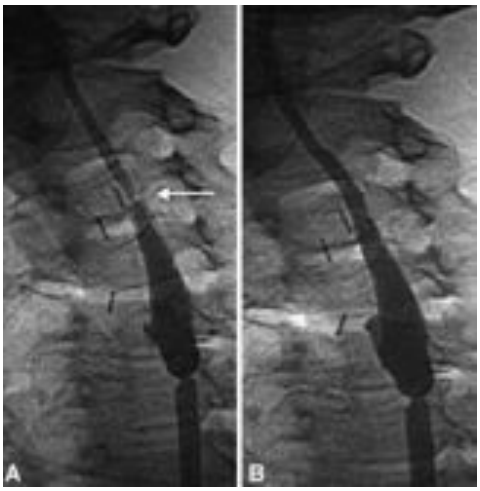

Figure 6.1 *A, Angiographic demonstration of focal in-stent restenosis developing at upper aspect of WallStent (arrow) 7 months after CAS. B, Treatment with angioplasty and placement of Palmaz stent produced a technically satisfactory angiographic result [11].*

a foreign body, and respond by mounting an immune system response which leads to further narrowing near or inside the stent.

Radial strength comparison between different stent designs has been widely experimentally investigated in the literature with different approaches [13, 14, 15, 134, 135, 136, 137, 138]. As example, Snowhill et al. [134] proposed an experimental benchmark to characterize the radial response of Z-shaped stent rings by mean of a polymeric strain gauge (Fig.6.2-a), while Schrader et al. [135] employed a more complex system based on a pressurized chamber and strain measures extrapolated by ultrasonic crystals (Fig. 6.2-b). It is clear that the experimental approach requires an accurate control in determining the boundary conditions of the problem and, often, this is too complex or, at worst, not possible. In this aspect, computational modeling

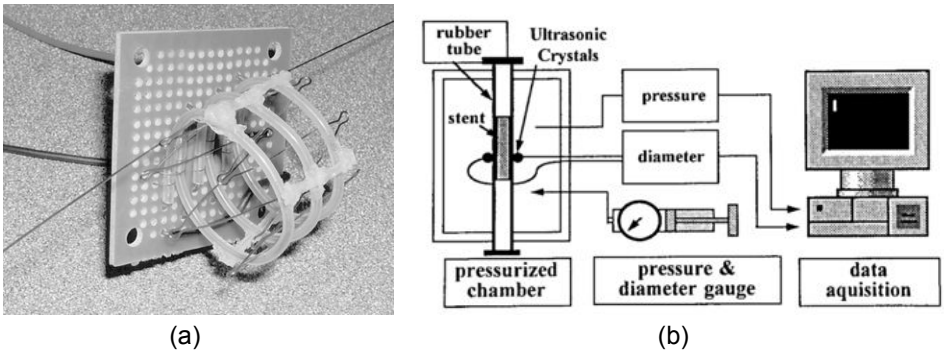

Figure 6.2 *Radial strength experimental benchmarks: (a) picture of a Whitney strain gauge with a z stent inserted into its center [134]; (b) pressure chamber and measurement set up for radial strength evaluation [135].*

can provide a valuable tool to predict the radial strength of a specific design. Again, the majority of such studies employ FEA in reason of its flexibility and capability to rapidly adapt to different designs, materials and working conditions [70, 77, 79, 139, 140, 141] . As example, Migliavacca et al. [139] proposed a 3D FEA model to investigate the effects of a radial pressure on different stent models (Fig. 6.3-a), while Dumoulin and Cochelin [141] investigated the impact of model complexities, e.g., 3D versus 2D models, in determining the effects of external pressure on stent devices (Fig. 6.3-b).

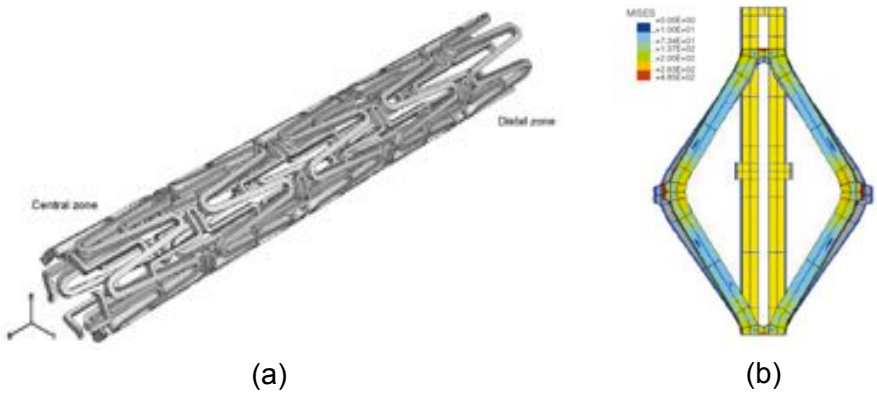

Figure 6.3 *Radial strength numerical benchmarks: (a) GEO-2 3D coronary stent model proposed in the work of Migliavacca et al. [139]; (b) Von Mises stress representation on a single cell deformed state after dilation at 12 mm diameter [141].*

6.1.2 Procedure-planning simulations

The contact between medical device and biological structure represents one of the most important sources of nonlinearity in structural biomechanics and the most important in terms of extrapolation of clinical relevant information for surgical pre-operative planning. In particular, the contact modeling plays a preeminent role in the following aspects:

- The contact stress induced by the stent implant in the vessel is a major index of injury (Fig. 6.4).

- The correct transmission of contact forces between vessel and stent determines the deformed configuration of the stent model. This information can be employed for further elaboration (see Chapter 3).

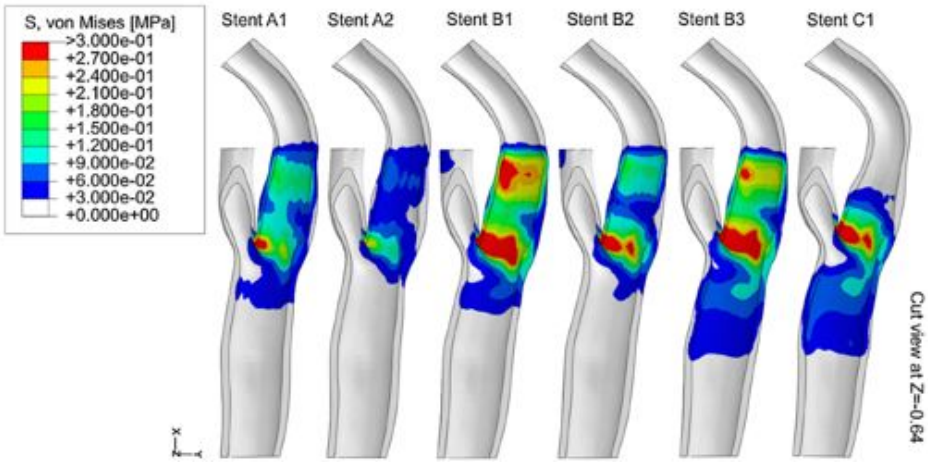

Figure 6.4 *Contour plot of von Mises stress distribution (S, von Mises) in the post-stenting carotid artery with respect to different stent models [142].*

In the following section the basics concepts of contact mechanics are introduced. Subsequently the change of paradigm from low-order, facet-based FEA contact formulation to the high-order, surface-based IgA contact formulation is presented.

6.2 Basic concepts of computational contact mechanics

The typical contact boundary value problem involves two deformable bodies undergoing finite deformations (Fig. 6.5). The most common approach identifies two basic entities, i.e., the *slave* body $\mathbf{B}^s$ and the *master* body $\mathbf{B}^m$. During deformation, if contact occurs, it is possible to identify the contact surface Γ_c. It is clear that this boundary value problem is inherently non-linear, since the contact condition introduces additional kinematic constraints to prevent the compenetration of the two bodies. The discrete counterpart of contact boundary value problems employed FEA for many years [143]. Along the boundary Γ_c of two bodies different contact models can be included. Within this doctoral research we focus on the simplest model, i.e., *frictionless* contact, in which the only non-zero component of the contact traction is normal to the contact surfaces.

The basic entities in computational contact mechanics are the contact pairs, i.e., couples of points (one for the slave body and one for the master body) where the contact constraint is locally enforced. The most common approaches to define the contact pairs are:

- Node-to-Node contact: Each contact pair is defined by a couple of mesh nodes, coming from the *slave* and *master* surfaces, respectively. This approach gives satisfactory results if the contact boundary displacements are small and the FEA meshes are constructed such that the nodes at the contact surfaces match;

- Node-to-Segment contact: Each contact pair is defined by a node coming from the *slave* surface and its projection on the *master* surface. In general the projection not necessarily coincides with a node (see Fig. 6.6).

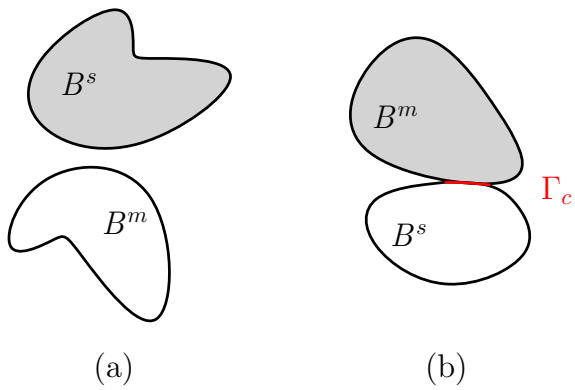

Figure 6.5 *2-D contact problem: (a) no contact; (b) contact state.*

Given the complex stent geometries objective of this chapter, it is not possible to ensure an adequate matching between master and slave discretizations. For this reason, in the following only the Node-to-Segment approach is considered. Once the pairs are established, the *gap* g determines which nodes are in contact. The entity g is defined as

$$g = [\mathbf{x}_s - \mathbf{x}_m] \cdot \mathbf{n}c \tag{6.2.1}$$

being $\mathbf{x}_s$ and $\mathbf{x}_m$ the slave node and master projection locations in the deformed configuration, and $\mathbf{n}_c$ the outward normal evaluated in the projection point. If $g > 0$ there is no contact, while if $g < 0$ compenetration occurs. Given the total energy of the system Π, a proper contact contribu-

tion Π_c needs to be included when contact occurs. Several techniques have been developed but we can roughly identify three big families:

- Lagrange multiplier form: The contact contribution is obtained multiplying the gap with the multiplier λ,

$$\Pi_c = \Pi(u, \lambda) = \int_{\Gamma_c} \lambda g \, d\Gamma, \tag{6.2.2}$$

  This approach implies that no compenetration occurs. The multiplier λ becomes an additional degree of freedom that must be included in the problem for each contact pair. From a physical viewpoint the lagrange multipliers can be associated with the contact force exchanged to avoid compenetration.

- Penalty function form: A simpler form with respect to Lagrange multiplier method considers the following form,

$$\Pi_c = \Pi(u) = \int_{\Gamma_c} \varepsilon g^2 \, d\Gamma, \tag{6.2.3}$$

  where ε is an user-defined penalty coefficient.
  In this case the final gap is not zero, so some compenetration occurs, depending on the parameter ε, i.e., high values of ε reduce the final gap. Thus, the main advantage of penalty method is that no additional degrees of freedom are required. The principal drawback is that there is no general rule to identify a proper value of ε. Moreover, extremely high values of ε lead to ill-conditioned problems;

- Augmented Lagrangian form: This form typically represents a good compromise between the previous two. In particular it uses an iterative update of the Lagrangian multiplier coupled with a penalty-like

form

$$\Pi_c = \Pi(u) = \int_{\Gamma_c} \lambda_k g + \varepsilon g^2 \, d\Gamma, \tag{6.2.4}$$

$$\lambda_{k+1} = \lambda_k + \varepsilon g(u), \tag{6.2.5}$$

Many augmentation strategies are available in literature in order to improve the convergence order of the method. However this approach allows to reach good solution quality with little additional effort.

6.2.1 Knot-to-segment contact formulation: toward an IgA-based approach

As described in the previous section, nowadays the most implemented technique for FEA contact problems is the node-to-segment (NTS) approach (Fig. 6.6). The use of non smooth, facet-based contact routines leads to

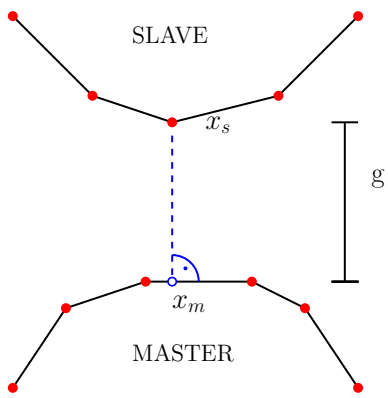

Figure 6.6 *Node-to-surface contact*

numerical problems in the geometric description of the contact surfaces and in the management of sliding contact. In particular, it may occur that the computation of the projection of the slave node to the master segment is

not unique (Fig. 6.7-a). Moreover, it is also possible that the projection is not unique and, at the same time, it is not located in the interior of the master segments (Fig. 6.7-b). These problems are strictly related to the C^0 continuity along the inter element FEA nodes and the lack of smoothness in the geometric description of the contact surface. For this reason, a discretization technique that guarantees higher order continuity along the elements is highly desirable. The research in the past years treated this issue with the development of smoothing techniques of the contact surfaces or with the exact description of the surfaces in the case of rigid obstacles. The principal drawbacks of these techniques are the lack of generality for arbitrary geometries in 3D problems and, in particular, the additional effort required to couple the smoothed surface with the real FEA mesh [144]. Given these considerations, it seems clear that IgA could provide and ideal

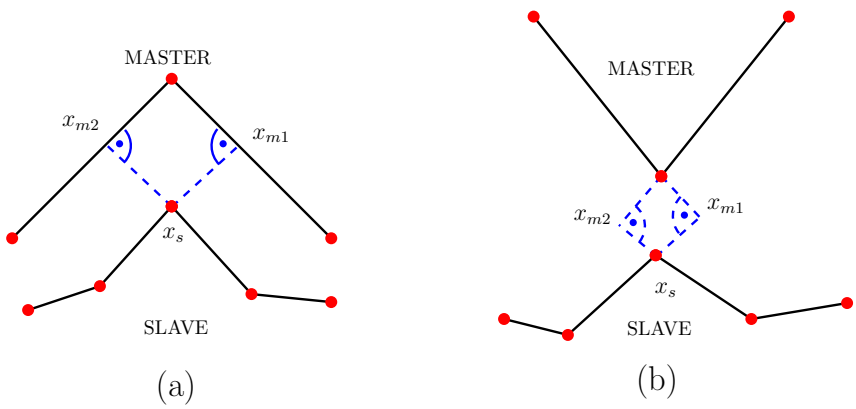

Figure 6.7 *Not uniqueness of the master projection: (a) two projections on the master side; (b) no projection on the master side.*

framework to overcome these issues in terms of surface smoothness. However, NTS approach cannot be naturally extended to IgA in reason given

the non-interpolatory nature of the control points. To overcome this limitation, Temizer et al. [105] proposed the so-called knot-to-segment (KTS) approach, in which the contact constraint is not imposed on the slave nodes, but at the Gauss points belonging to each slave contact surface (see Fig. 6.8). The first implementations of KTS algorithm showed superior quality

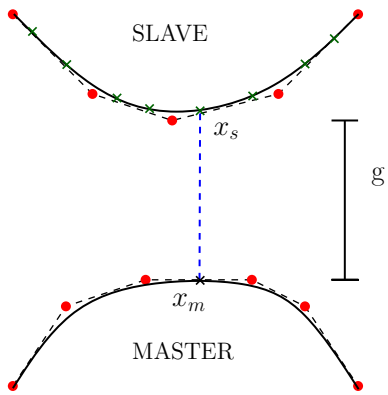

Figure 6.8 *Knot-to-segment contact: the gauss points on the slave surface are highlighted as* x

and robustness over classic Lagrangian elements. Temizer and colleagues pointed also out that the KTS implementation leads to an over-constrained problem induced by the discrepancy between the total number of degrees of freedom of the contact surfaces and the number of contact pairs, e.g. the number of Gauss points. Starting from this first step. the research took two different directions. On one hand, Temizer el al. [105] and De Lorenzis et al. [106] relaxed the over-costrained formulation implementing a mortar-based KTS approach, exhibiting superior results over classic KTS and NTS approach. On the other hand, Matzen et al. [145] proposed to collocate the contact constraint on particular points, e.g. Greville and Botella points, already implemented successfully in NURBS collocation methods [131]. The

use of Greville and Botella points gives a consistent number of collocation points with the control points along the contact surface.

6.3 NURBS 3D contact driver for FEAP

In this section the contact driver embedded within the IgA package for the general purpose solver FEAP is introduced. The contact driver reproduces the non-mortar KTS algorithm proposed by De Lorenzis et al. for NURBS discretizations [106] and by Dimitri et al. [146] for T-spline discretizations. In particular each portion of the contact driver and the add-ons included within this doctoral research are presented. The KTS contact driver structure is summarized in Fig. 6.9. The contact model is considered frictionless, i.e., only normal contact forces are transmitted. Initially, the contact constraint is regularized with a penalty method (more sophisticated solutions are implemented as add-ons). In the following, each block is described in detail.

6.3.1 Search

As introduced in the Section 6.2.1, for each slave Gauss point the contact pair is composed by the point itself and its unknown projection on the master surface. The projection point is recovered by means of a Newton-based scheme and the search routine aims at finding the best initial guess for the Newton loop. We assume that the projection is confined between all the elements connected to the closest master control point. This assumption allows to reduce the computational domain for the subsequent projection routine. This domain reduction has no general validity but, for reasonably refined meshes, we did not noticed any problem. In particular for each slave Gauss point $x_s(\xi)$, the parametric coordinates of the closest control point

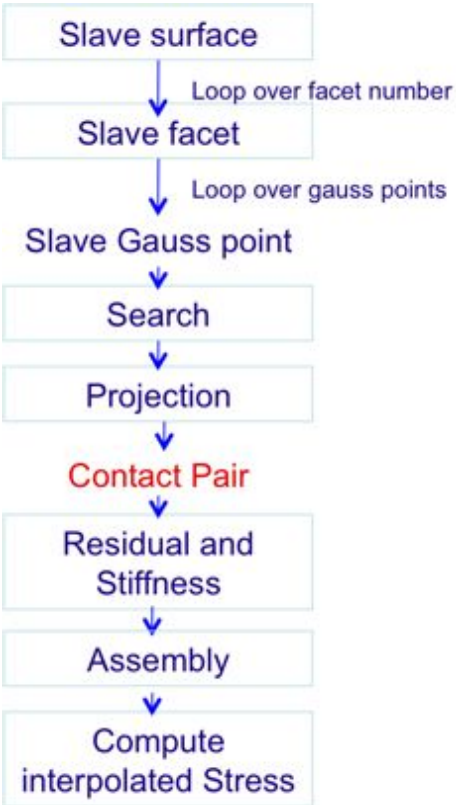

Figure 6.9 *KTS contact driver structure*

in the master side are stored. At the same time all the information concerning the facets connected with the closest control points are considered for projection in order to reduce the computational domain for the subsequent projection routine.

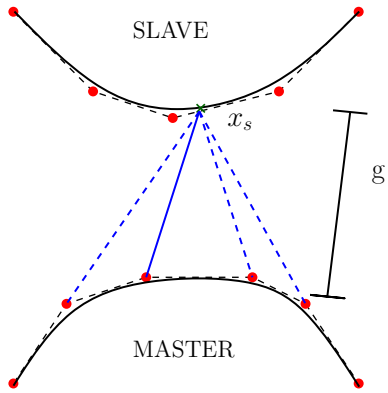

Figure 6.10 *Search algorithm: the gauss points on the slave surface are highlighted as $x.v$ The initial contact pair guess, prior to projection, is highlighted as the full blue line.*

6.3.2 Projection

The aim of the projection routine is to determine, for each slave Gauss point $x_s(\xi)$, the closest point projection $x_m(\xi)$ on the master surface. The projection point is recovered by means of a Newton-based scheme that minimizes the scalar product between the conjunction between $x_s(\xi)$ and $x_m(\xi)$, called $r(\xi)$, and the tangent vector $t(\xi)$ evaluated at the guess parametric coordinate. The search algorithm is summarized in box 1 and depicted in Fig. 6.11. The projection code is improved with the following add ons:

- The information about the facets connected with the initial guess is recovered to improve the projection. In particular when projection

BOX 1: CONTACT PROJECTION ALGORITHM

SET INITIAL GUESS ξ (SEARCH)

LOOP OVER MAX NUMBER OF ITERATIONS
    EVALUATE $\mathbf{x}_m(\xi)$
    COMPUTE $\mathbf{r}(\xi)$=$\mathbf{x}_m(\xi)$-$\mathbf{x}_s(\xi)$ and the Jacobian $\mathbf{J}(\mathbf{r})$
    COMPUTE $f(\xi)$=$\mathbf{r}(\xi)\cdot\mathbf{t}(\xi)$
    IF $f \leq tol$
        CONVERGENCE$\longrightarrow$ STORE PAIR INFORMATION
        BREAK
    ELSE
        $d\xi$=-$f(\xi)/J(\mathbf{r})$
        ξ=ξ+$d\xi$
NEXT

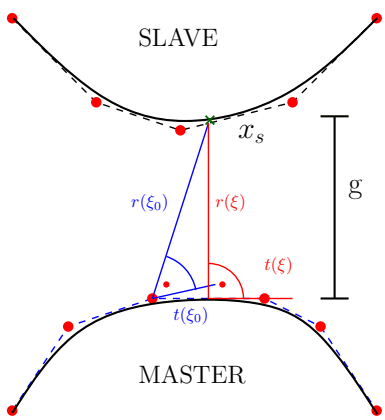

Figure 6.11 *Projection algorithm: initial and final configurations are depicted in blue and red, respectively.*

failure occurs in a facet, it is automatically switched to another stored facet;

- The increments $d\xi$ during the first iterations are scaled in order reduce the oscillation between facets if not necessary;

- The solution ξ at the ith is stored and employed as initial guess for the subsequent contact steps.

6.3.3 Residual, Stiffness and Assembly routines

Once we got the information about the contact pair, all the stiffness and residual contributions need to be computed and assembled into the global data structure. Both stiffness and residual computations follow the standard structure of penalty-based frictionless contact formulation [143]. The stiffness and residual contributions at the gauss point level are then projected and assembled at the degree of freedom level (the complete description of the data structures can be recovered in [146]).

In order to improve the accuracy and efficiency of the contact algorithm the following add-ons are implemented:

- The penalty constraint has been substituted with the augmented Uszawa algorithm [143]. In this way a sensitive increase of gap accuracy has been achieved with a little additional effort (see section 6.4.1).

- The driver data structure has been modified in order to use the FEAP contact assembly routine.

6.4 Numerical examples

In this section, the proposed IgA contact driver is tested by means of a set of simple numerical tests with increasing complexity. Subsequently, we move toward real-life applications including stent geometries, simplified artery models and inelastic constitutive models.

6.4.1 Preliminary tests

At first, we perform a simple benchmark in which FEA and IgA should attain the same results. In particular, a 3D, displacement-based, cube-cube contact test is implemented with trilinear shape functions both for FEA and IgA (see Fig. 6.12). Both tests employ a penalty-based regularization ($\varepsilon = 10^{12}$) and linear elastic constitutive models ($E = 10^4 MPa$ and $\nu = 0.3$). The IgA test employs the proposed KTS approach while the FEA one uses the FEAP built-in NTS driver. The results show perfect agreement both in terms of convergence rate and gap magnitude (see Table 6.1). The slight difference of computational times is due to the different implementation of FEA and IgA FEAP.

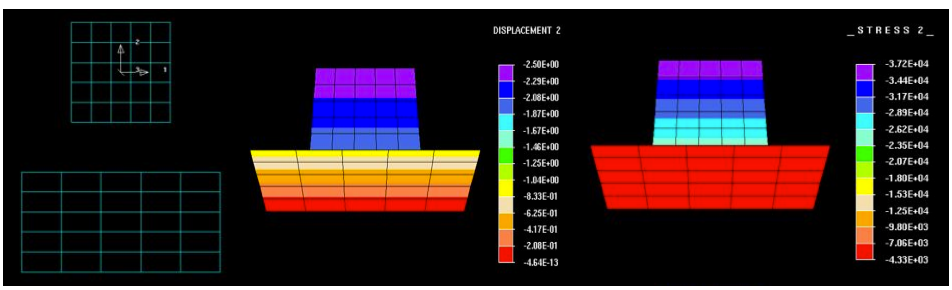

(a) (b) (c)

Figure 6.12 *3D Cube-Cube contact test: a) undeformed configuration; b) y-displacement contour plot; c)* σ_{yy} *contour plot*

In order to test the projection capability of the contact driver, other two tests are performed. They are both characterized by the need to project into a curved master surface. The first one is the so-called Cube-Cylinder contact test, in which the rigid slave cube body (discretized with a trilinear element) comes in contact with the master cylinder body (four quadratic-linear-linear elements) by means of a displacement-controlled analysis. In particular, the cube-cylinder contact is imposed both at internal knot location and tied boundary location, in order to address the capability of the contact driver to recover correctly all the data structures also after a node tie process. The results, depicted in Fig. 6.13, show that the contact driver is invariant to tied surfaces. Another test is the so called Cylinder-Cylinder contact test (both cylinders are discretized with 16 quadratic-quadratic-linear elements) , in which both master and slave surfaces are curved (see Fig. 6.14). This test mimics the expansion of a cylindric-shaped structure inside another one with the same topology, recalling the typical environment of simulations applied to vascular biomechanics. Moreover, this test investigates the improvements introduced by the implementation of the Uszawa algorithm ($\varepsilon = 10^3$, number of augmenting iterations = 3). In particular some results and computational indexes are compared with respect to the original penalty ($\varepsilon = 10^3$) formulation (see table 6.2). In particular, the employment of the Uszawa algorithm leads to a significant improvement of computational accuracy and gap magnitude with a slight increase

Model	IgA	FEA
Avg iteration number/step	2	2
Gap magnitude [mm]	10^{-5}	10^{-5}
CPU time [s]	0.56	0.34

Table 6.1 *Cube-cube test: IgA versus FEA.*

of iterations number and computational times.

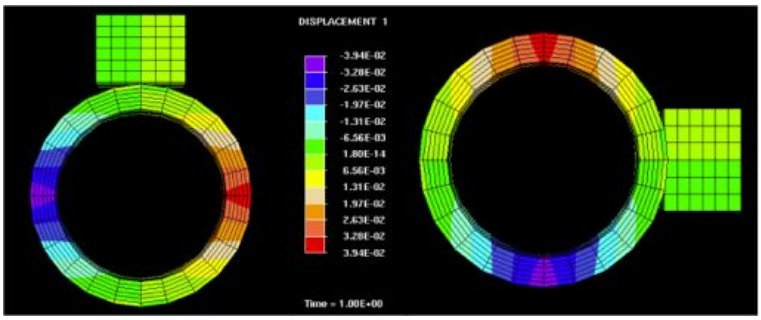

Figure 6.13 *Cube-Cylinder contact test: contour plot of the x-displacement. The plot is symmetrical respect to tied surfaces.*

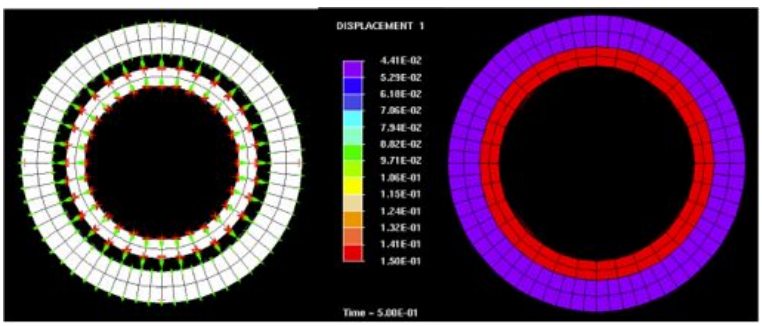

Figure 6.14 *Cylinder-Cylinder contact test: displacement vectors plot and radial displacement contour plot.*

Model	Penalty	Uszawa
Avg iteration number/step	3	7
Gap magnitude [mm]	10^{-5}	10^{-9}
CPU time [s]	33.16	73.64

Table 6.2 *Cylinder-Cylinder contact test: Penalty vs. Uszawa formulation*

6.4.2 Toward real-life applications

The ultimate goal of the present study is to provide an robust contact framework to evaluate the contact forces between a complex geometry, i.e., a stent and a deformable surface like a catheter or an artery, resorting to a reduced number of DOF. In this aspect, the objective of this section is to develop a multi-patch double-side contact driver (both cylinder-stent and stent-vessel) in order to get an innovative tool suitable for real life applications. In particular, we explored three illustrative examples applied to a carotid stent portion, i.e., expansion, crimping and deployment on a deformable pipe resembling a real carotid model.

Stent expansion and crimping simulations

The first test aims at simulating the expansion of a carotid stent ring. Stent expansion has a crucial role in determining the implant performance in coronary stenting but has no clinical application in carotid artery stenting. However, virtual expansion is often employed in the literature in order to obtain the expanded stent model when only information on the crimped stent is available [20, 67].

Concerning to stent crimping, it represents the step before stent deployment and activation of the contact between stent and vessel.

The stent models (Fig. 6.15-a and 6.16-a) are obtained with the same procedure described in Section 5.2.1. The stent resembles a portion of a Bard ViVEXX Carotid Stent (C. R. Bard Angiomed GmbH & Co., Germany), it is composed by 18 NURBS patches and it is modeled as a Neo-hookean material (E=15000 MPa, ν=0.3). The crimper is composed by one cylindrical NURBS patch and is modeled as a rigid body. The boundary conditions include displacement conditions on the crimper to impose the

radial expansion, and the minimal stent constraints to avoid rigid body motions. For the expansion simulation, the stent is expanded from its crimped configuration (radius equal to 0.6 mm) to its final expanded configuration (radius equal to 3.5 mm). For the crimping simulation, the stent undergoes under a 55% radius reduction. The contact constraint is regularized using the Uszawa algorithm ($\varepsilon = 10^3$, number of augmenting iterations = 3). The contour plots for the displacement and Von Mises stress solutions for the stent expansion simulation and stent crimping simulation are depicted in Fig. 6.15-b and c and in Fig. 6.16-b-c, respectively.

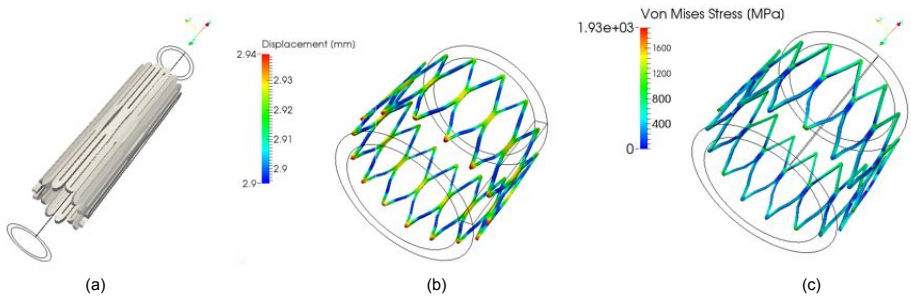

Figure 6.15 *Stent expansion test: (a) undeformed configuration; (b) radial displacement contour plot ; (c) Von Mises Stress contour plot.*

Stent deployment simulation

The last numerical test of this Chapter aims at investigating the interaction between a carotid stent (Fig. 6.17-b) and an idealize stenotic artery with a 25% lumen reduction (Fig. 6.17-a). As in many other works of our group, we perform a two-step simulation procedure [20, 68]. The first step corresponds to the crimping simulation described in the previous section, i.e., the diameter of the stent is decreased simulating the loading phase

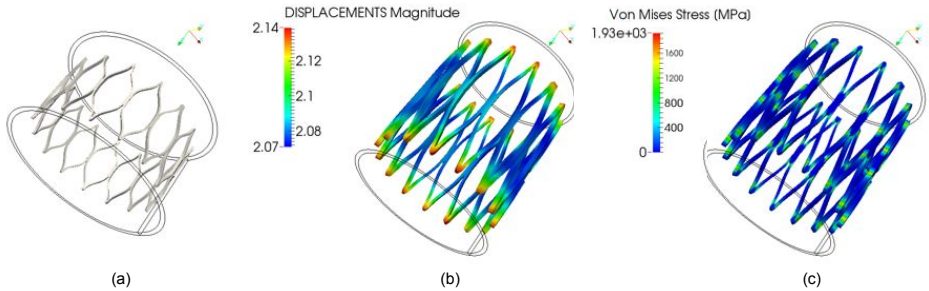

Figure 6.16 *Stent crimping test: (a) undeformed configuration; (b) radial displacement contour plot ; (c) Von Mises Stress contour plot.*

of the stent into the delivery system 6.17-c. Subsequently, the catheter expands again in order to place the stent into the target lesion 6.17-d. For this simulations we consider the Souza model presented in Chapter 2, using the same material parameters employed in Chapter 5, for the stent and a Neohookean model for the stenotic artery (E=1 MPa, ν=0.3). The contour plots of displacement and Von Mises distributions for both vessel and stent are depicted in Fig. 6.18. This preliminary analysis confirms the results obtained by Auricchio et al. [55].

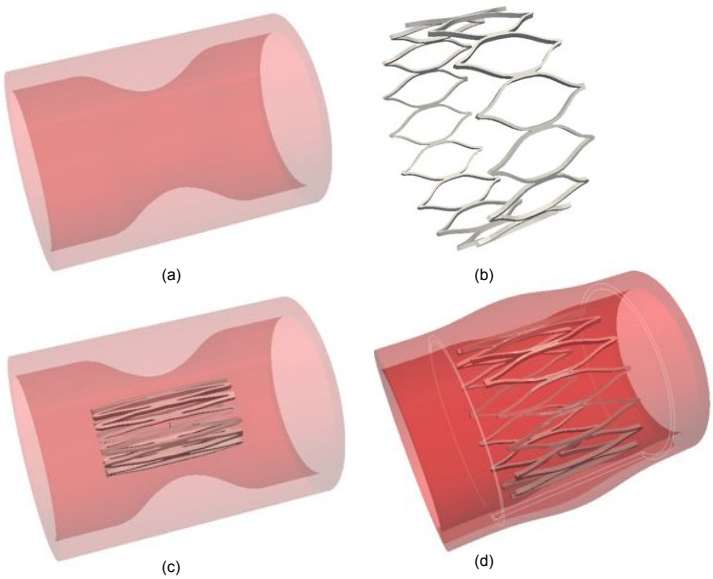

Figure 6.17 *Stent deploymend test: (a) vessel model; (b) stent model; (c) Deformed configuration after crimping; (d) Deformed configuration after deploymend.*

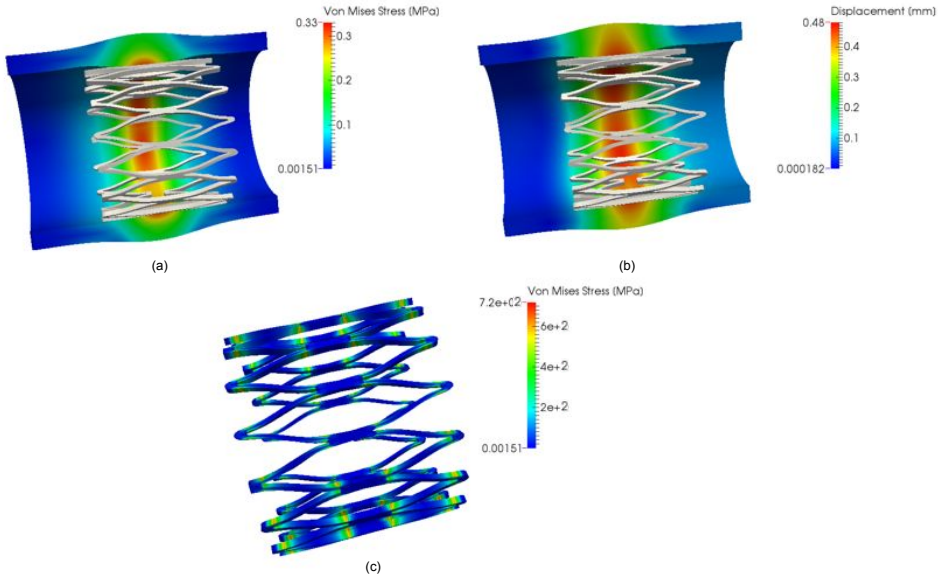

Figure 6.18 *Stent deploymend test: (a) Vessel Von Mises contour plot; (b) vessel radial displacement contour plot ; (c) stent Von Mises Stress contour plot.*

6.5 Summary

In the present study a novel IgA-based contact driver able to simulate complex contact interaction between stents and arterial vessel is presented and described. Our preliminary results suggest that KTS contact driver is able to represent the computational domain and also able to get reasonable results within a novel IgA framework. This is the first step to obtain a robust and accurate KTS contact driver to simulate real-life, clinical relevant implant simulations.

Chapter 7

Final remarks

Each piece, or part, of the whole of nature is always merely an approximation to the complete truth, or the complete truth so far as we know it. In fact, everything we know is only some kind of approximation, because we know that we do not know all the laws as yet. Therefore, things must be learned only to be unlearned again or, more likely, to be corrected.

The Feynman Lectures on Physics (1964)

In recent years, the employment of *in silico* (i.e., computational) methods in the medical device sector has become an important tool for both device manufacturers and clinical researchers.
From the industrial point of view, computational tools allow to investigate, prior to device manufacturing, different experimental scenarios including design modifications, new materials, and working conditions that are difficult to reproduce with the traditional experimental approach. Moreover,

numerical tools are employed, within the concept of predictive medicine, to simulate different "what-if" clinical scenarios with the aim of tailoring the best combination of medical device and procedure strategy for a specific patient morphology.

From a practical viewpoint, the reliable application of these methodologies in the industrial and clinical practice needs to fulfill the following requirements: i) reliable description of the material behavior of the involved components; ii) accurate geometric representation of the computational model with respect to the real component; iii) appropriate reproduction of the real working conditions within the computational model.

Within this context, Finite Element Analysis (FEA) is widely used as a reliable and accurate tool to develop the scopes described above. However, even if FEA is already a widely employed and well assessed simulation tool, it presents some limitations that can affect both the geometrical accuracy of the domain under investigation and the regularity of the approximated solution. In particular, the typical low-order and low-regularity FEA basis functions used to discretize the continuum domain do not allow, in general, to accurately represent complex geometries unless extremely fine meshes are adopted. At the same time, FEA basis functions do not allow, in general, to properly approximate the solution without resorting to a high number of degrees of freedom.

In this aspect, Isogeometric analysis (IgA), has been recently proposed as an exact-geometry, cost-effective alternative to classical FEA. The idea of IgA is that NURBS basis functions used for geometry representation in CAD can be employed both for the geometry description and the solution framework in a isoparametric fashion. This approach allows to bypass the meshing process and to merge the model for design and analysis into one. Moreover, the high regularity provided by the IgA shape functions extends

the benefits provided by this innovative method to all the boundary value problems where high continuity plays a preeminent role.

The doctoral research described in this dissertation is collocated within this framework, since we aimed at integrating advanced constitutive modeling and innovative computational mechanics techniques to efficiently evaluate the main mechanical features of different shape memory alloy (SMA) carotid stent designs. In particular, the present doctoral research can be subdivided as follows: i) identification and implementation of robust and accurate SMA constitutive models; ii) set up of a "traditional" FEA-based computational framework for the computation of carotid stent scaffolding; iii) set up of an innovative IgA-based computational framework for the evaluation of carotid stent flexibility; iv) performance comparison between IgA and FEA with respect to solution accuracy and computational efficiency; v) extension of the proposed IgA framework to take into account frictionless contact modeling for stent implant simulations.

Accordingly, we first investigated the peculiar issues and techniques related to SMA material constitutive modeling. In particular, we presented a brief overview of the SMA mechanical features we need to take in account for the applications object of this dissertation. Subsequently, we described the continuous model and the discrete implementation of two widely employed SMA constitutive models, i.e., Souza model [21] and Auricchio-Taylor model [22]. Thereafter, the two models were implemented and tested with several FEA-based SMA boundary value problems in order to confirm the effectiveness of such models into the description of complex mechanical behaviors typical of several real life applications. The results demonstrated that both models are able to accurately reproduce the main behavior of different boundary value problems with increasing complexity, e.g., large deformations and contact. Moreover, both models were not very effective

in a simulation involving constant loads and thermal cycles. We remark that this unexpected result is inherently related to the model structure for the Souza model, while it has not a clear explanation for the Auricchio-Taylor model, even if this aspect has been already investigated in the literature.

Following the reliable characterization of both SMA models, we moved toward the investigation of an important SMA carotid stent feature, i.e., vessel scaffolding, through patient-specific FEA. In particular, we measured the cell area of four different SMA stent designs deployed in a realistic carotid artery model. The results showed that, after the deployment, the cell area changes along the stent length in function of the vessel tapering. On one hand this result, widely expectable, demonstrates that the conclusions withdrawn from the free-expanded configuration appear to be qualitatively acceptable and our method is able to catch the same information. On the other hand, free-expanded cell area measures should be carefully handled since they do not take into account the variability affecting the cell area distribution after the implant. Our approach can be used as basis for comparative studies on the device behavior in implanted configurations, using different data, i.e. variability values, as index of critical behaviors, such as fish scaling effect, that can lead to intimal disruption and stenting implant fail. The results confirmed the capability of dedicated FEA simulations to provide useful information about complex stent features.

As previously introduced, FEA presents some drawbacks that can be overcome with the employment of innovative NURBS-based IgA. Thus, in order to investigate the IgA benefits over FEA within the objectives of this doctoral research, we implemented a novel computational framework based on IgA to evaluate another important SMA carotid stent feature, i.e., flexibility. We performed stent bending flexibility analyses involving large deformations using both IgA and classical FEA for two carotid artery

stent designs. The results suggested that, for a given level of accuracy, IgA attains a better performance with at least one order of magnitude fewer degrees of freedom than classical FEA. As a consequence, for the same level of accuracy, IgA showed a significant enhancement also for the computational times with respect to traditional FEA. These aspects are even more pronounced when we consider a particular design inducing local buckling effects. Moreover, it is remarkable to observe how low regularity and low interpolation order in FEA basis functions can lead to a reduced capability of catching the physics of the problem under investigation.

Eventually, given the promising results obtained with the IgA flexibility simulations, we aimed at extending the proposed IgA framework to include the contact modeling in order to numerically reproduce important experimental benchmarks, e.g., radial strength evaluation, or, more in general, to simulate the carotid stent implant for pre-operative planning. We focused on the application of NURBS-based isogeometric analysis to 3D frictionless contact problems between deformable bodies undergoing large deformations. In particular, starting from the works of De Lorenzis et al. [106, 146], we presented the knot-to-surface (KTS) contact driver implemented in the IgA package for FEAP. Moreover, for each driver portion, several add-ons were proposed in order to improve computational efficiency and robustness. Several basic numerical tests were implemented and the results showed that the proposed computational framework provides promising results with reduced DOF number with respect to classical FEA. Moreover, we extended the proposed framework to more complex applications, including stent geometry and non linear constitutive models to simulate the double-sided contact typical of stent implant simulations. The preliminary results demonstrated the capability of the proposed framework to reproduce complex real life problems.

7.1 Future developments

The results of our doctoral research proved the capability of computational modeling to efficiently reproduce a set of experimental benchmark to evaluate the mechanical behavior of endovascular stents.
From the computational viewpoint, we demonstrated the huge impact that IgA can provide within this topic, both in terms of geometrical representation and cost-effective accuracy. Our results can be the first step for several developments, both in terms of technological improvement and possible industrial applications. In the following, the main future developments for the present work are summarized.

- IgA computational efficiency: even if the IgA results showed an improved efficiency and accuracy with respect to linear FEA, it is important to remark the following aspects: (i) the current FEAP IgA package does not include parallel implementation; (ii) all performed IgA tests employed the classical FEA $p+1$ Gauss quadrature which is not the best solution, given the large support of NURBS shape functions (in this aspect several solutions have been investigated in the literature [84, 85] and need to be explored);

- Advanced NURBS mesh generation: the procedure proposed in Chapter 5 (and extended to vascular structures in Appendix B) provides accurate models from a geometric point of view. However, the majority of CAD models employ boolean operators and/or trimming techniques to build arbitrary topologies bypassing the NURBS tensor product nature. Unfortunately, these approaches keep the original NURBS parametrization unchanged, leading to a discrepancy between the CAD model and the IgA-suitable NURBS structure. In

this aspect, the research is moving in two main directions: (i) different technologies to perform IgA using trimmed surfaces are under development [147, 148]; (ii) novel parametrizations, e.g., T-splines [109, 110], hierarchical B-splines [111] and LR- B-splines [112], can overcome the tensor product limitation;

- From research to industrial design: the results of this doctoral research, coupled with the technological improvements mentioned in the previous point provide a promising framework for different applications. As example, the three stent mechanical tests, i.e., vessel scaffolding, flexibility and radial strength could be integrated within a simplified CAD software to rapidly prototype new stent designs (Fig. 7.1).

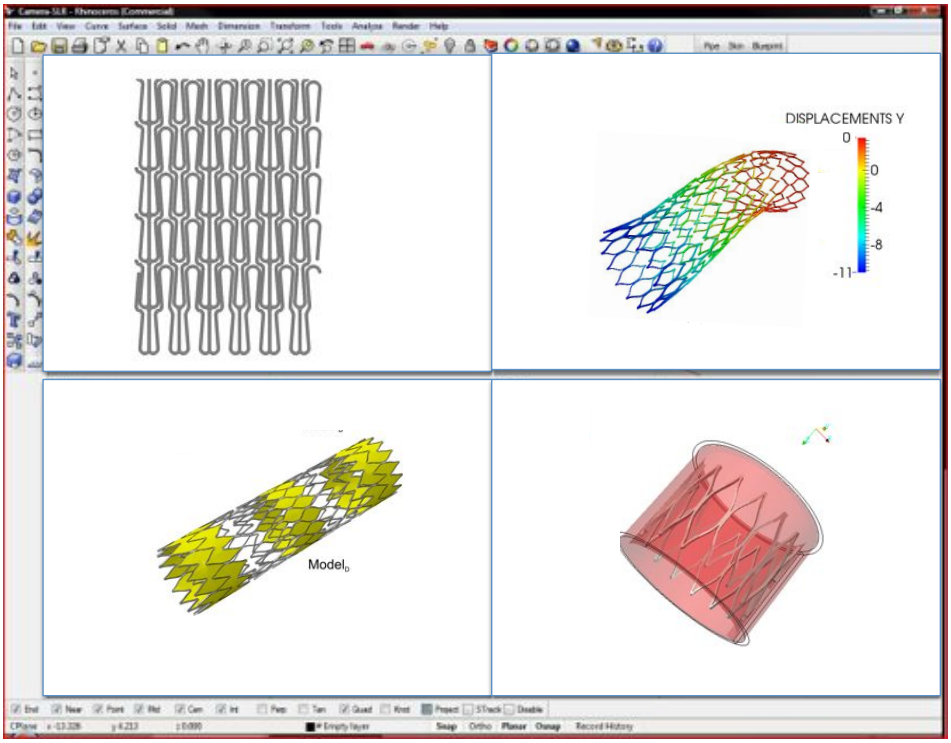

Figure 7.1 *Future developments: integrated CAD-IgA software for stent design evaluation.*

Appendix A

Abaqus/Standard solution control parameters

Solution control parameters can be used to control:

- nonlinear equation solution accuracy;
- time increment adjustment;

These solution control parameters need not be changed for most analyses. In difficult cases, however, the solution procedure may not converge with the default controls or may use an excessive number of increments and iterations. After it has been established that such problems are not due to modeling errors, it may be useful to change certain control parameters. Control parameters can modify different aspect of FEA and, for our analyses, we chose to include control modifications on time incrementation parameters. Solution control parameters can be used to alter both the convergence control algorithm and the time incrementation scheme. The time incrementation parameters and are the most significant since they have a direct effect on convergence. They may have to be modified if convergence is

(initially) nonmonotonic or if convergence is nonquadratic. Nonmonotonic convergence may occur if various nonlinearities interact; for example, the combination of friction, nonlinear material behavior, and geometric nonlinearity may lead to nonmonotonically decreasing residuals. Nonquadratic convergence will occur if the Jacobian is not exact, which may occur for complex material models. We implemented time incrementation controls with the following syntax:

```
*CONTROLS, PARAMETERS=TIME INCREMENTATION
** Relax checks on rate of convergence:
**   IO   IR   IP   IC   IL   IG  IS  IA
**   16 , 18 , 20 , 40 , 30 ,  6, 12, 20
```

where

- I_O number of equilibrium iterations (without severe discontinuities) after which the check is made whether the residuals are increasing in two consecutive iterations;

- I_R number of consecutive equilibrium iterations (without severe discontinutities) at which logarithmic rate of convergence check begins;

- I_P number of consecutive equilibrium iterations (without severe discontinuities) after which the residual tolerance R_P is used instead of R_N;

- I_C upper limit on the number of consecutive equilibrium iterations (without severe discontinuities), based on prediction of the logarithmic rate of convergence;

- I_L number of consecutive equilibrium iterations (without severe discontinuities) above which the size of the next increment will be reduced;
- I_G maximum number of consecutive equilibrium iterations (without severe discontinuities) allowed in consecutive increments for the time increment to be increased;
- I_S maximum number of severe discontinuity iterations allowed in an increment;
- $I_A$maximum number of cutbacks allowed for an increment;

For a detailed description of the *CONTROLS command see [149].

Appendix B

NURBS-based surface mapping for vascular biomechanics

B.1 Problem definition

CVD are the main cause of death in western countries and it is responsible for hundreds of thousands of early deaths all over the world. CVD are not only a major threat to individuals' lives and their quality of life but it is also a major economic cost to all European countries [1]. Several treatment options are nowadays available for managing many CVD but, thanks also to the encouraging outcomes achieved in the coronary district, the application of percutaneous minimally-invasive techniques, such as stenting, grafting and angioplasty procedure, are also applied to other peripheral districts. Device design, development and performance assessment of these minimally-invasive procedures are the natural application field of computational biomechanics, which applies the principle of mechanics to investigate biological systems and their interaction with artificial implants. In particular, patient-specific modeling has been proposed in recent years as a

new paradigm in surgical planning support based on computational tools [121, 150, 151].
Moreover, Isogeometric Analysis (IgA) has recently emerged as a cost-effective alternative to classic isoparametric Finite Element Analysis (FEA) [17]. The main feature of the method consists of using typical CAD basis functions for both geometric description and variable approximation. This implies the ability to describe exactly the computational domain geometry throughout the analysis process, including, at the same time, the chance to control the basis functions continuity. These features led to a wide variety of approaches able to treat efficiently many critical aspects of FEA (e.g., analysis of nearly incompressibile solids and novel contact formulations [95, 106]). Starting from these results, the aim of this work is to create a computational workflow able to convert the information coming from vascular patient-specific DICOM images into a IgA-suitable geometric structure and to perform a preliminary analysis resembling a minimal-invasive procedure i.e., carotid angioplasty, using an an extension of FEAP, a numerical solver widely adopted for research in FEA, to IgA [125].

B.2 Materials and Methods

The main objective of this work is to provide, given the vascular medical images, a geometrical structure IgA-suitable. This task can be achieved through the following steps:

- Image processing: the set of DICOM medical images need to be processed in order to get a finite number of point able to describe the vascular surface;

- Mapping: starting from a given NURBS parametrization (primitive surface) and the set of points previously extracted (reference surface), a least-square based mapping procedure is implemented in order to obtain two patient-specific NURBS surfaces, resembling the inner and outer vascular wall, respectively;

- FEAP-suitable block structure: the two NURBS surface need to be integrated in order to obtain a 3D IgA solid structure suitable for the solver FEAP;

The proposed framework includes all the other ingredients needed by IgA (boundary conditions, material definition) and, as a preliminary analysis, a displacement-control simulation of angioplasty procedure has been performed.

B.2.1 Image processing

The vessel model considered in this study reflects the geometry of a patient-specific carotid artery, derived from DICOM images of a neck-head Computed Tomography Angiography (see Fig.B.1-a). After a segmentation step (Fig. B.1-b), the vascular surface was splitted into its main branches (Fig. B.1-c) using the vascular model toolkit VMTK. The final pre-processing step consist on the skeletonization of the surfaces and the subsequent points extraction (Fig. B.1-d). These points represent the reference surface for the subsequent mapping procedure.

B.2.2 Mapping procedure

In order to obtain a IgA-suitable NURBS structure starting from a set of points representing the vascular geometry, we implemented the mapping

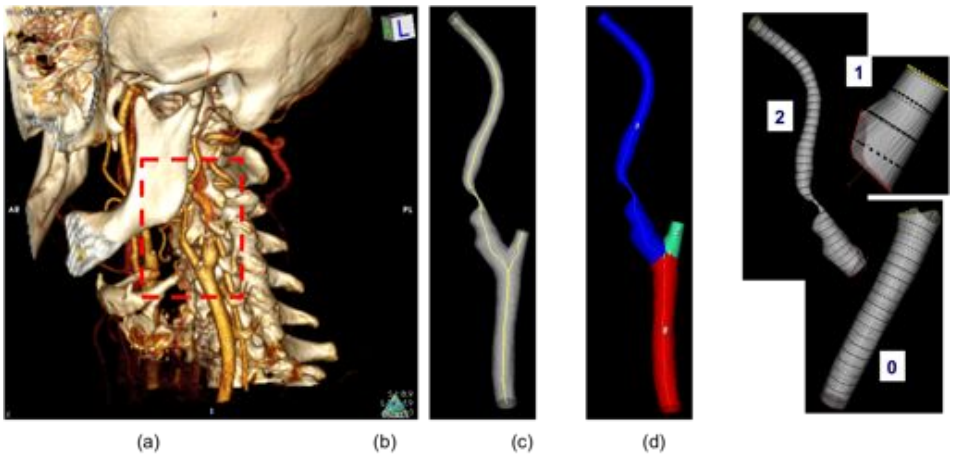

Figure B.1 *Image processing step: 3D volumetric reconstruction from CTA images (a); vascular STL surface and centerline (b); vascular surfaces after branch splitting (c); sampled sections after skeletonization process (d).*

procedure proposed by Morganti [124], that has been successfully applied to aortic root geometries. A generic NURBS surface defined in $\mathbb{R}^3$ can be described with the following relation:

$$\mathbf{S}(\psi,\eta) = \frac{\sum_i \sum_j N_{i,p}(\psi) M_{j,q}(\eta) \mathbf{B}_{ij} w_{ij}}{\sum_i \sum_j N_{i,p}(\psi) M_{j,q}(\eta) w_{ij}} \tag{B.2.1}$$

where $\mathbf{B}_{ij}$ and w_{ij} represent the i,j-th control point coordinates and weight, respectively, and $N_{j,q}$ and $M_{i,p}$ are the i-th j-th shape functions of order p and q respectively, related to each parametric direction. Assuming constant weights, after some simple algebraic manipulations, eq.B.2.1 can be rearranged in order to get the following matricial form

$$\mathbf{S_T}^{\mathbf{r}} = \mathbf{C} * \mathbf{B}^{\mathbf{r}}{}_{vec} \tag{B.2.2}$$

where $\mathbf{S_T}^{\mathbf{r}}$ represents the r-th cartesian nodal component of the sampling points belonging to the reference surface, $\mathbf{B^r}_{vec}$ is the r-th cartesian component of the control points ordere in vectorial form and $\mathbf{C}$ roughly contains the products between shape functions values in both parametric directions. It is immediate to observe that eq.B.2.2 represents a linear system which can be solved (in the least-square sense) in order to obtain the r-th component of the mapped control points.
The proposed approach can be used to map a primitive cylinder with a predefined parametrization onto each of the carotid artery branch (Fig. B.2).

B.2.3 IgA structure and preliminary analysis

After the mapping procedure, the three NURBS patches, one for each vessel branch, need to be refined and integrated in a single vessel geometry, defined by 3D solid elements. This task is achieved by means of an in-house Matlab code (The Mathworks Inc., Natick, MA, USA) that includes a refinement step, both h and p, and several routines for the management of some critical geometrical aspects, as the interpach continuity at the bifurcation level. In the last part of the code the NURBS structure is exported in a format compatible with the isogeometric package for FEAP. The Matlab code takes advantage of the routines given by the NURBS toolbox and by some customized routines from the software tool GeoPDEs [152]. As preliminary analysis, a simulated angioplasty (AP) procedure for the carotid artery has been performed. From the clinical perspective AP is defined as the technique of mechanically widening narrowed or obstructed arteries, typically being a result of atherosclerosis. This task is achieved by mean of a ballon

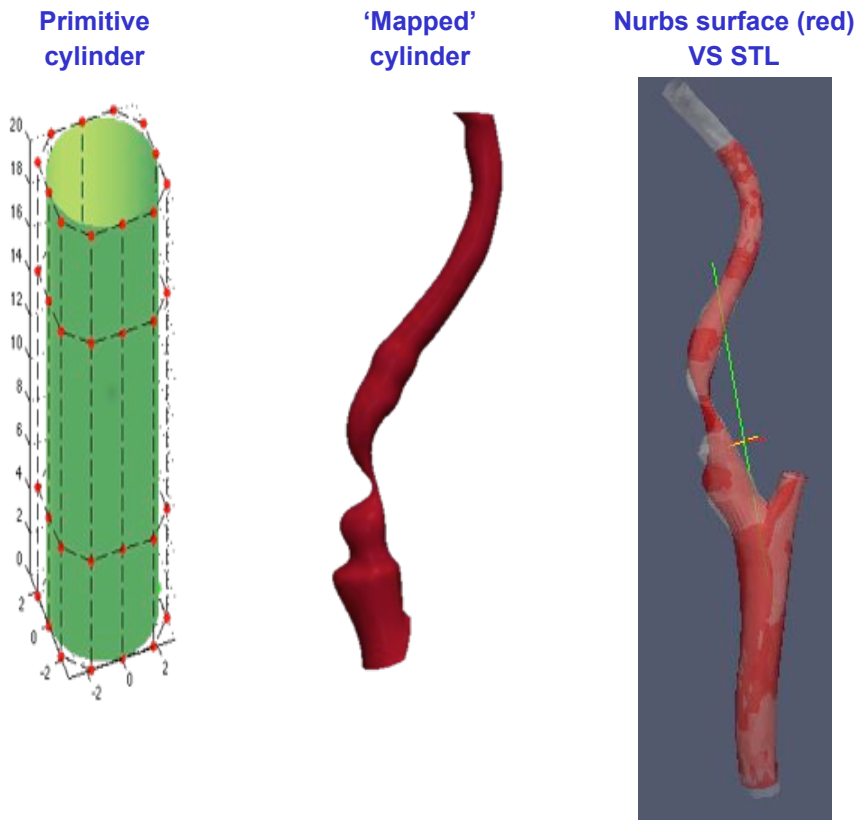

Figure B.2 *IgA mapping procedure: left primitive surface and parametrization; center mapped internal carotid IgA surface; right overlap of the IgA vascular surface with the original stl file.*

catheter that is passed into the narrowed location and then inflated to a fixed size and subsequently deflated and withdrawn. From the computational viewpoint AP can be roughly simplified as a displacement-controlled analysis with a finite-strain regime and (non)linear elastic constitutive behavior associated with the vessel model. The mechanical response of the vessel is reproduced assuming a Neohookean hyperelastic material model, defined by the two parameters E=2 MPa and ν=0.45. The ballon expansion is simulated by mean of a displacement field applied to the vessel inner wall control points. The displacement values were structured as the difference between the expected configuration and the reference configuration

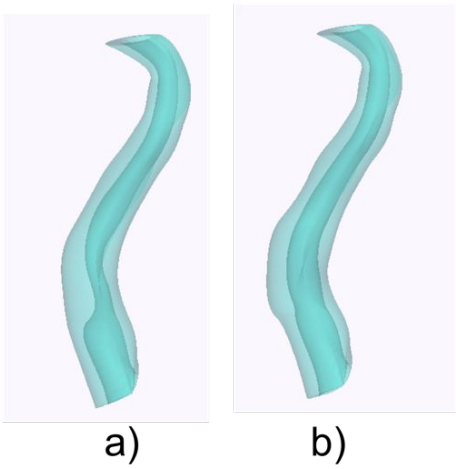

Figure B.3 *Ballon expansion simulation (one branch example): reference NURBS structure (a); expanded NURBS structure (b).*

B.3 Results and discussion

The von Mises stress distribution after the AP simulation is depicted in Fig. B.4. The results show, in a simplified way, the interaction between the expanded balloon and the vessel wall, exhibiting higher stress values in the stenotic region. This information, after a necessary refinement of the model features, can be associated with different clinical issues, such as vessel damage after AP and restenosis risk. It is important to note that this simulation was performed using only 3600 degrees of freedom, at least one order of magnitude less than typical FEA meshes for similar purposes [121, 150] . However, in order to ensure a fair comparison between FEA and IgA and to get a valuable tool for different cardiovascular applications, i.e., stenting and endografting, some more sophisticated tools, such as stable contact driver and complex constitutive models, need to be included.

B.4 Conclusions

In the present study we present a novel computational framework able to integrate medical information and computational tools in order to perform IgA for vascular biomechanics. The results suggest that it is possible to obtain an IgA-suitable structure in a reasonable number of steps. Moreover, a preliminary analysis has been performed in order to make the point about the capability of the workflow to reproduce, in a simplified way, a minimally-invasive procedure present in the clinical practice. In order to obtain a valuable tool for a wider range of clinical procedures, such as stenting and grafting, some more sophisticated components (such as stable contact driver,pressure elements, biologic materials constitutive models etc.) need to be included. We think that IgA for vascular biomechanics represents

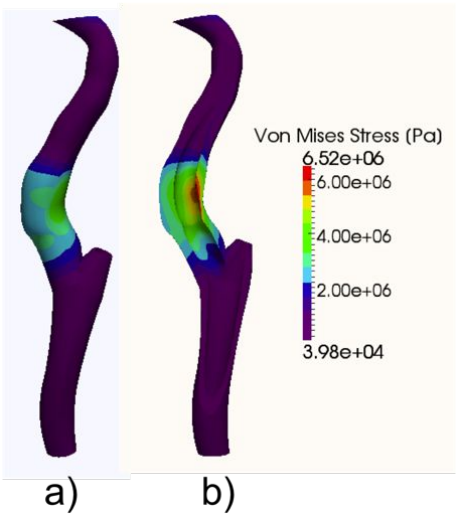

Figure B.4 *von Mises stress distribution of the ballon expansion simulation: complete vessel structure (a); clipped structure in order to visualize the stress at the lumen level (b).*

a big challenge both from computational and model design viewpoint and can give, in the next future, a crucial contribution to the integration of medicine and numerical analysis.

Bibliography

[1] M. Nichols, N. Townsend, R. Luengo-Fernandez, J. Leal, A. Gray, P. Scarborough, and M. Rayner, "European cardiovascular disease statistics 2012," *European Heart Network, Brussels, European Society of Cardiology, Sophia Antipolis*, p. P104, 2012.

[2] H. H. G. Eastcott, G. W. Pickering, and C. G. Rob, "Reconstruction of internal carotid artery in a patient with intermittent attacks of hemiplegia," *The Lancet*, vol. 264, no. 6846, pp. 994–996, 1954.

[3] NASCET trial collaborators, "Beneficial effect of carotid endarterectomy in symptomatic patients with high-grade carotid stenosis," *New England Journal of Medicine*, vol. 325, pp. 445–453, 1991.

[4] B. Farrell, A. Fraser, P. Sandercock, J. Slattery, and C. Warlow, "Randomised trial of endarterectomy for recently symptomatic carotid stenosis: final results of the mrc european carotid surgery trial (ecst)," *Lancet*, vol. 351, no. 9113, pp. 1379–1387, 1998.

[5] J. E. Connolly, "The epic 1954 operation that led to one of surgery's major advances: carotid endarterectomy," *Grand Rounds*, vol. 4, pp. L15–L17, 2004.

[6] T. Duerig and A. Pelton, "An overview of superelastic stent design," *Materials Science Forum Vols.*, pp. 1–8, 2002.

[7] M. Roffi and K. Mathias, "History of carotid artery stenting.," *The Journal of cardiovascular surgery*, vol. 54, no. 1, pp. 1–10, 2013.

[8] T. G. Brott, R. W. Hobson, G. Howard, G. S. Roubin, W. M. Clark, W. Brooks, A. Mackey, M. D. Hill, P. P. Leimgruber, A. J. Sheffet, *et al.*, "Stenting versus endarterectomy for treatment of carotid-artery stenosis," *New England Journal of Medicine*, vol. 363, no. 1, pp. 11–23, 2010.

[9] B. K. Lal, "Recurrent carotid stenosis after cea and cas: diagnosis and management," in *Seminars in vascular surgery*, vol. 20, pp. 259–266, Elsevier, 2007.

[10] C. Lally, D. Kelly, and P. Prendergast, "Stents," *Wiley Encyclopedia of Biomedical Engineering*, 2006.

[11] E. Y. Chakhtoura, R. W. Hobson II, J. Goldstein, G. T. Simonian, B. K. Lal, P. B. Haser, M. B. Silva Jr, F. T. Padberg Jr, P. J. Pappas, and Z. Jamil, "In-stent restenosis after carotid angioplasty-stenting: incidence and management," *Journal of vascular surgery*, vol. 33, no. 2, pp. 220–226, 2001.

[12] G. J. Tearney, E. Regar, T. Akasaka, T. Adriaenssens, P. Barlis, H. G. Bezerra, B. Bouma, N. Bruining, J.-m. Cho, S. Chowdhary, *et al.*, "Consensus standards for acquisition, measurement, and reporting of intravascular optical coherence tomography studiesa report from the international working group for intravascular optical coherence to-

mography standardization and validation," *Journal of the American College of Cardiology*, vol. 59, no. 12, pp. 1058–1072, 2012.

[13] S. H. Duda, J. Wiskirchen, G. Tepe, M. Bitzer, T. W. Kaulich, D. Stoeckel, and C. D. Claussen, "Physical properties of endovascular stents: an experimental comparison," *Journal of vascular and interventional radiology*, vol. 11, no. 5, pp. 645–654, 2000.

[14] J. F. Dyet, W. G. Watts, D. F. Ettles, and A. A. Nicholson, "Mechanical properties of metallic stents: how do these properties influence the choice of stent for specific lesions?," *Cardiovascular and interventional radiology*, vol. 23, no. 1, pp. 47–54, 2000.

[15] S. Müller-Hülsbeck, P. Schafer, N. Charalambous, S. Schaffner, M. Heller, and T. Jahnke, "Comparison of carotid stents: an in-vitro experiment focusing on stent design," *Journal of Endovascular Therapy*, vol. 16, pp. 168–177, 2009.

[16] C. A. Taylor and C. Figueroa, "Patient-specific modeling of cardiovascular mechanics," *Annual review of biomedical engineering*, vol. 11, pp. 109–134, 2009.

[17] T. Hughes, J. Cottrell, and Y. Bazilevs, "Isogeometric analysis: Cad, finite elements, nurbs, exact geometry, and mesh refinement," *Computer Methods in Applied Mechanics and Engineering*, vol. 194, pp. 4135–4195, 2005.

[18] J. Cottrell, T. Hughes, and Y. Bazilevs, *Isogeometric Analysis. Toward integration of CAD and FEA*. John Wiley & Sons, 2009.

[19] J. Grogan, S. Leen, and P. McHugh, "Comparing coronary stent material performance on a common geometric platform through simu-

lated bench testing," *Journal of the Mechanical Behavior of Biomedical Materials*, vol. 6, pp. 129–138, 2012.

[20] M. Conti, D. Van Loo, F. Auricchio, M. De Beule, G. De Santis, B. Verhegghe, S. Pirrelli, and A. Odero, "Impact of carotid stent cell design on vessel scaffolding: a case study comparing experimental investigation and numerical simulations," *Journal of Endovascular Therapy*, p. in press, 2011.

[21] A. Souza, E. Mamiya, and N. Zouain, "Three-dimensional model for solids undergoing stress-induced phase transformations," *European Journal of Mechanics, A: Solids*, vol. 17, pp. 789–806, 1998.

[22] F. Auricchio and R. L. Taylor, "Shape-memory alloys: modelling and numerical simulations of the finite-strain superelastic behavior," *Computer methods in applied mechanics and engineering*, vol. 143, no. 1, pp. 175–194, 1997.

[23] F. Auricchio, R. L. Taylor, and J. Lubliner, "Shape-memory alloys: macromodelling and numerical simulations of the superelastic behavior," *Computer methods in applied mechanics and engineering*, vol. 146, no. 3, pp. 281–312, 1997.

[24] M. V. Gandhi and B. S. Thompson, *Smart materials and structures*. Springer, 1992.

[25] T. W. Duerig, K. Melton, D. Stockel, and C. Wayman, "Engineering aspects of shape memory alloys," *Butterworth-Heinemann, Reed Books Services Ltd, P. O. Box 5, Rushden, Northants, NN 10 9 YX, UK, 1990. 499*, 1990.

[26] W. J. Buehler, J. V. Gilfrich, and R. C. Wiley, "Effect low temperature phase changes on the mechanical properties of alloys near composition ti-ni," *Journal of Applied Physics*, vol. 34, pp. 1475–1477, 2006.

[27] F. Auricchio and L. Petrini, "A three-dimensional model describing stress-temperature induced solid phase transformations. part i: solution algorithm and boundary value problems," *International Journal for Numerical Methods in Engineering*, vol. 4, pp. 807–836, 2004.

[28] T. Duerig, A. Pelton, and D. Stockel, "An overview of nitinol medical applications," *Materials Science and Engineering*, vol. A273-275, pp. 149–160, 1999.

[29] D. Stoeckel, "Nitinol medical devices and implants.," *Minimally Invasive Therapy & Allied Technologies*, vol. 9, pp. 81–88, 2000.

[30] S. A. Shabalovskaya, "Surface, corrosion and biocompatibility aspects of nitinol as an implant material," *Bio-medical materials and engineering*, vol. 12, no. 1, pp. 69–109, 2002.

[31] J. Ryhänen, E. Niemi, W. Serlo, E. Niemelä, P. Sandvik, H. Pernu, and T. Salo, "Biocompatibility of nickel-titanium shape memory metal and its corrosion behavior in human cell cultures," *Journal of biomedical materials research*, vol. 35, no. 4, pp. 451–457, 1997.

[32] A. Pelton, V. Schroeder, M. Mitchell, X. Gong, M. Barney, and S. Robertson, "Fatigue and durability of nitinol stents," *Fatigue and durability of Nitinol stents*, vol. 1, pp. 153–164, 2008.

[33] L. Petrini and F. Migliavacca, "Biomedical applications of shape memory alloys," *Journal of Metallurgy*, vol. 2011, 2011.

[34] N. Morgan, "Medical shape memory alloy applications—the market and its products," *Materials Science and Engineering: A*, vol. 378, no. 1, pp. 16–23, 2004.

[35] S. Idelsohn, J. Pena, D. Lacroix, J. Planell, F. Gil, and A. Arcas, "Continuous mandibular distraction osteogenesis using superelastic shape memory alloy (sma)," *Journal of Materials Science: Materials in Medicine*, vol. 15, no. 4, pp. 541–546, 2004.

[36] L. Machado and M. Savi, "Medical applications of shape memory alloys," *Brazilian Journal of Medical and Biological Research*, vol. 36, no. 6, pp. 683–691, 2003.

[37] K. Otsuka and C. M. Wayman, *Shape memory materials*. Cambridge university press, 1999.

[38] J. Arghavani, "Thermo-mechanical behavior of shape memory alloys under multi axial loadings; constitutive modeling and numerical implementation at small and finite strains.," *Phd Thesis in Mechanical Engineering, Sharif University of Technology, Tehran, Iran*.

[39] D. Hartl and D. Lagoudas, *Thermomechanical characterization of shape memory alloy materials*. Springer, 2008.

[40] M. E. Gurtin, *An introduction to continuum mechanics*. Academic press, 1982.

[41] J. Simo and T. Hughes, "Computational inelasticity," 2008.

[42] F. Falk and P. Konopka, "Three-dimensional landau theory describing the martensitic phase transformation of shape-memory alloys," *Journal of Physics: Condensed Matter*, vol. 2, no. 1, p. 61, 1990.

[43] Y. Huo, "A mathematical model for the hysteresis in shape memory alloys," *Continuum Mechanics and Thermodynamics*, vol. 1, no. 4, pp. 283–303, 1989.

[44] K. Tanaka and S. Nagaki, "A thermomechanical description of materials with internal variables in the process of phase transitions," *Ingenieur-Archiv*, vol. 51, no. 5, pp. 287–299, 1982.

[45] J. G. Boyd and D. C. Lagoudas, "Thermomechanical response of shape memory composites," *Journal of intelligent material systems and structures*, vol. 5, no. 3, pp. 333–346, 1994.

[46] L. Brinson, "One-dimensional constitutive behavior of shape memory alloys: thermomechanical derivation with non-constant material functions and redefined martensite internal variable," *Journal of intelligent material systems and structures*, vol. 4, no. 2, pp. 229–242, 1993.

[47] B. Raniecki, C. Lexcellent, and K. Tanaka, "Thermodynamic models of pseudoelastic behaviour of shape memory alloys," *Archiv of Mechanics, Archiwum Mechaniki Stosowanej*, vol. 44, pp. 261–284, 1992.

[48] S. Leclercq and C. Lexcellent, "A general macroscopic description of the thermomechanical behavior of shape memory alloys," *Journal of the Mechanics and Physics of Solids*, vol. 44, no. 6, pp. 953–980, 1996.

[49] J. Lubliner and F. Auricchio, "Generalized plasticity and shape memory alloys," *International Journal of Solids and Structures*, vol. 33, no. 7, pp. 991–1003, 1996.

[50] J. Lubliner, *Plasticity theory.* Courier Dover Publications, 2008.

[51] M. Qidwai and D. Lagoudas, "On thermomechanics and transformation surfaces of polycrystalline niti shape memory alloy material," *International Journal of Plasticity*, vol. 16, no. 10, pp. 1309–1343, 2000.

[52] L. Orgeas and D. Favier, "Non-symmetric tension-compression behaviour of niti alloy," *Journal de physique. IV*, vol. 5, no. 8, pp. C8–605, 1995.

[53] G. Maenchen and S. Sack, "The tensor code," tech. rep., California. Univ., Livermore. Lawrence Radiation Lab., 1963.

[54] F. Auricchio, A. Coda, A. Reali, and M. Urbano, "Sma numerical modeling versus experimental results: parameter identification and model prediction capabilities," *Journal of materials engineering and performance*, vol. 18, no. 5-6, pp. 649–654, 2009.

[55] F. Auricchio, M. Conti, S. Morganti, and A. Reali, "Shape memory alloy: from constitutive modeling to finite element analysis of stent deployment," *Computer Modeling in Engineering and Sciences (CMES)*, vol. 57, no. 3, p. 225, 2010.

[56] D. Hartl, S. Oehler, and D. Lagoudas, "Constitutive modeling of phase transformation and plastic yield in smas: Application to the s3t-roundrobin," in *ESOMAT 2009-8th European Symposium on Martensitic Transformations*, p. 08006, EDP Sciences, 2009.

[57] P. Sittner, L. Heller, J. Pilch, P. Sedlak, M. Frost, Y. Chemisky, A. Duval, B. Piotrowski, T. B. Zineb, E. Patoor, *et al.*, "Roundrobin

sma modeling," in *ESOMAT 2009-8th European Symposium on Martensitic Transformations*, p. 08001, EDP Sciences, 2009.

[58] R. Mirzaeifar, R. DesRoches, and A. Yavari, "A combined analytical, numerical, and experimental study of shape-memory-alloy helical springs," *International Journal of Solids and Structures*, vol. 48, no. 3, pp. 611–624, 2011.

[59] F. Auricchio, G. Scalet, and M. Urbano, "A numerical/experimental study of nitinol actuator springs," *Journal of Materials Engineering and Performance*, pp. 1–9, 2014.

[60] P. Zhu, L. C. Brinson, E. Peraza-Hernandez, D. Hartl, and A. Stebner, "Comparison of three-dimensional shape memory alloy constitutive models: Finite element analysis of actuation and superelastic responses of a shape memory alloy tube," in *ASME 2013 Conference on Smart Materials, Adaptive Structures and Intelligent Systems*, pp. V002T02A004–V002T02A004, American Society of Mechanical Engineers, 2013.

[61] A. Cremonesi, C. Setacci, F. Castriota, and M. Valgimigli, "Carotid stent cell design: lack of benefit or lack of evidence?," *Stroke*, vol. 39, p. e130, 2009.

[62] C. Setacci, G. de Donato, and M. Bosiers, "Two different studies on carotid stent cell design importance, or are we just saying the same thing?," *Stroke*, vol. 39, p. e129, 2008.

[63] M. Schillinger, M. Gschwendtner, B. Reimers, J. Trenkler, L. Stockx, J. Mair, S. Macdonald, F. Karnel, K. Huber, and E. Minar, "Does carotid stent cell design matter?," *Stroke*, vol. 39, pp. 905–909, 2008.

[64] M. Bosiers, G. de Donato, K. Deloose, J. Verbist, P. Peeters, F. Castriota, A. Cremonesi, and C. Setacci, "Does Free Cell Area Influence the Outcome in Carotid Artery Stenting?," *European Journal of Vascular and Endovascular Surgery*, vol. 33, pp. 135–141, 2007.

[65] J. Hart, P. Peeters, J. Verbist, K. Deloose, and M. Bosiers, "Do device characteristics impact outcome in carotid artery stenting?," *J of Vascular Surgery*, vol. 44, pp. 725–730, 2006.

[66] J. Hart, M. Bosiers, K. Deloose, R. Uflacker, and C. Schönholz, "Impact of stent design on the outcome of intervention for carotid bifurcation stenosis," *The Journal of Cardiovascular Surgery*, vol. 51, pp. 799–806, 2010.

[67] M. Conti, F. Auricchio, M. De Beule, and B. Verhegghe, "Numerical simulation of Nitinol peripheral stents: from laser-cutting to deployment in a patient specific anatomy," *Proceeding of ESOMAT 2009*, p. 06008, 2009.

[68] F. Auricchio, M. Conti, M. De Beule, G. De Santis, and B. Verhegghe, "Carotid artery stenting simulation: from patient-specific images to finite element analysis," *Medical Engineering & Physics*, vol. 33, pp. 281–289, 2011.

[69] N. Rebelo, N. Walker, and H. Foadian, "Simulation of implantable stents," *Abaqus User's Conference*, vol. 143, pp. 421–434, 2001.

[70] C. Kleinstreuer, Z. Li, C. Basciano, S. Seelecke, and M. Farber, "Computational mechanics of Nitinol stent grafts," *Journal of Biomechanics*, vol. 41, pp. 2370–2378, 2008.

[71] M. Cremonesi, A. Frangi, and U. Perego, "A lagrangian finite element approach for the analysis of fluid-structure interaction problems," *International Journal for Numerical Methods in Engineering*, vol. 84, no. 5, pp. 610–630, 2010.

[72] A. Cremonesi, P. Rubino, C. Grattoni, D. Scheinert, F. Castriota, and G. Biamino, "Multicenter experience with a new hybrid carotid stent," *Journal of Endovascular Therapy*, vol. 15, pp. 186–192, 2008.

[73] M. Bosiers, K. Deloose, J. Verbist, and P. Peeters, "What Practical Factors Guide the Choice of Stent and Protection Device during Carotid Angioplasty?," *European Journal of Vascular and Endovascular Surgery*, vol. 35, pp. 637–643, 2008.

[74] G. Siewiorek, M. Wholey, and E. Finol, "In vitro performance assessment of distal protection filters: Pulsatile flow conditions," *Journal of Endovascular Therapy*, vol. 16, pp. 735–743, 2009.

[75] M. Wholey and E. Finol, "Designing the Ideal Stent," *Endovascular Today*, vol. 6, pp. 25–34, 2007.

[76] P. Mortier, G. Holzapfel, M. De Beule, D. Van Loo, Y. Taeymans, P. Segers, P. Verdonck, and B. Verhegghe, "A novel simulation strategy for stent insertion and deployment in curved coronary bifurcations: comparison of three drug-eluting stents," *Annals of Biomedical Engineering*, vol. 38, pp. 88–99, 2010.

[77] W. Wu, M. Qi, X. Liu, D. Yang, and W. Wang, "Delivery and release of nitinol stent in carotid artery and their interactions: A finite element analysis," *Journal of Biomechanics*, vol. 40, pp. 3034–3040, 2007.

[78] D. Gastaldi, S. Morlacchi, R. Nichetti, C. Capelli, G. Dubini, L. Petrini, and F. Migliavacca, "Modelling of the provisional side-branch stenting approach for the treatment of atherosclerotic coronary bifurcations: effects of stent positioning," *Biomechanics and Modeling in Mechanobiology*, vol. 9, no. 5, pp. 551–561, 2010.

[79] C. Lally, F. Dolan, and P. Prendergast, "Cardiovascular Stent Design and Vessel Stresses: a Finite Element Analysis," *Journal of Biomechanics*, vol. 38, pp. 1574–1581, 2005.

[80] G. Holzapfel, M. Stadler, and T. Gasser, "Changes in the mechanical environment of the stenotic arteries during interaction with stents: Computational assessment of parametric stent design," *Journal of Biomechanical Engineering*, vol. 127, pp. 166–180, 2005.

[81] J. Gillard, M. Graves, T. Hatsukami, and C. Yuan, *Carotid Disease, The Role of Imaging in Diagnosis and Management.* Cambridge University Press, 2007.

[82] L. Piegl and W. Tiller, *The NURBS book.* Springer, 2007.

[83] J. Zhu, R. Taylor, and O. Zienkiewicz, "The finite element method: Its basis and fundamentals," 2005.

[84] T. J. Hughes, A. Reali, and G. Sangalli, "Efficient quadrature for nurbs-based isogeometric analysis," *Computer methods in applied mechanics and engineering*, vol. 199, no. 5, pp. 301–313, 2010.

[85] F. Auricchio, F. Calabro, T. Hughes, A. Reali, and G. Sangalli, "A simple algorithm for obtaining nearly optimal quadrature rules for nurbs-based isogeometric analysis," *Computer Methods in Applied Mechanics and Engineering*, vol. 249, pp. 15–27, 2012.

[86] Y. Bazilevs, L. Beirao da Veiga, J. Cottrell, T. Hughes, and G. Sangalli, "Isogeometric analysis: approximation, stability and error estimates for h-refined meshes," *Mathematical Models and Methods in Applied Sciences*, vol. 16, no. 07, pp. 1031–1090, 2006.

[87] J. Cottrell, A. Reali, Y. Bazilevs, and T. Hughes, "Isogeometric analysis of structural vibrations," *Computer Methods in Applied Mechanics and Engineering*, vol. 38, pp. 310–322, 2006.

[88] J. Cottrell, A. Reali, and T. Hughes, "Studies of refinement and continuity in isogeometric structural analysis," *Computer Methods in Applied Mechanics and Engineering*, vol. 196, pp. 41–44, 2007.

[89] A. Reali, "An isogeometric analysis approach for the study of structural vibrations," *Journal of Earthquake Engineering*, vol. 10, pp. 1–30, 2006.

[90] J. Kiendl, K.-U. Bletzinger, J. Linhard, and R. Wüchner, "Isogeometric shell analysis with kirchhoff–love elements," *Computer Methods in Applied Mechanics and Engineering*, vol. 198, no. 49, pp. 3902–3914, 2009.

[91] D. Benson, Y. Bazilevs, M. Hsu, and T. Hughes, "Isogeometric shell analysis: the reissner–mindlin shell," *Computer Methods in Applied Mechanics and Engineering*, vol. 199, no. 5, pp. 276–289, 2010.

[92] A. Buffa, G. Sangalli, and R. Vázquez, "Isogeometric analysis in electromagnetics: B-splines approximation," *Computer Methods in Applied Mechanics and Engineering*, vol. 199, no. 17, pp. 1143–1152, 2010.

[93] H. Gómez, V. M. Calo, Y. Bazilevs, and T. J. Hughes, "Isogeometric analysis of the cahn–hilliard phase-field model," *Computer Methods in Applied Mechanics and Engineering*, vol. 197, no. 49, pp. 4333–4352, 2008.

[94] G. Vilanova, I. Colominas, and H. Gomez, "Capillary networks in tumor angiogenesis: From discrete endothelial cells to phase-field averaged descriptions via isogeometric analysis," *International journal for numerical methods in biomedical engineering*, vol. 29, no. 10, pp. 1015–1037, 2013.

[95] R. Taylor, "Isogeometric analysis of nearly incompressible solids," *International Journal for Numerical Methods in Engineering*, vol. 87, pp. 273–288, 2011.

[96] T. Elguedj, Y. Bazilevs, V. M. Calo, and T. J. Hughes, "and projection methods for nearly incompressible linear and non-linear elasticity and plasticity using higher-order nurbs elements," *Computer methods in applied mechanics and engineering*, vol. 197, no. 33, pp. 2732–2762, 2008.

[97] J. M. Kiendl, *Isogeometric analysis and shape optimal design of shell structures*. Shaker, 2011.

[98] W. A. Wall, M. A. Frenzel, and C. Cyron, "Isogeometric structural shape optimization," *Computer methods in applied mechanics and engineering*, vol. 197, no. 33, pp. 2976–2988, 2008.

[99] S. Cho and S.-H. Ha, "Isogeometric shape design optimization: exact geometry and enhanced sensitivity," *Structural and Multidisciplinary Optimization*, vol. 38, no. 1, pp. 53–70, 2009.

[100] Y. Bazilevs, V. Calo, J. Cottrell, T. Hughes, A. Reali, and G. Scovazzi, "Variational multiscale residual-based turbulence modeling for large eddy simulation of incompressible flows," *Computer Methods in Applied Mechanics and Engineering*, vol. 197, pp. 173–201, 2007.

[101] Y. Bazilevs, J. Gohean, R. Moser, Y. Zhang, and T. Hughes, "Patient-specific isogeometric fluid-structure interaction analysis of thoracic aortic blood flow due to implantation of the jarvik 2000 left ventricular assist device," *Computer Methods in Applied Mechanics and Engineering*, vol. 198, pp. 3534–3550, 2009.

[102] Y. Bazilevs, Y. Zhang, V. Calo, S. Goswami, C. Bajaj, and T. Hughes, "Isogeometric fluid–structure interaction analysis with applications to arterial blood flow," *Computational Mechanics*, vol. 199, pp. 229–263, 2010.

[103] F. Auricchio, L. B. Da Veiga, T. Hughes, A. Reali, and G. Sangalli, "Isogeometric collocation methods," *Mathematical Models and Methods in Applied Sciences*, vol. 20, no. 11, pp. 2075–2107, 2010.

[104] F. Auricchio, L. Beirão da Veiga, T. Hughes, A. Reali, and G. Sangalli, "Isogeometric collocation for elastostatics and explicit dynamics," *Computer methods in applied mechanics and engineering*, vol. 249, pp. 2–14, 2012.

[105] I. Temizer, P. Wriggers, and T. Hughes, "Contact treatment in isogeometric analysis with nurbs," *Computer Methods in Applied Mechanics and Engineering*, vol. 200, no. 9, pp. 1100–1112, 2011.

[106] L. De Lorenzis, I. Temizer, P. Wriggers, and G. Zavarise, "A large deformation frictional contact formulation using nurbs-based isoge-

ometric analysis," *International Journal for Numerical Methods in Engineering*, vol. 87, no. 13, pp. 1278–1300, 2011.

[107] S. Lipton, J. A. Evans, Y. Bazilevs, T. Elguedj, and T. J. Hughes, "Robustness of isogeometric structural discretizations under severe mesh distortion," *Computer Methods in Applied Mechanics and Engineering*, vol. 199, no. 5, pp. 357–373, 2010.

[108] T. Hughes, A. Reali, and G. Sangalli, "Duality and unified analysis of discrete approximations in structural dynamics and wave propagation: Comparison of p-method finite elements with k-method nurbs.," *Computer Methods in Applied Mechanics and Engineering*, vol. 197, pp. 4104–4124, 2008.

[109] Y. Bazilevs, V. M. Calo, J. A. Cottrell, J. A. Evans, T. Hughes, S. Lipton, M. Scott, and T. Sederberg, "Isogeometric analysis using t-splines," *Computer Methods in Applied Mechanics and Engineering*, vol. 199, no. 5, pp. 229–263, 2010.

[110] M. A. Scott, M. J. Borden, C. V. Verhoosel, T. W. Sederberg, and T. J. Hughes, "Isogeometric finite element data structures based on bézier extraction of t-splines," *International Journal for Numerical Methods in Engineering*, vol. 88, no. 2, pp. 126–156, 2011.

[111] A.-V. Vuong, C. Giannelli, B. Jüttler, and B. Simeon, "A hierarchical approach to adaptive local refinement in isogeometric analysis," *Computer Methods in Applied Mechanics and Engineering*, vol. 200, no. 49, pp. 3554–3567, 2011.

[112] K. A. Johannessen, T. Kvamsdal, and T. Dokken, "Isogeometric anal-

ysis using lr b-splines," *Computer Methods in Applied Mechanics and Engineering*, vol. 269, pp. 471–514, 2014.

[113] N. Collier, D. Pardo, L. Dalcin, M. Paszynski, and V. M. Calo, "The cost of continuity: a study of the performance of isogeometric finite elements using direct solvers," *Computer Methods in Applied Mechanics and Engineering*, vol. 213, pp. 353–361, 2012.

[114] T. Dimont and A. Rughani, "National trends in carotid artery revascularization surgery," *Journal of Neurosurgery*, vol. 6, pp. 1251–1257, 2012.

[115] K. Schmitz, D. Behrend, P. Behrens, and W. Schmidt, "Comparative studies of different stent designs," *Journal of Biomechanical Engineering-Transactions of the ASME*, vol. 4, pp. 52–58, 1999.

[116] J. Ormiston, S. Dixon, M. Webster, P. Ruygrok, J. Stewart, I. Minchington, and T. West, "Stent longitudinal flexibility: a comparison of 13 stent designs before and after balloon expansion," *Catheterization and cardiovascular interventions*, vol. 50, pp. 120–124, 2000.

[117] K. Mori and T. Saito, "Effects of stent structure on stent flexibility measurements," *Annals of Biomedical Engineering*, vol. 6, pp. 733–742, 2005.

[118] D. Carnelli, G. Pennati, T. Villa, L. Baglioni, B. Reimers, and F. Migliavacca, "Mechanical properties of open-cell, self-expandable shape memory alloy carotid stents," *Artificial Organs*, vol. 35, pp. 74–80, 2011.

[119] L. Petrini, F. Migliavacca, F. Auricchio, and G. Dubini, "Numerical

investigation of the intravascular coronary stent flexibility," *Journal of Biomechanics*, vol. 37, pp. 495–501, 2004.

[120] M. Conti, D. Van Loo, F. Auricchio, M. De Beule, G. De Santis, B. Verhegghe, S. Pirrelli, and A. Odero, "Impact of carotid stent cell design on vessel scaffolding: A case study comparing experimental investigation and numerical simulations," *Journal of Endovascular Therapy*, vol. 18, pp. 397–406, 2011.

[121] F. Auricchio, M. Conti, M. Ferraro, and A. Reali, "Evaluation of carotid stent scaffolding through patient-specific finite element analysis," *International journal for numerical methods in biomedical engineering*, vol. 28, no. 10, pp. 1043–1055, 2012.

[122] T. Hughes, J. Evans, and A. Reali, "Finite element and nurbs approximations of eigenvalue, boundary-value, and initial-value problems.," *Computer Methods in Applied Mechanics and Engineering*, vol. 272, pp. 290–320, 2014.

[123] Y. Zhang, Y. Bazilevs, S. Goswami, C. Bajaj, and T. Hughes, "Patient-specific vascular nurbs modeling for isogeometric analysis of blood flow," *Computer methods in applied mechanics and engineering*, vol. 196, pp. 2943–2959, 2007.

[124] S. Morganti, F. Auricchio, D. Benson, F. Gambarin, S. Hartmann, T. Hughes, and A. Reali, "Patient-specific isogeometric structural analysis of aortic valve closure," *ICES REPORT*, vol. 14-10, 2014.

[125] R. Taylor, *FEAP - A finite element analysis program*, 2013.

[126] L. Petrini, F. Migliavacca, P. Massarotti, S. Schievano, G. Dubini, and F. Auricchio, "Computational studies of shape memory alloy behavior

in biomedical applications," *Journal of Biomechanical Engineering*, vol. 127, pp. 716–725, 2005.

[127] M. Spink, "Nurbs toolbox ¡ http://www.aria.uklinux.net/nurbs.php3¿, ¡ http://octave.sourceforge.net/nurbs/index.html¿," 2009.

[128] C. De Falco, A. Reali, and R. Vázquez, "Geopdes: A research tool for isogeometric analysis of pdes," *Advances in Engineering Software*, vol. 42, pp. 1020–1034, 2010.

[129] G. Holzapfel, *Nonlinear Solid Mechanics. A Continuum Approach for Engineering.* Chichester: John Wiley & Sons, 2000.

[130] F. Auricchio, M. Di Loreto, and E. Sacco, "Finite element analysis of a stenotic artery revascularization through stent insertion," *Computer Methods in Biomechanics and Biomedical Engineering*, vol. 4, pp. 249–263, 2001.

[131] F. Auricchio, M. Conti, S. Morganti, and A. Reali, "Shape-memory alloys: from constitutive modeling to finite element analysis of stent deployment," *Computer Modeling in Engineering and Sciences*, vol. 57, pp. 225–243, 2010.

[132] D. Schillinger, J. A. Evans, A. Reali, M. A. Scott, and T. J. Hughes, "Isogeometric collocation: cost comparison with galerkin methods and extension to adaptive hierarchical nurbs discretizations," *Computer Methods in Applied Mechanics and Engineering*, vol. 267, pp. 170–232, 2013.

[133] B. K. Lal, R. W. Hobson II, J. Goldstein, M. Geohagan, E. Chakhtoura, P. J. Pappas, Z. Jamil, P. B. Haser, S. Varma, F. T. Padberg,

et al., "In-stent recurrent stenosis after carotid artery stenting: life table analysis and clinical relevance," *Journal of vascular surgery*, vol. 38, no. 6, pp. 1162–1168, 2003.

[134] P. B. Snowhill, J. L. Nosher, R. L. Siegel, and F. H. Silver, "Characterization of radial forces in z stents," *Investigative radiology*, vol. 36, no. 9, pp. 521–530, 2001.

[135] S. C. Schrader and R. Beyar, "Evaluation of the compressive mechanical properties of endoluminal metal stents," *Catheterization and cardiovascular diagnosis*, vol. 44, no. 2, pp. 179–187, 1998.

[136] T. Duerig and M. Wholey, "A comparison of balloon- and self-expanding stents," *Minimally Invasive Therapy and Allied Technologies*, vol. 11, pp. 173–178, 2002.

[137] J. W. Freeman, P. B. Snowhill, and J. L. Nosher, "A link between stent radial forces and vascular wall remodeling: the discovery of an optimal stent radial force for minimal vessel restenosis," 2010.

[138] A. C. Morton, D. Crossman, and J. Gunn, "The influence of physical stent parameters upon restenosis," *Pathologie Biologie*, vol. 52, pp. 196–205, 2004.

[139] F. Migliavacca, L. Petrini, M. Colombo, F. Auricchio, and R. Pietrabissa, "Mechanical behavior of coronary stents investigated through the finite element method," *Journal of Biomechanics*, vol. 35, pp. 803–811, 2002.

[140] F. Etave, G. Finet, M. Boivin, J.-C. Boyer, G. Rioufol, and G. Thollet, "Mechanical properties of coronary stents determined by using

finite element analysis," *Journal of Biomechanics*, vol. 34, no. 8, pp. 1065–1075, 2001.

[141] C. Dumoulin and B. Cochelin, "Mechanical behaviour modelling of balloon-expandable stents," *Journal of Biomechanics*, vol. 33, no. 11, pp. 1461–1470, 2000.

[142] F. Auricchio, M. Conti, M. De Beule, G. De Santis, and B. Verhegghe, "Carotid artery stenting simulation: from patient-specific images to finite element analysis," *Medical engineering & physics*, vol. 33, no. 3, pp. 281–289, 2011.

[143] P. Wriggers and T. A. Laursen, *Computational contact mechanics*, vol. 30167. Springer, 2006.

[144] L. De Lorenzis, P. Wriggers, and T. J. Hughes, "Isogeometric contact: a review," *GAMM-Mitteilungen*, vol. 37, no. 1, pp. 85–123, 2014.

[145] M. Matzen, T. Cichosz, and M. Bischoff, "A point to segment contact formulation for isogeometric, nurbs based finite elements," *Computer Methods in Applied Mechanics and Engineering*, vol. 255, pp. 27–39, 2013.

[146] R. Dimitri, L. De Lorenzis, M. Scott, P. Wriggers, R. Taylor, and G. Zavarise, "Isogeometric large deformation frictionless contact using t-splines," *Computer methods in applied mechanics and engineering*, vol. 269, pp. 394–414, 2014.

[147] R. Schmidt, R. Wüchner, and K.-U. Bletzinger, "Isogeometric analysis of trimmed nurbs geometries," *Computer Methods in Applied Mechanics and Engineering*, vol. 241, pp. 93–111, 2012.

[148] H.-J. Kim, Y.-D. Seo, and S.-K. Youn, "Isogeometric analysis for trimmed cad surfaces," *Computer Methods in Applied Mechanics and Engineering*, vol. 198, no. 37, pp. 2982–2995, 2009.

[149] A. U. Manual, "Version 6.11," *Dassault Systems Simulia Corp., USA*, 2008.

[150] F. Auricchio, M. Conti, M. De Beule, G. De Santis, and B. Verhegghe, "Carotid artery stenting simulation: from patient-specific images to finite element analysis," *Medical engineering & physics*, vol. 33, no. 3, pp. 281–289, 2011.

[151] F. Auricchio, M. Conti, S. Marconi, A. Reali, J. L. Tolenaar, and S. Trimarchi, "Patient-specific aortic endografting simulation: From diagnosis to prediction," *Computers in biology and medicine*, vol. 43, no. 4, pp. 386–394, 2013.

[152] C. De Falco, A. Reali, and R. Vázquez, "Geopdes: a research tool for isogeometric analysis of pdes," *Advances in Engineering Software*, vol. 42, no. 12, pp. 1020–1034, 2011.